Ariel School
solar system & exoplanets

Pierre Drossart

29 September 2019

l'Observatoire de Paris | LESIA

Laboratoire d'Études Spatiales et d'Instrumentation en Astrophysique

General Summary

General Introduction : planets and exoplanets

Uranus, by Voyager 2 in 1986

1. Bond albedo and radiative equilibrium

Intermezzo : the true color of the planets

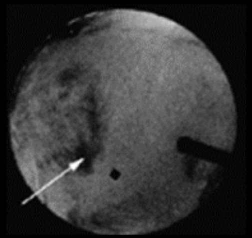

Mars polarization (HST, 2003)

2. Polarization effects in planetary atmospheres

Intermezzo : Rayleigh scattering and colors

Mars H scattering (UVS/MAVEN 2016)

3. Atmospheric escape

Intermezzo : habitability

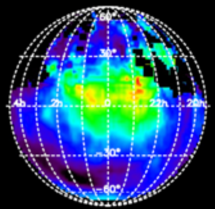

Venus, O_2 emission (VIRTIS/VEX, 2012)

4. Non-LTE effects in planetary atmospheres

Historical perspectives:

- First observations : historical images
- Imaging ~ XXth century, polarimetry ~1930
- Infrared => early observations of planets : circa 1939
- Space age : 1969 and ff

Base de Données d'Images Planétaires

http://www.lesia.obspm.fr/BDIP/

¤ Homepage

¤ What is BDIP ?
¤ User manual
¤ Observatories

¤ Saturn
¤ Jupiter
¤ Mars
¤ Venus
¤ Mercury

¤ Credits
¤ Contact

Database Jupiter

Result of request : 5 records found

Current page : 1/1

Select all / Reset all / Print selection in a file / Download selected images in a zipped file

	Image	Index	Date	Time	LCM1 [°]	LCM2 [°]	λ [°]	Filter	Observatory
☐	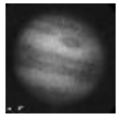	1321	1961-08-26	22:07:00	0.00	355.00	0.00	G	PM
☐	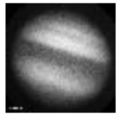	1332	1962-08-22	22:29:00	162.00	213.00	337.00	G	PM
☐	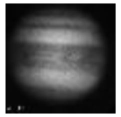	1338	1962-08-23	01:22:00	272.00	323.00	336.50	G	PM
☐	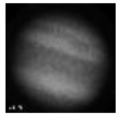	1351	1962-08-25	23:53:00	332.00	0.00	337.00	G	PM
☐	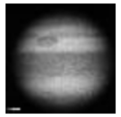	1375	1962-09-11	23:46:00	133.00	33.00	338.00	G	PM

¤ Back to search form

Design by SIGAL

Historical perspectives:

- First observations : historical images
- Infrared => early observations Jupiter et al : circa 1939
- Mars : images and polarization : circa 1930
- Space age : 1969 and following

Spectrocopy planets & exoplanets

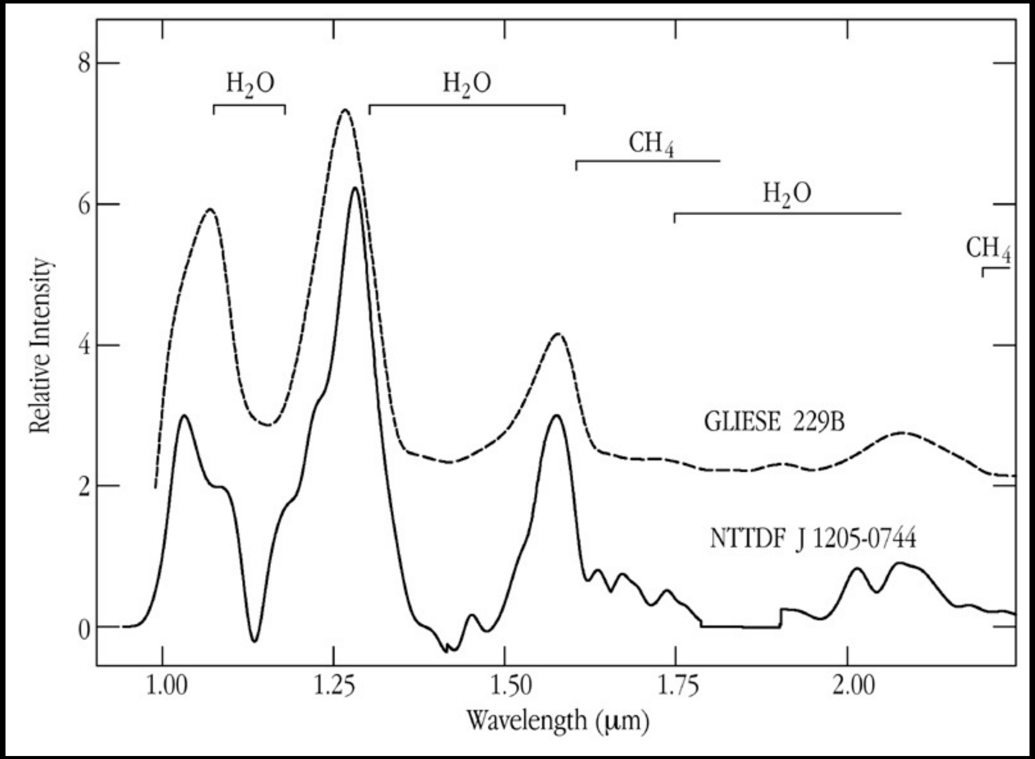

G. Kuiper, ApJ, 1947

Infrared Spectroscopy of planets –started as soon as 1930 years – details similar to today's exoplanet spectroscopy

Historical perspectives:

- First observations : historical images
- Infrared => early observations Jupiter et al : circa 1939
- Mars : spectroscopy and polarization
- Space age : 1969 and ff

Lyot observations of the polarization of planets in the 1920ies

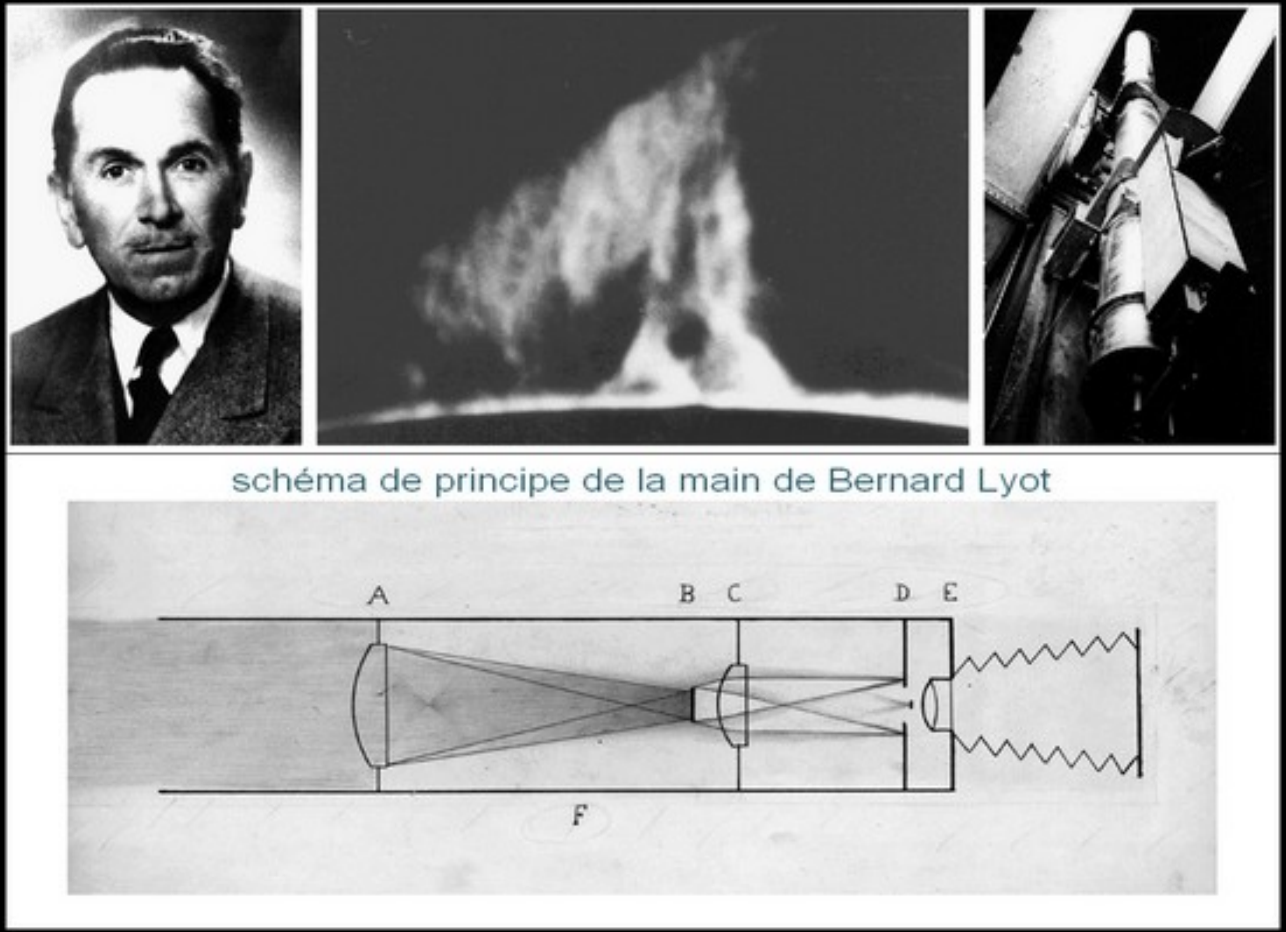

Historical perspectives:

- First observations : historical images
- Infrared => early observations Jupiter et al : circa 1939
- Mars : spectroscopy and polarization
- Space age : 1969 and ff

Mars exploration by Soviet and US spacecraft

Selected Soviet Mars probes

Spacecraft	Orbiter or flyby outcome	Lander outcome
Mars 1	Failure	Failure
Mars 2	Success	Failure
Mars 3	Partial success	Partial success
Mars 4	Failure	N/A
Mars 5	Partial success	N/A
Mars 6	Success	Failure
Mars 7	Success	Failure
Phobos 1	Failure	Not deployed
Phobos 2	Partial success	Not deployed

NASA / US earlyprobes

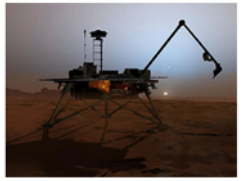
Mars Phoenix


Mars Exploration Rover - Opportunity


Mars Exploration Rover - Spirit

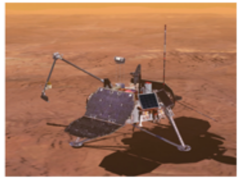
Mars Polar Lander/Deep Space 2

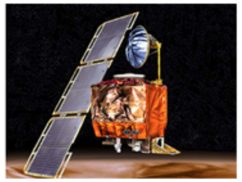
Mars Climate Orbiter


Mars Global Surveyor

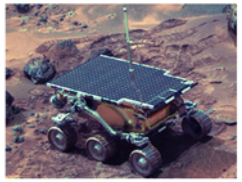
Mars Pathfinder


Mars Observer

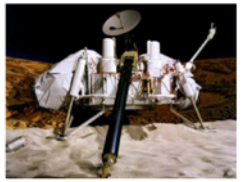
Viking 1 & 2

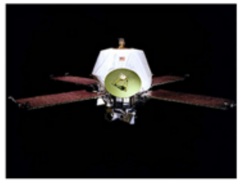
Mariner 8 & 9


Mariner 6 & 7

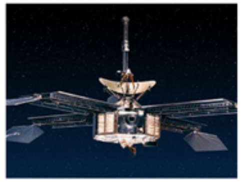
Mariner 3 & 4

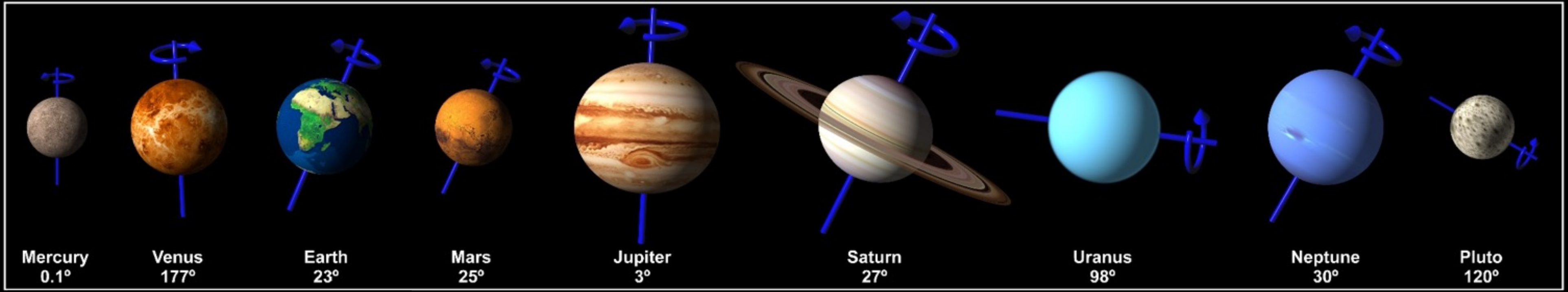

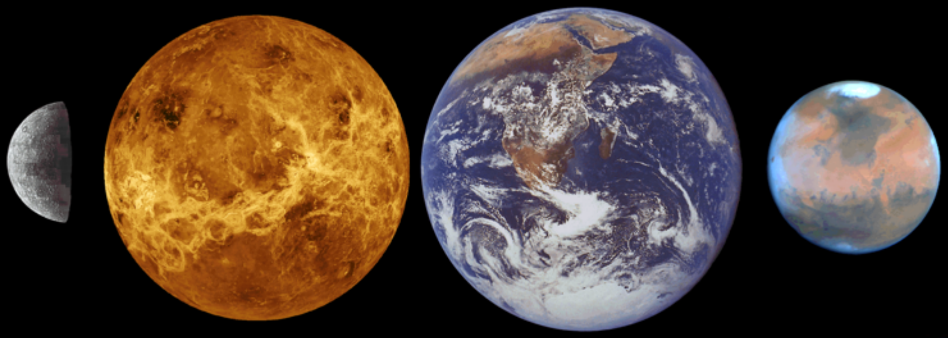

Solar system largest bodies

Basic facts about planets

Size, mass, orbits, etc.

	Name	Equatorial diameter [h]	Mass [h]	Semi-major axis (AU)	Orbital period (years) [h]	Inclination to Sun's equator (°)	Orbital eccentricity	Rotation period (days)	Confirmed moons [i]	Axial tilt (°)	Rings	Atmosphere
1.	Mercury	0.382	0.06	0.39	0.24	3.38	0.206	58.64	0	0.04	no	minimal
2.	Venus	0.949	0.82	0.72	0.62	3.86	0.007	−243.02	0	177.36	no	CO_2, N_2
3.	Earth [a]	1.00	1.00	1.00	1.00	7.25	0.017	1.00	1	23.44	no	N_2, O_2, Ar
4.	Mars	0.532	0.11	1.52	1.88	5.65	0.093	1.03	2	25.19	no	CO_2, N_2, Ar
5.	Jupiter	11.209	317.8	5.20	11.86	6.09	0.048	0.41	79	3.13	yes	H_2, He
6.	Saturn	9.449	95.2	9.54	29.46	5.51	0.054	0.43	62	26.73	yes	H_2, He
7.	Uranus	4.007	14.6	19.22	84.01	6.48	0.047	−0.72	27	97.77	yes	H_2, He, CH_4
8.	Neptune	3.883	17.2	30.06	164.8	6.43	0.009	0.67	14	28.32	yes	H_2, He, CH_4

Planet	Radius (km)	Radius (Earth = 1)	Mass (kg)	Mass (Earth = 1)	Escape velocity (km/sec)
Mercury	2439	0.382	3.3×10^{23}	0.0558	4.3
Venus	6052	0.95	4.9×10^{24}	0.815	10.3
Earth	6378	1.00	6.0×10^{24}	1.00	11.2
Mars	3398	0.53	6.4×10^{23}	0.1075	5.0
Jupiter	71,494	11.20	1.9×10^{27}	317.83	61
Saturn	60,330	9.42	5.7×10^{26}	95.147	35.6
Uranus	25,559	4.01	8.7×10^{25}	14.54	22
Neptune	24,750	3.93	1.0×10^{26}	17.23	25

Planet	Average density (kg/m^3)	Composition (In order of abundance)	Surface gravity (Earth = 1)	Escape velocity (km/sec)	Rotation Period	Tilt
Mercury	5440	Fe, Ni, Si	0.378	4.3	58.646d	0°
Venus	5240	Si, Fe, Ni	0.903	10.3	244.3d	177°
Earth	5497	Si, Fe, Ni	1.00	11.2	23h56m	23° 27"
Mars	3940	Si, Fe, S	0.379	5.0	24h37m	23° 59"
Jupiter	1340	H, He	2.54	61	9h50.5m	3° 5"
Saturn	690	H, He	1.16	35.6	10h14m	26° 24"
Uranus	1190	H, C, N, O	0.919	22	17h14m	97° 55"
Neptune	1660	H, C, N, O	1.19	25	16h3m	28° 48"

Mars historical observations

base de données d'images planétaires (bdip, LESIA)

Image	Index	Date	Time	LCM [°]	λ [°]	Filter	Observatory
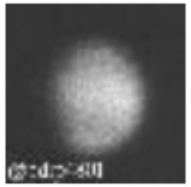	4801	1962-11-12	14:55:00	7.96	97.00	B	TM
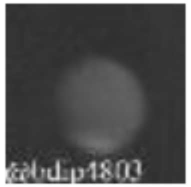	4803	1962-11-22	13:50:00	257.39	101.76	B	TM
	4806	1962-12-14	13:00:00	39.43	112.04	B	TM
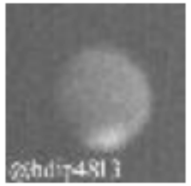	4813	1962-12-22	11:40:00	306.33	115.69	B	TM
	4814	1962-12-27	11:28:00	257.80	117.97	B	TM
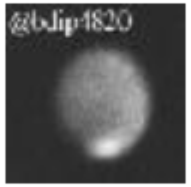	4820	1962-12-28	11:49:00	253.84	118.44	B	TM

Observations of Venus

Observations of Venus at Pic du Midi

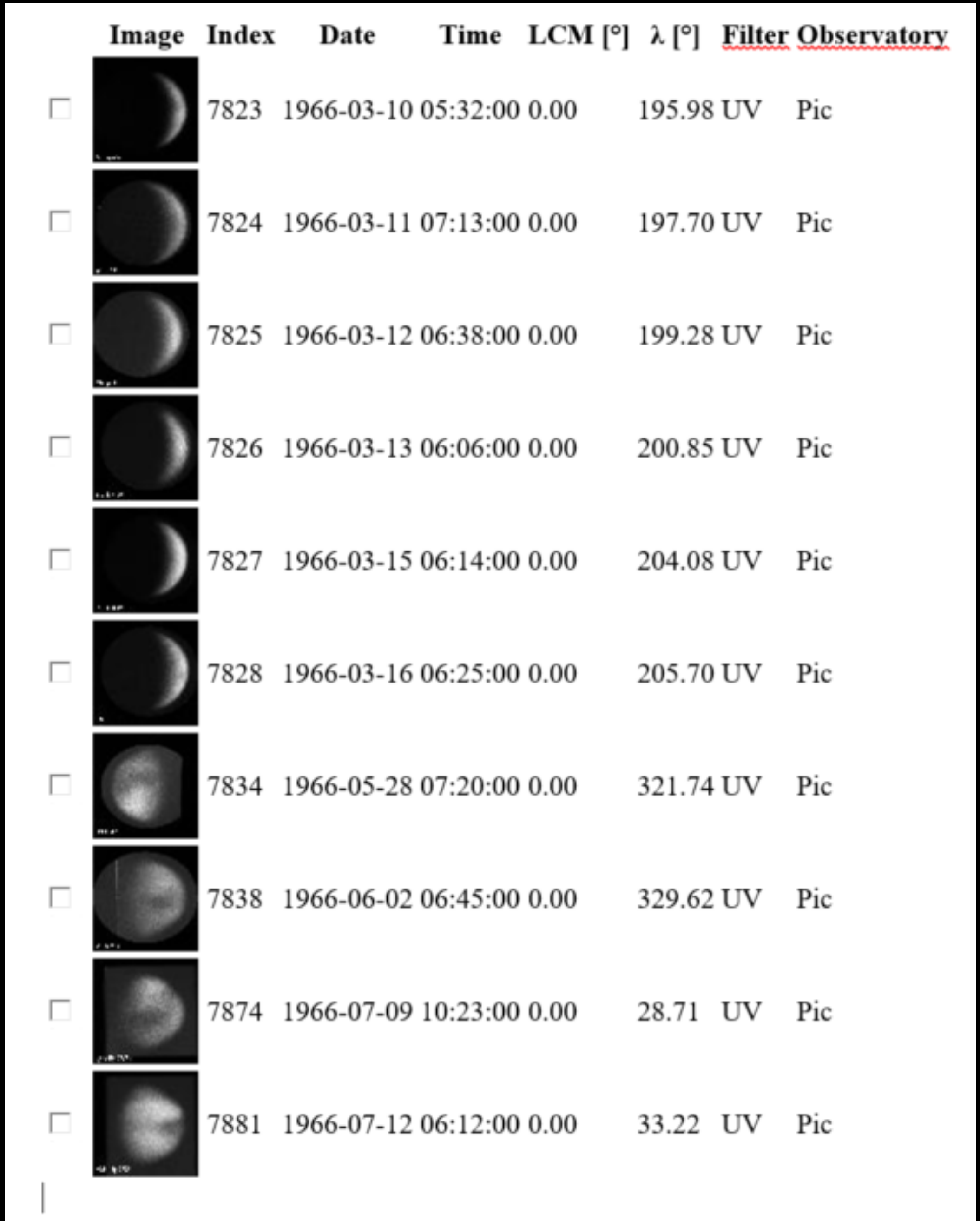

Image	Index	Date	Time	LCM [°]	λ [°]	Filter	Observatory
	7823	1966-03-10	05:32:00	0.00	195.98	UV	Pic
	7824	1966-03-11	07:13:00	0.00	197.70	UV	Pic
	7825	1966-03-12	06:38:00	0.00	199.28	UV	Pic
	7826	1966-03-13	06:06:00	0.00	200.85	UV	Pic
	7827	1966-03-15	06:14:00	0.00	204.08	UV	Pic
	7828	1966-03-16	06:25:00	0.00	205.70	UV	Pic
	7834	1966-05-28	07:20:00	0.00	321.74	UV	Pic
	7838	1966-06-02	06:45:00	0.00	329.62	UV	Pic
	7874	1966-07-09	10:23:00	0.00	28.71	UV	Pic
	7881	1966-07-12	06:12:00	0.00	33.22	UV	Pic

Image	Index	Date	Time	LCM1 [°]	LCM2 [°]	λ [°]	Filter	Observatory
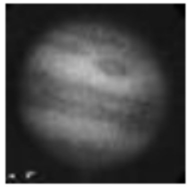	1321	1961-08-26	22:07:00	0.00	355.00	0.00	G	PM
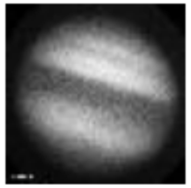	1332	1962-08-22	22:29:00	162.00	213.00	337.00	G	PM
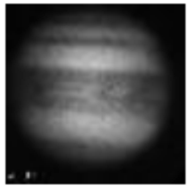	1338	1962-08-23	01:22:00	272.00	323.00	336.50	G	PM
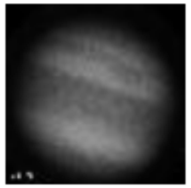	1351	1962-08-25	23:53:00	332.00	0.00	337.00	G	PM
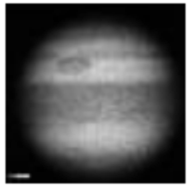	1375	1962-09-11	23:46:00	133.00	33.00	338.00	G	PM

Infrared observations of Jupiter at 5 micron

Strong nhomogeneities in

planetary pemissions

and the quest for H_2O on Jupiter…

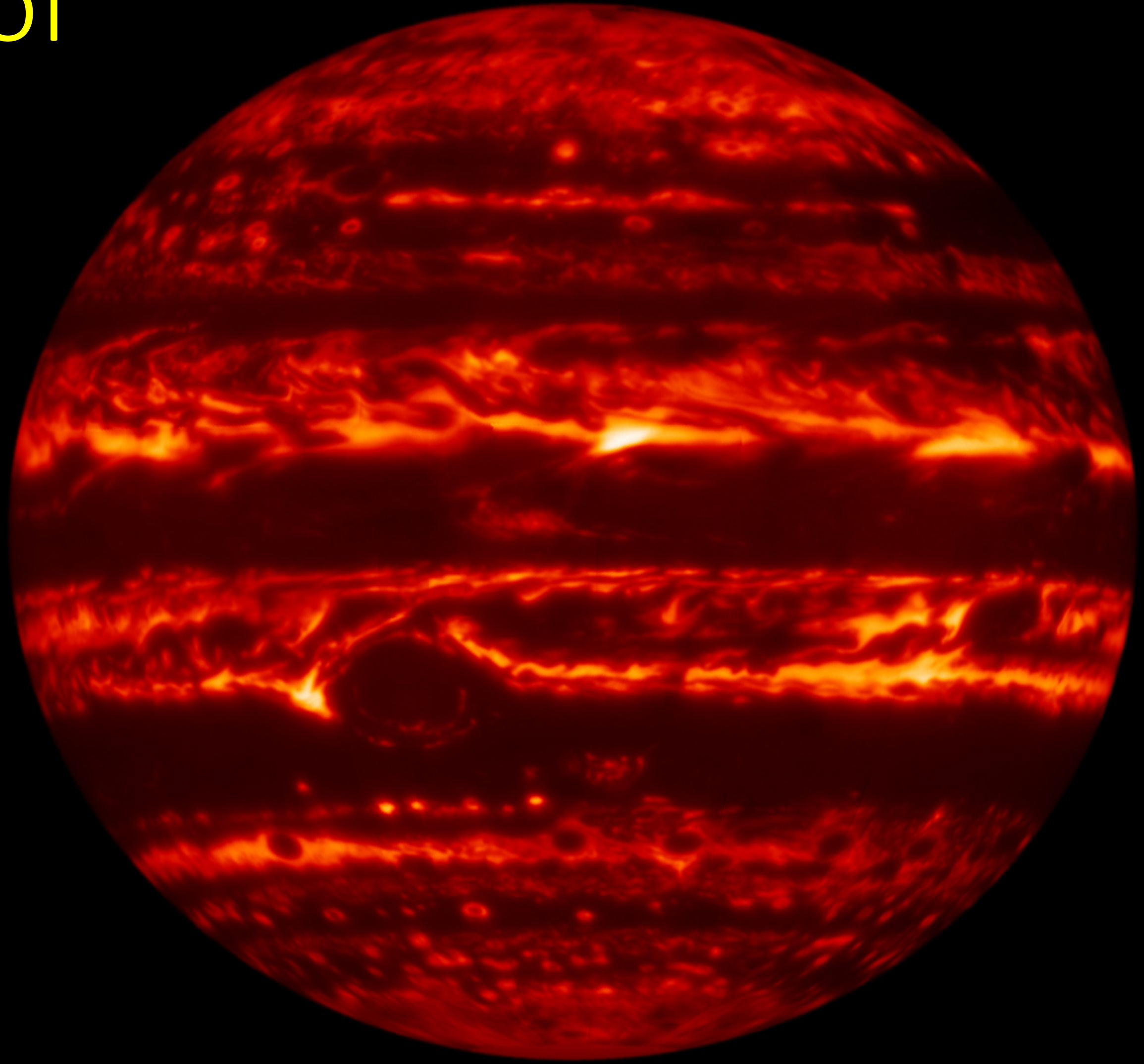

Credit: Gemini Observatory/AURA/NSF/UC Berkeley

The Earth seen as a planet

Earth & Moon on Dec. 16, 1992
(Galileo/SSI)

Galileo arrived at Jupiter on December 7, 1995, after gravitational assist flybys of Venus and Earth, and became the first spacecraft to orbit Jupiter. It launched the first probe into Jupiter, directly measuring its atmosphere.

Earth and Venus : the twin planets

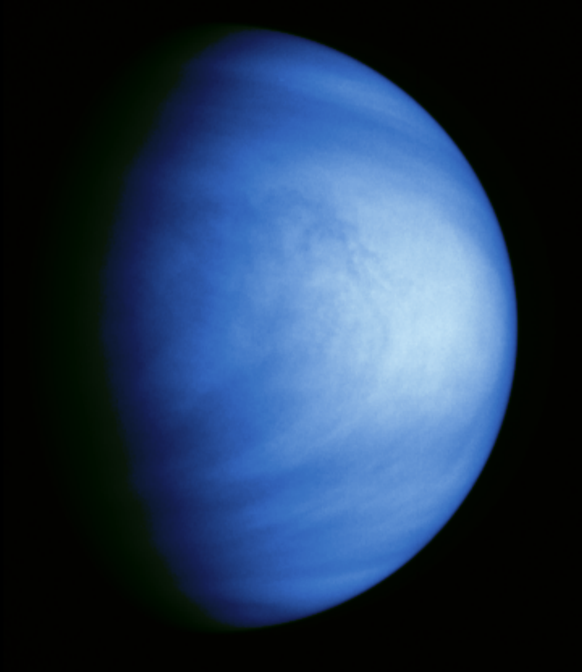

Vénus		Terre
0,72 UA	D	1 UA
0,95	R	1
0,82	M	1
-2,6°	I	23,5°
225 jours	Y	365 jours
243 jours rétrograde	D	1 jour = 23h56mn
460°C	T	15°C
92	P	1

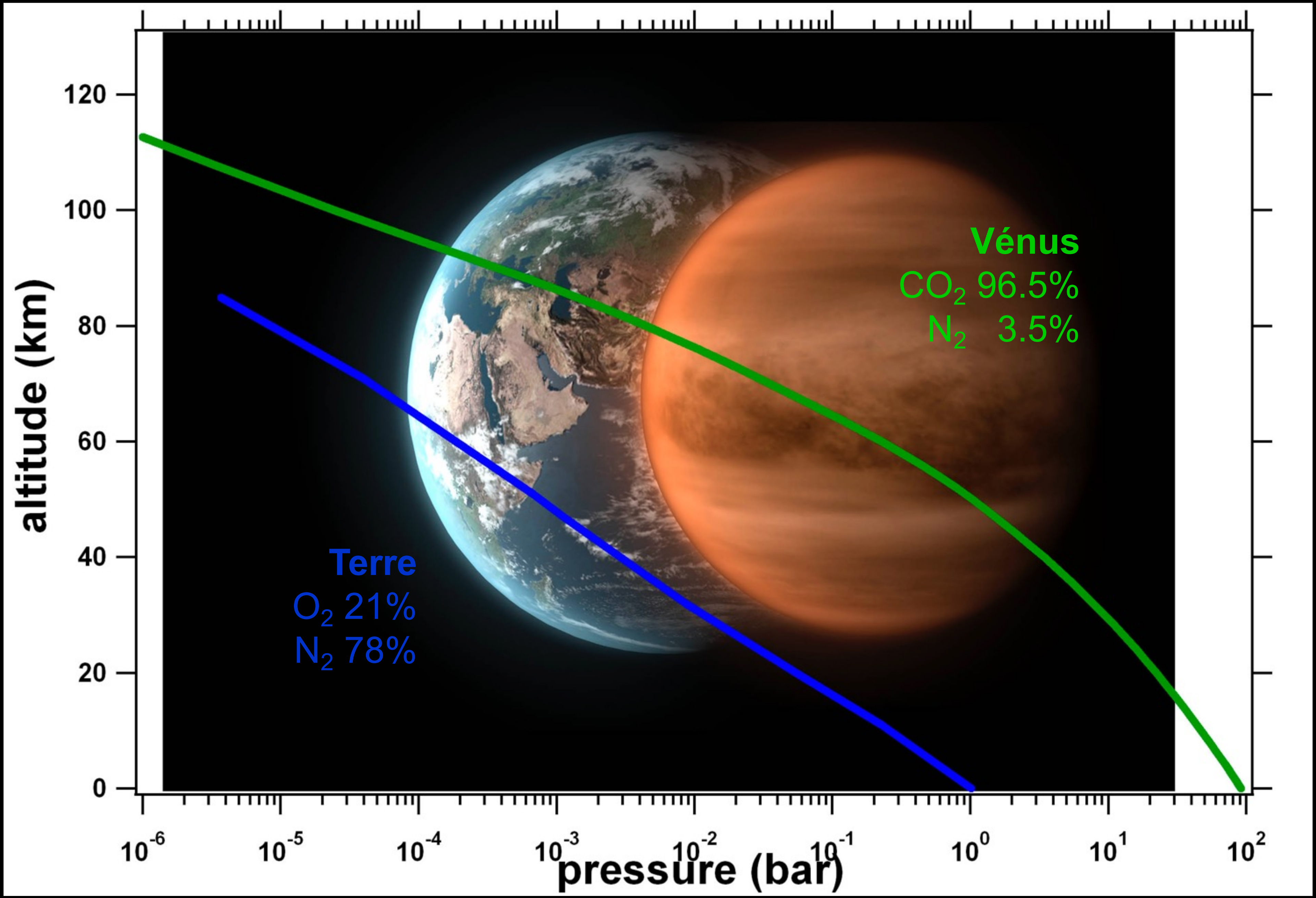
altitude (km)
120
100
80
60
40
20
0
10^-6
10^-5
10^-4
10^-3
10^-2
10^-1
10^0
10^1
10^2
pressure (bar)
Vénus
CO2 96.5%
N2 3.5%
Terre
O2 21%
N2 78%

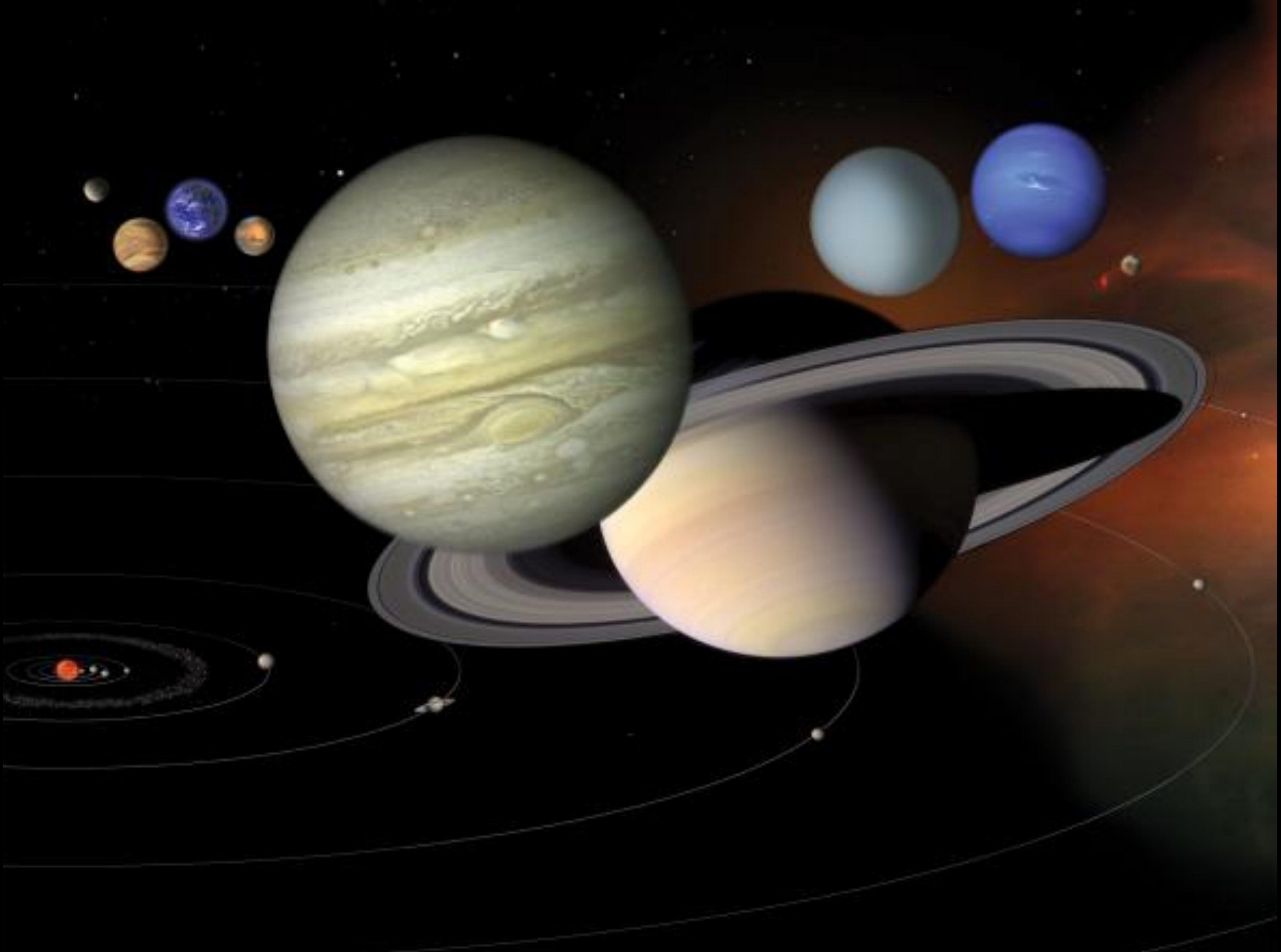

Jupiter’s atmosphere

coupling

-Thermal structure and dynamics (tropo/strato/thermosphere)

- Stratospheric composition

- Vertical coupling (from interior to ionsphere)

- Thermospheric heating

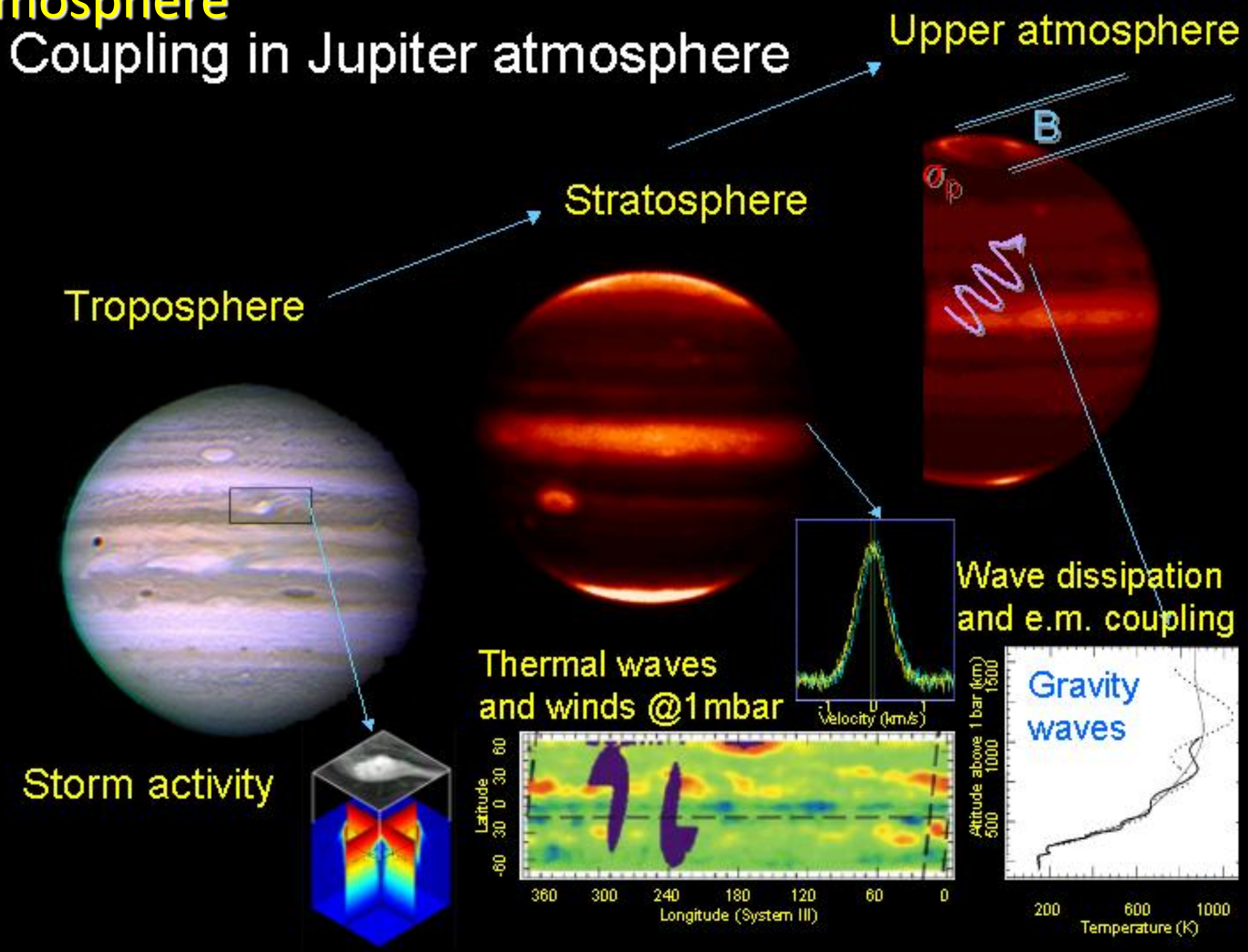

Astéroïdes et comètes

Astéroïde Lutetia (mission Rosetta)

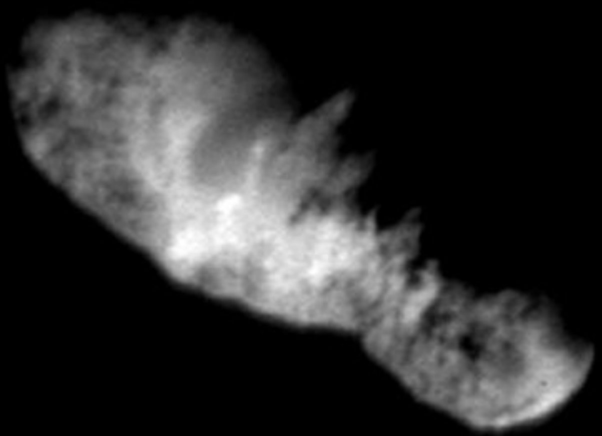

Comète Borelly (Deep Space 1)

La comète Hale-Bopp

Orbite de l’objet de
Kuiper 1998 WW31
(double)

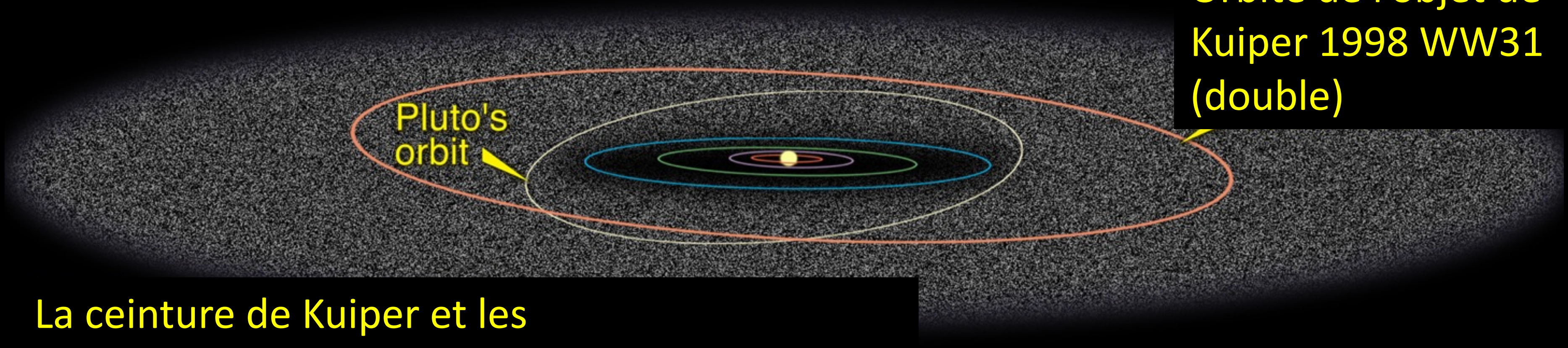

La ceinture de Kuiper et les
Orbites des planètes

Part 1. Photometry of planets

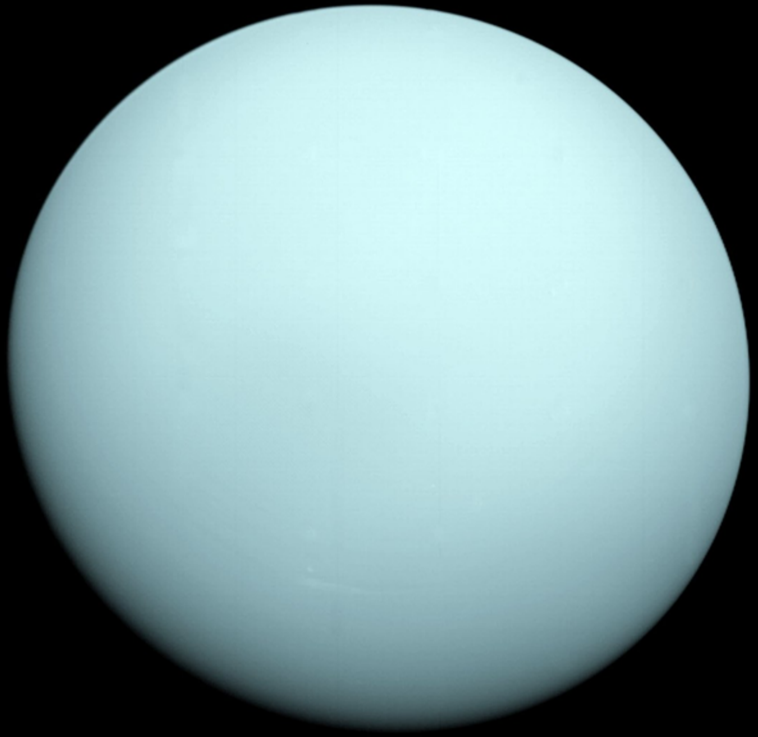

Some definitions

Lambertian surface

Definition : equally bright
In all directions

See M.K. Shepard ; Introduction to Planetary Photometry, Cambridge Univ. Press, 2017

Surface Appearance

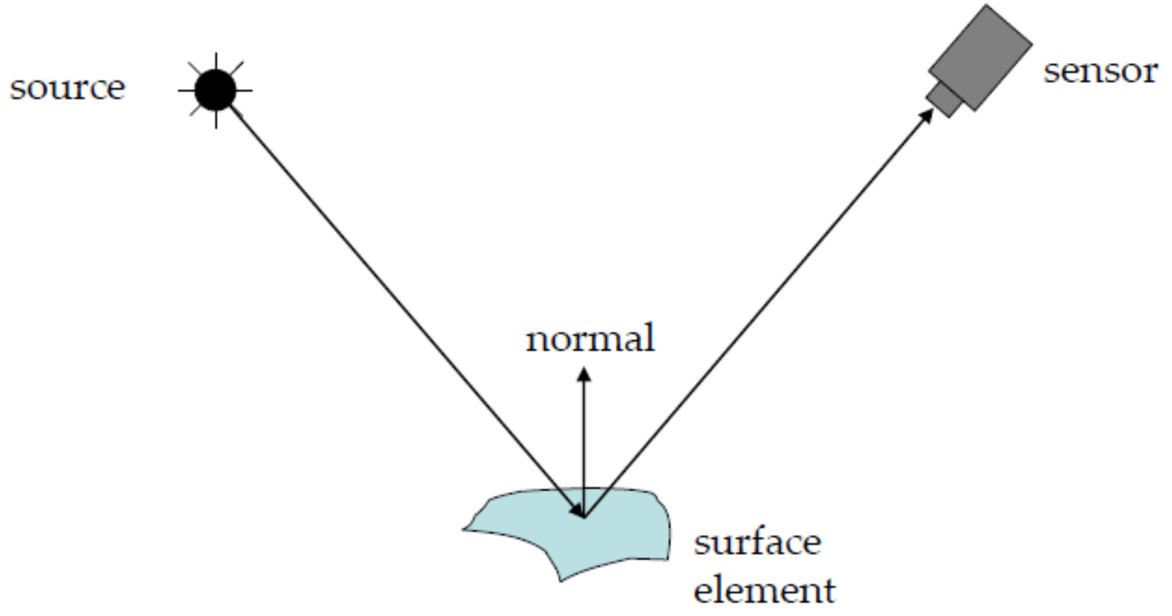

Image intensities = f (normal, surface reflectance, illumination)

Surface Reflection depends on both the viewing and illumination direction.

Disk resolved photometry

Ratio of measured radiance from a surface to the incident irradiance

$r_{brdf} = L / E$

Units = sr^{-1}

For perfect lambertian : $r=\pi^{-1}$

BRDF: Bidirectional Reflectance Distribution Function

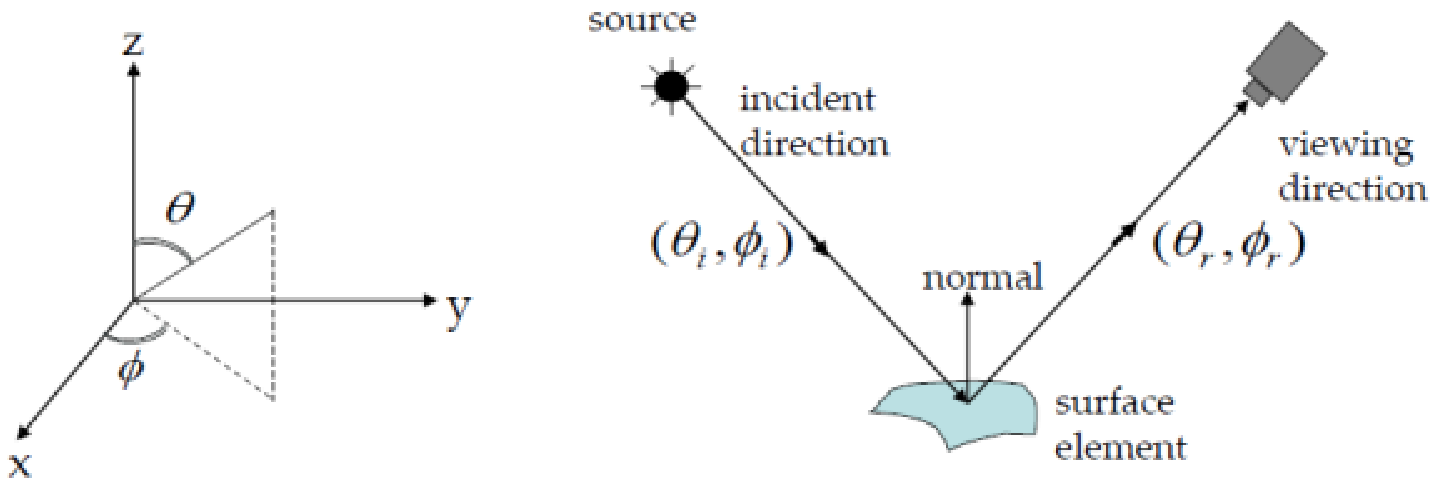

$E^{surface}(\theta_i,\phi_i)$ Irradiance at Surface in direction (θ_i,ϕ_i)

$L^{surface}(\theta_r,\phi_r)$ Radiance of Surface in direction (θ_r,ϕ_r)

$$\text{BRDF}: f(\theta_i,\phi_i;\theta_r,\phi_r) = \frac{L^{surface}(\theta_r,\phi_r)}{E^{surface}(\theta_i,\phi_i)}$$

Lambertian diffuse reflection

Diffuse Reflection and Lambertian BRDF

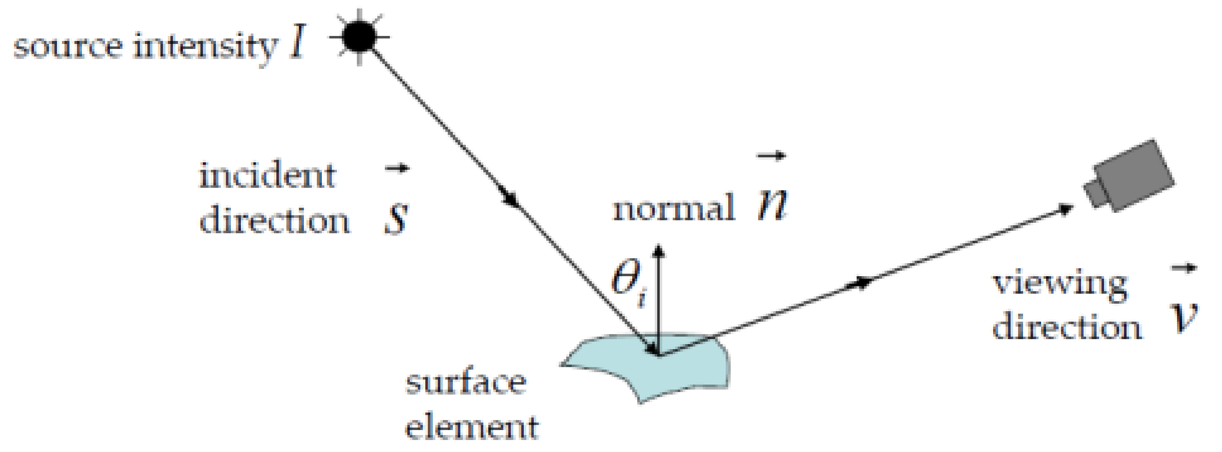

- Surface appears equally bright from ALL directions! (independent of $\vec{v}$)
- Lambertian BRDF is simply a constant : $f(\theta_i, \phi_i; \theta_r, \phi_r) = \frac{\rho_d}{\pi}$ (albedo: ρ_d)
- Surface Radiance : $L = \frac{\rho_d}{\pi} I \cos \theta_i = \frac{\rho_d}{\pi} I \; \vec{n} \cdot \vec{s}$ (I: source intensity)
- Commonly used in Vision and Graphics!

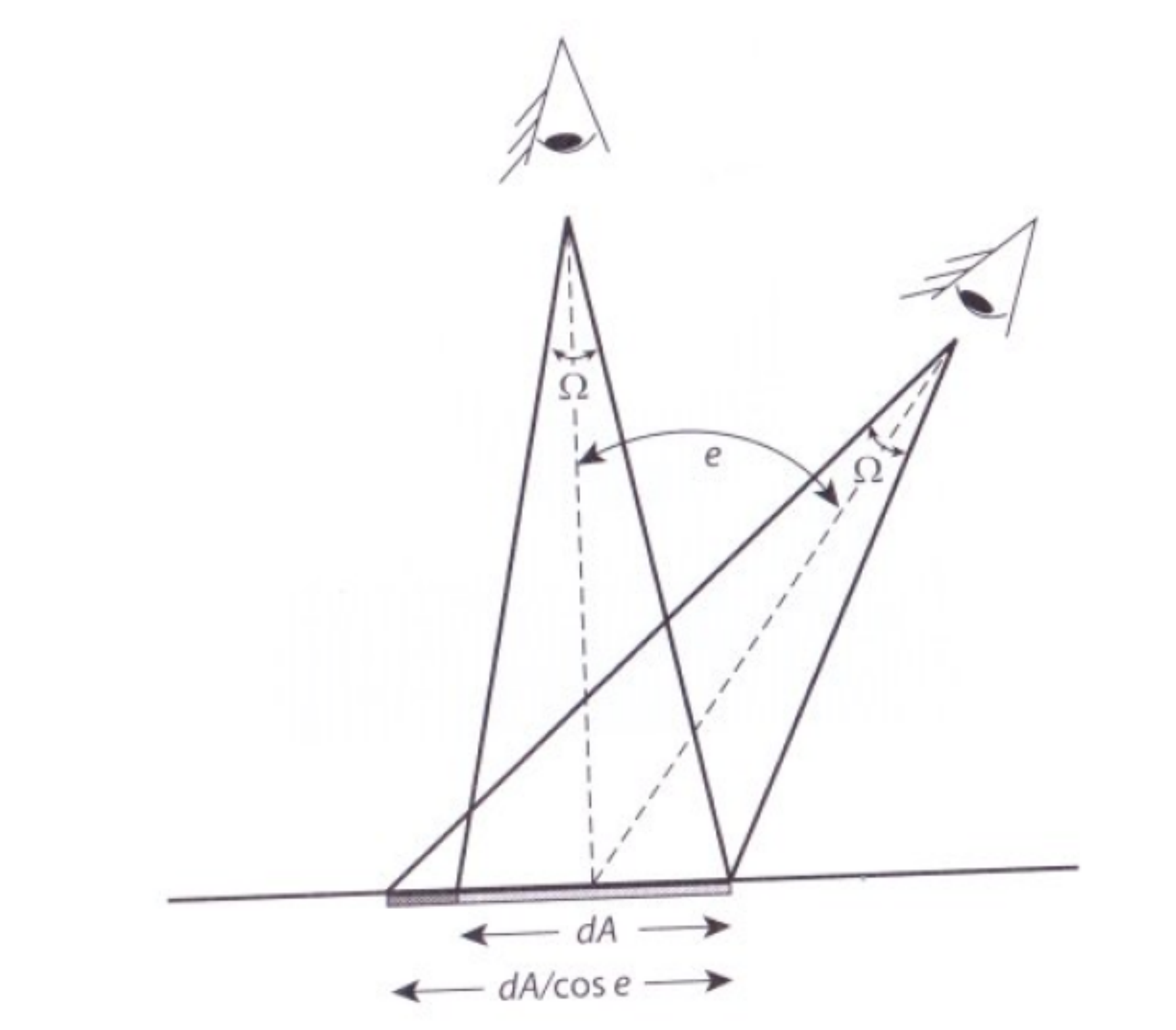
Ω
e
Ω
dA
dA/cos e

Full disk photometry

Integration over illuminated disk

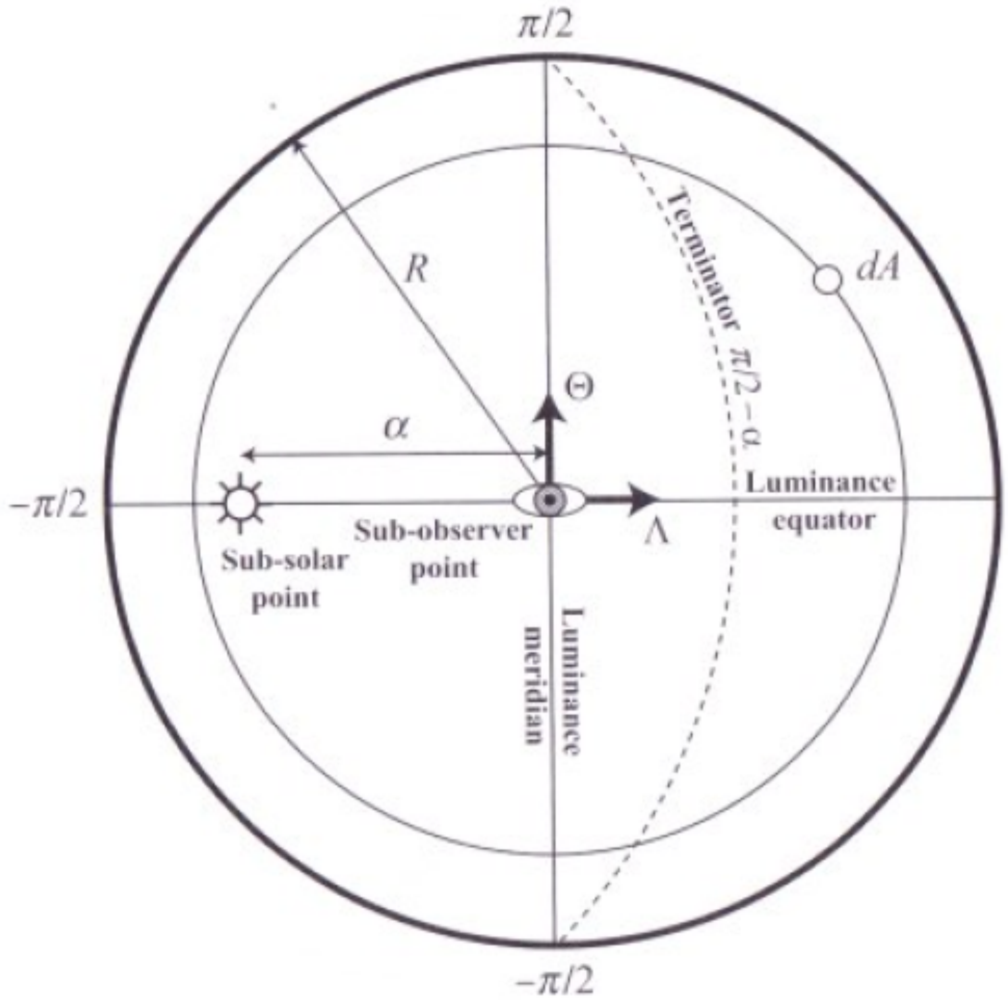

Figure 5.7. Geometry for spherical integration using luminance coordinates. Credit: Michael K. Shepard.

More definitions

- Geometric albedo p : amount of light reflected by a planetary body divided by the amount of light of a perfect lambertian disk of the same cross section area

$$p = \frac{I(0)}{I_{lam}}$$

- Phase function : directional dependence of light scattered in all directions by a planet
- Phase integral : q = 2 * integral of phase function
- Bond albedo : fraction of total incident power scattered into space

$$A = p\, q$$

Table 1 The definitions of some commonly used reflectance quantities

Quantity	Definition	Formula
Bidirectional reflectance	Ratio of the scattered radiance towards (i, e, α) to the collimated incident irradiance	$r(i,e,\alpha) = I(i,e,\alpha)/J$ [ster^{-1}]
Bidirectional reflectance distribution function (BRDF)	Ratio of the scattered radiance towards (i, e, α) to the collimated power incident on a unit area of the surface	$\text{BRDF} = I(i,e,\alpha)/J\mu_0 = r/\mu_0$ [ster^{-1}]
Radiance factor (RADF)	Ratio of the bidirectional reflectance of a surface to that of a perfectly scattering surface$^{\$}$ illuminated at normal direction	$\text{RADF} = \pi r(i,e,\alpha) = [I/F]$
Reflectance factor (or reflectance coefficient, REFF)	Ratio of the reflectance of a surface to that of a perfectly diffused surface under the same conditions of illumination and viewing	$\text{REFF} = \pi r/\mu_0 = [I/F]/\mu_0$
Lambertian albedo	Ratio of the total scattered irradiance towards all directions from a Lambert surface to incident power per unit area	$A_L = P_L/J\mu_0$ Perfectly scattering surface has $A_L = 1$
Normal albedo	Ratio of the reflectance of a surface observed at zero phase angle from an arbitrary direction to that of a perfectly diffuse surface located at the same position, but illuminated and observed perpendicularly	$A_n = \pi r(e,e,0)$
Geometric albedo (physical albedo)	Ratio of the integral brightness of a body at zero phase angle to the brightness of a perfect Lambert disk of the same size and at the same distance, but illuminated and observed perpendicularly. It is the weighted average of the normal albedo over the illuminated area of the body	$A_p = \int_{2\pi} r(e,e,0)\mu\, d\Omega\ ^{\#}$
Bond albedo (spherical albedo, or global albedo)	Total fraction of incident irradiance scattered by a body into all directions	$A_s = \frac{1}{\pi}\int_{2\pi}\int_{2\pi} r(i,e,\alpha)\mu\, d\Omega_e\, d\Omega_i$
Bolometric albedo (radiometric albedo)	Average of the spectral albedo $A_s(\lambda)$ weighted by the spectral irradiance of the Sun $J_s(\lambda)$	$A_b = \frac{\int_0^\infty A_S(\lambda)J_S(\lambda)\, d\lambda}{\int_0^\infty J_S(\lambda)\, d\lambda}$
Phase integral		$q = 2\int_0^\pi \Phi_p(\alpha)\sin\alpha\, d\alpha$

How to measure a Bond albedo ?

Geometric albedo, or albedo at some phase angle

Phase functions => access to full disk viewing geometry

⇒Limited to inner planets !

or complete the phase curve with modeling…

Image	Index	Date	Time	LCM [°]	λ [°]	Filter	Observatory
	7823	1966-03-10	05:32:00	0.00	195.98	UV	Pic
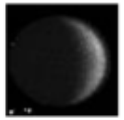	7824	1966-03-11	07:13:00	0.00	197.70	UV	Pic
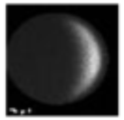	7825	1966-03-12	06:38:00	0.00	199.28	UV	Pic
	7826	1966-03-13	06:06:00	0.00	200.85	UV	Pic
	7827	1966-03-15	06:14:00	0.00	204.08	UV	Pic
	7828	1966-03-16	06:25:00	0.00	205.70	UV	Pic
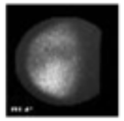	7834	1966-05-28	07:20:00	0.00	321.74	UV	Pic
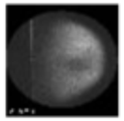	7838	1966-06-02	06:45:00	0.00	329.62	UV	Pic
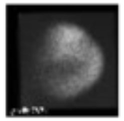	7874	1966-07-09	10:23:00	0.00	28.71	UV	Pic
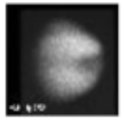	7881	1966-07-12	06:12:00	0.00	33.22	UV	Pic

Telluric planets phase curves

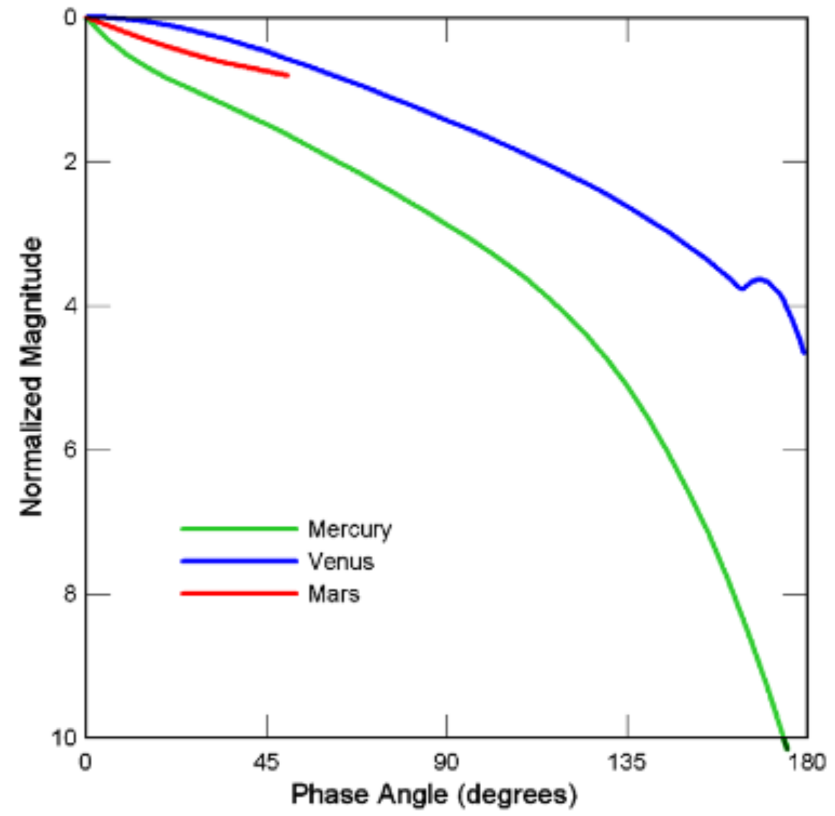

Fig. 1. The observed V-band phase curves of Mercury, Venus and Mars. Magnitudes have been normalized at phase angle zero. The photometry was obtained with the SOHO spacecraft and ground-based telescopes.

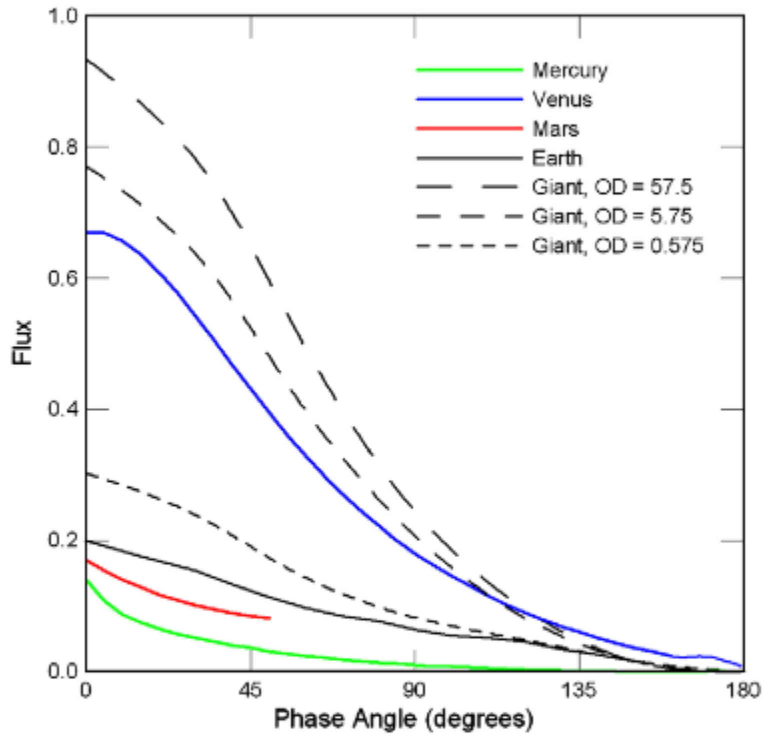

Fig. 2. The empirical phase functions of Mercury, Venus and Mars are compared with theoretical curves for giant planets and observed curve of the Earth. The giant planet data sets are distinguished according to optical density (OD). Values taken from Fig. 2 of Stam and Hovenier were divided by π so that flux at phase angle zero is one for a planet with unit geometric albedo. Furthermore 180° was subtracted from their scattering angle to give phase angle. The Earth data are adapted from the effective albedos in Fig. 1 of Goode et al. (2001) as described in Section 3 and the notes to Table 1.

Mallama, Icarus, 2009

Bond albedo of giant planets

- Giant planets => best measurements to date by Voyager

Jupiter : Hanel et al, J. Geophys. Res., 1981

Saturn : Hanel et al, Icarus, 1983

Uranus : Pearl et al, Icarus, 1990

ICARUS 84, 12–28 (1990)

The Albedo, Effective Temperature, and Energy Balance of Uranus, as Determined from Voyager IRIS Data

J. C. PEARL, B. J. CONRATH, R. A. HANEL, AND J. A. PIRRAGLIA

NASA/Goddard Space Flight Center, Greenbelt, Maryland 20771

AND

A. COUSTENIS

Observatoire de Paris, Meudon, France

Received September 27, 1988; revised July 27, 1989

Data from the Voyager infrared spectrometer and radiometer (IRIS) investigation are used to determine the albedo, effective temperature, and energy balance of Uranus. From broadband radiometric observations made over a range of phase angles $15° < \alpha < 155°$, an orbital mean value for the bolometric Bond albedo, $\bar{A} = 0.300 \pm 0.049$, is obtained, which yields an equilibrium temperature $T_{eq} = 58.2 \pm 1.0°K$. From thermal spectra obtained over latitudes from pole to pole, an effective temperature $T_{eff} = 59.1 \pm 0.3°K$ is derived. This represents a substantial improvement over previously determined values. The energy balance of Uranus is therefore $E = 1.06 \pm 0.08$; the one-standard-error upper limit of 1.14 is lower than previous results.

Method of measurement of the phase curve

IRIS instrument on Voyager – 50 cm Cassegrain telescope

- Visible radiometer (5600 – 33,000 cm^{-1}) / Calibrated on diffuse target of known photometric reflectivity
- Infrared radiometer : 180cm^{-1} to ~400 cm^{-1} for Uranus
- Phase curve measurements : 15 to 155° only due to orbital constraints => to retrieve the Bond albedo, an extrapolation is needed

By Minneart function $I = I_0 \, \mu_0^k \, \mu^{k-1}$ k~0.8

Phase curve for Uranus (Pearl et al)

Geometric albedo p

p=0.231 +/- 0.046

Phase curve integral : q

q = 1.40 +/- 0.14

$\Rightarrow$Estimate of Bond albedo A_b

$$\overline{A}_{\text{Uranus}} = 0.300 \pm 0.049.$$

Thermal emission estimated from infrared spectra passing from resolved to disk integrated emission : effective temperature estimated 59.0K

$\Rightarrow$Energy balance :

E = 1.06 +/- 0.08

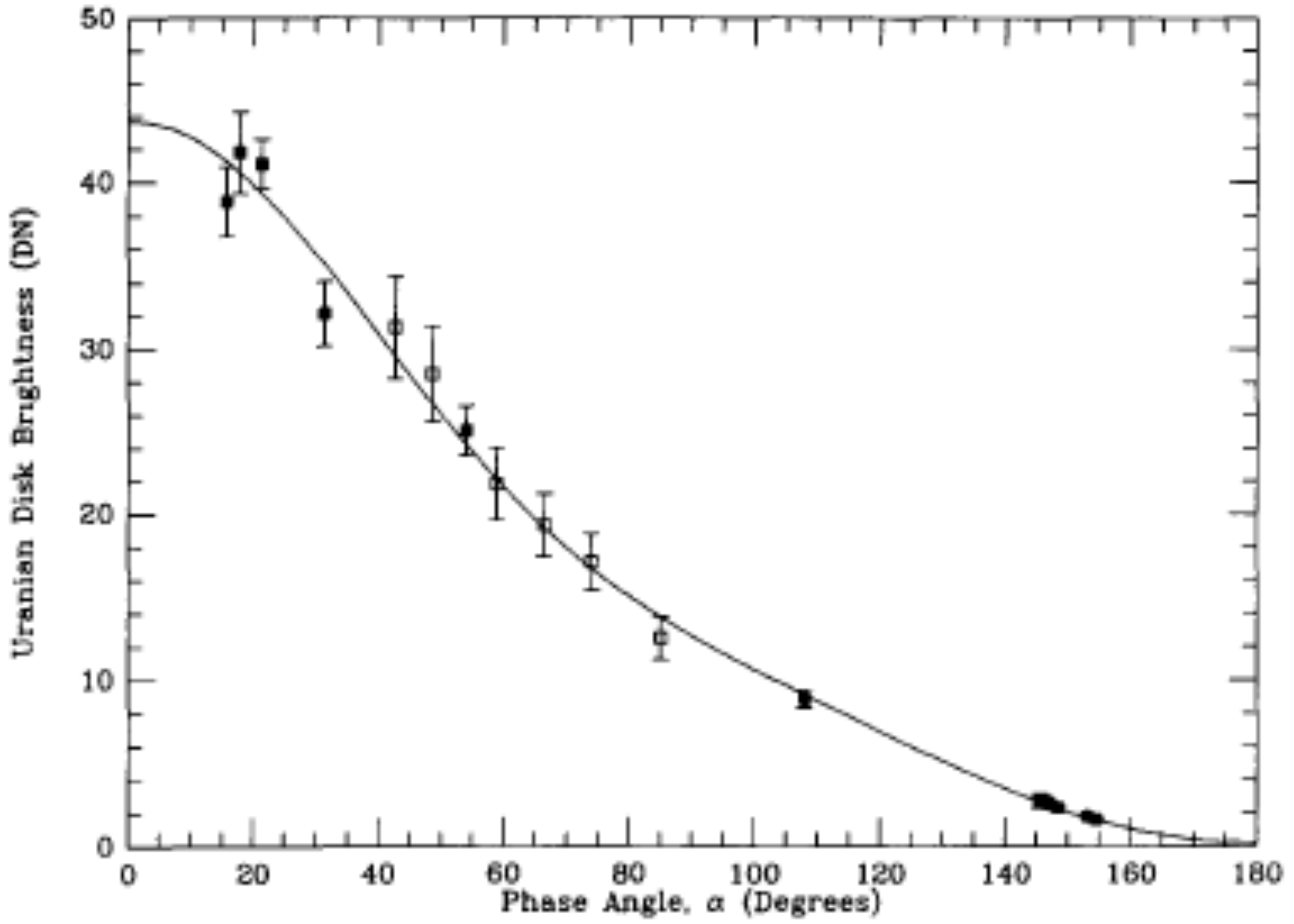

FIG. 3 The phase curve of Uranus in IRIS data numbers (DN) Filled points are derived from IRIS radiometer data, error bars represent only random uncertainties. Open points and their error flags are from imaging data (Pollack *et al*. 1986), normalized by linear interpolation to the IRIS data point at 54° phase angle. The two datasets are quite consistent The solid curve is an interpolant derived by fitting the IRIS data alone (see text)

Modelling atmospheric reflection

Cloud structure => scattering by cloud particle

Parameters (spectrally resolved):

- scattering particle parameters : ϖ , phase function
- Size distribution function
- Atmospheric structure and molecular composition
- Radiative transfer with scattering

=> Fully determined physical model possible

Photometry of atmosphereless bodies

Fundamental difficulties !

Definition of a surface : not an analytical manifold !

Particulate surface : single scattering not convenient (particles are not isolated and interference between individual particles cannot be neglected)

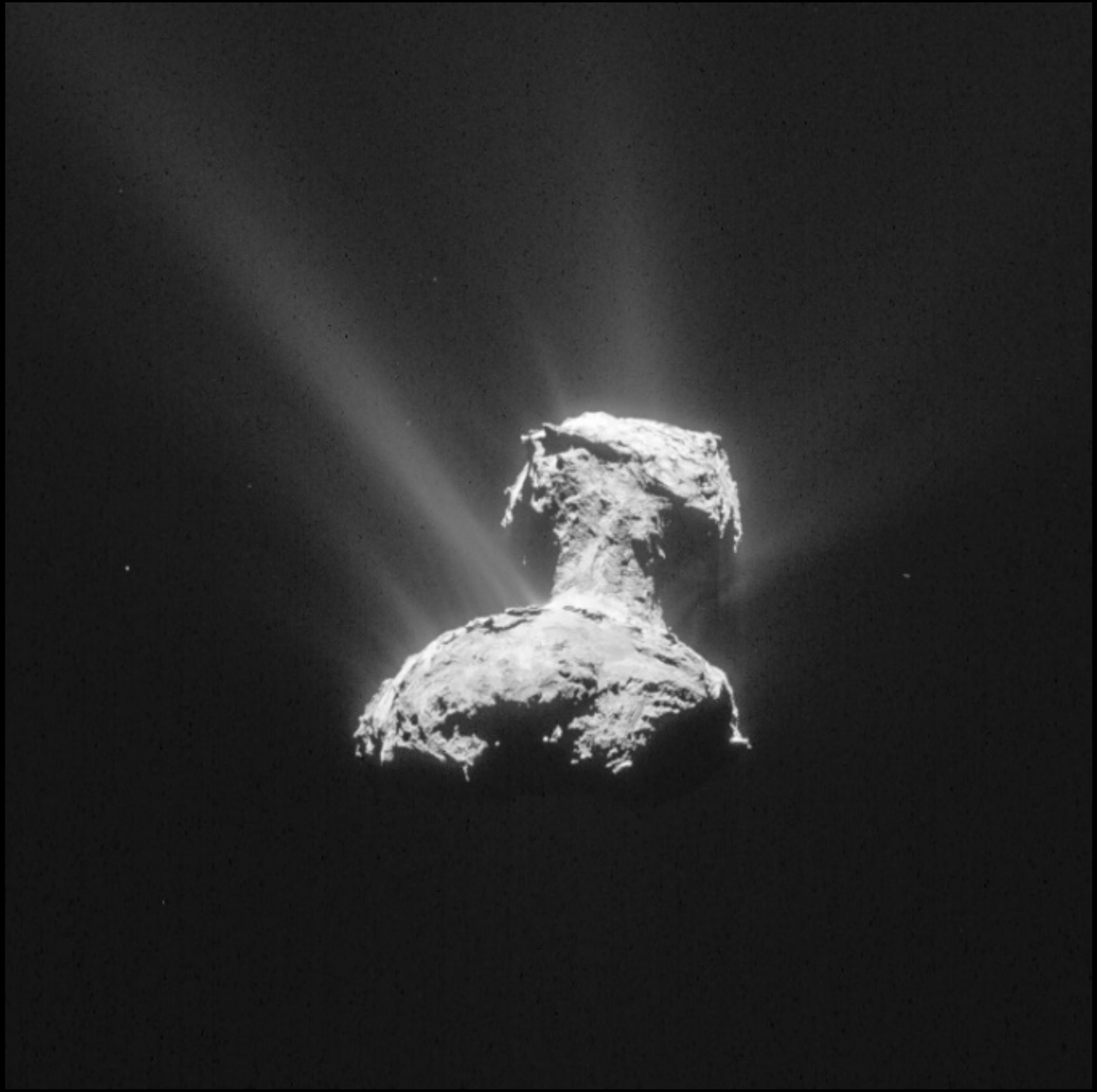

The Moon case

The moon phase curve is NOT even close to a lambertian surface !

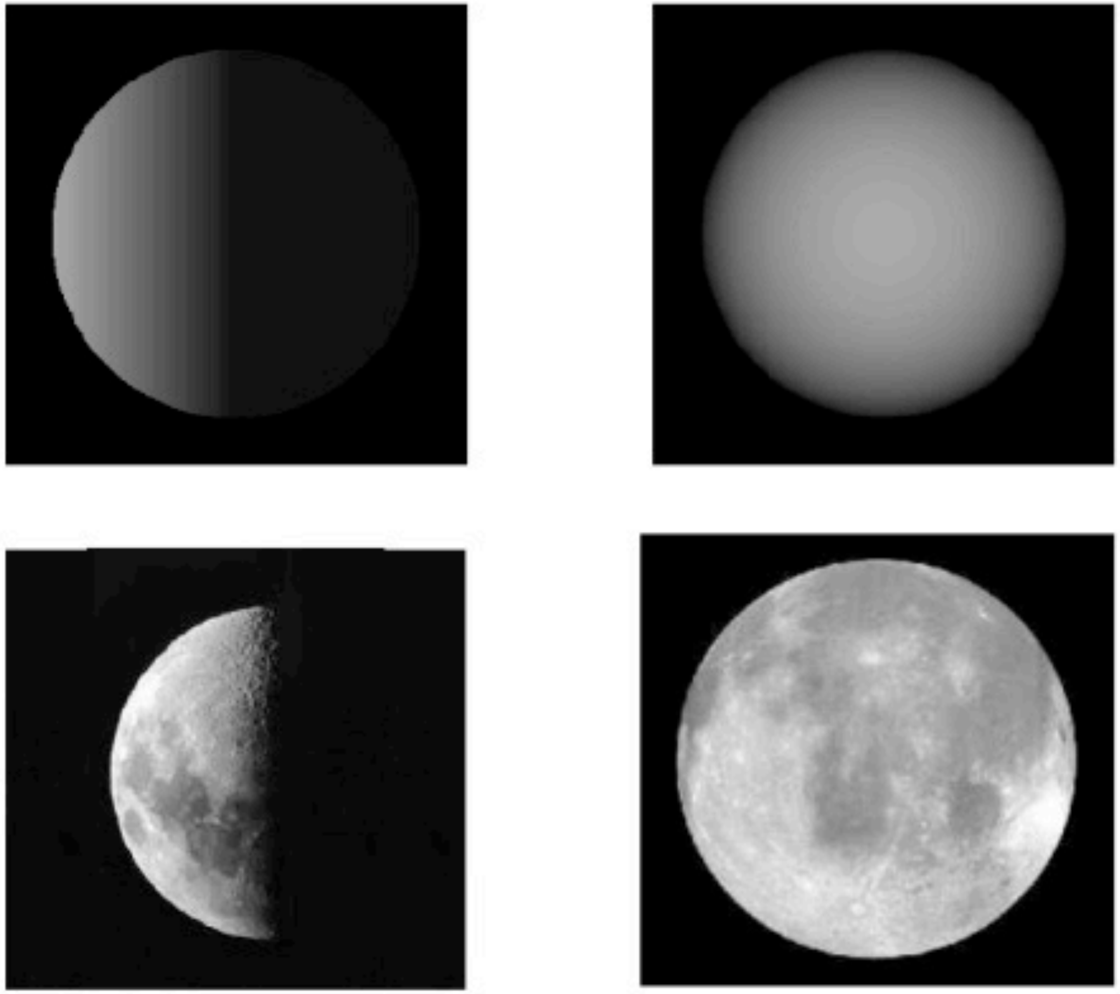

Lambertian Spheres and Moon Photos illuminated similarly

Model of phase function

The Hapke model(s) 1970-2012

$$R_n(\alpha, b, l) = \frac{\omega_n}{4\pi}[(1 + B_n(\alpha))P_n(\alpha) + M_n(\omega_n, \alpha, b, l)] \times \frac{\cos l \cos(l - \alpha) \cos b}{\cos l + \cos(l - \alpha)}.$$

"Hapke attributes the mutual dependence of the modeled regolith properties to a true property of nature and not a failure of his model." Li et al, 2015

Fractals are dark…

Construction of the Koch curve at step N = 6 and illumi- nated fraction for the conditions 0 = - 30.. 0, = -+ 30 (Drossart, Planet. Space Sci., 1993)

=> Increasing N, the radiance decreases exponentially as $(2/3)^n$

Extensive theory for quasi-fractal surfaces :

Shkuratov & Helfenstein, Icarus 2001

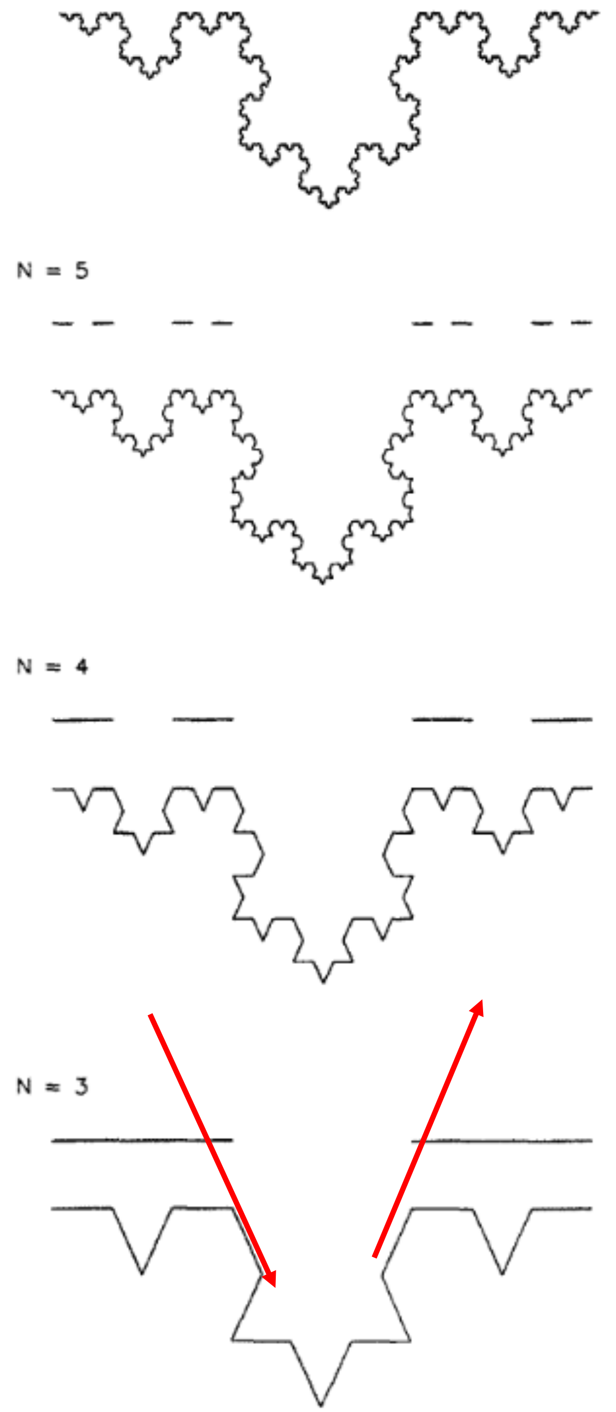

Model of phase function

The Hapke model(s) 1970-2012

$$R_n(\alpha, b, l) = \frac{\omega_n}{4\pi}\left[(1 + B_n(\alpha))P_n(\alpha) + M_n(\omega_n, \alpha, b, l)\right] \times \frac{\cos l \cos(l-\alpha)\cos b}{\cos l + \cos(l-\alpha)}.$$

Shkuratov approach (Shkuratov and Helfenstein, 1991)

Fractal approach Only 4 parameters:

ϖ h , L , q

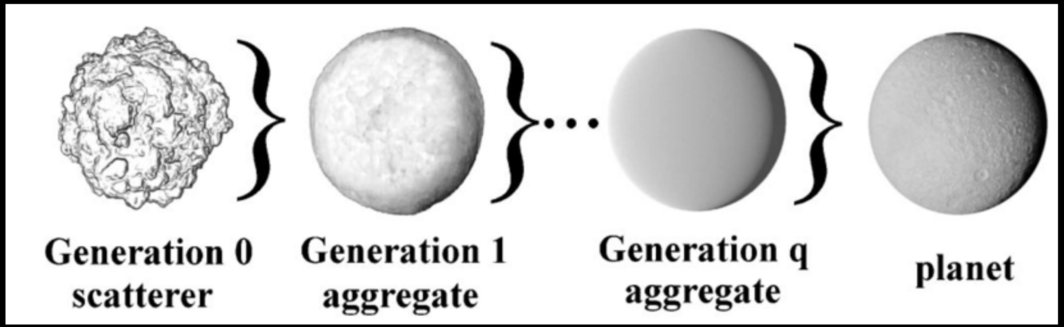

Extension to exoplanets

- Dyudina et al, ApJ 2016. REFLECTED LIGHT CURVES, SPHERICAL AND BOND ALBEDOS OF JUPITER- AND SATURN-LIKE EXOPLANETS

We estimate how the light curve and total stellar heating of a planet depends on forward and backward scattering in the clouds based on Pioneer and Cassini spacecraft images of Jupiter and Saturn. We fit analytical functions to the local reflected brightnesses of Jupiter and Saturn depending on the planet's phase. These observations cover broadbands at 0.59-0.72 and 0.39-0.5 µm, and narrowbands at 0.938 (atmospheric window), 0.889 (CH_4 absorption band), and 0.24-0.28 µm. We simulate the images of the planets with a ray-tracing model, and disk-integrate them to produce the full-orbit light curves. For Jupiter, we also fit the modeled light curves to the observed full-disk brightness. We derive spherical albedos for Jupiter and Saturn, and for planets with Lambertian and Rayleigh-scattering atmospheres. Jupiter-like atmospheres can produce light curves that are a factor of two fainter at half-phase than the Lambertian planet, given the same geometric albedo at transit.

1st Intermezzo : the true colors of planets

Source : Ellen,

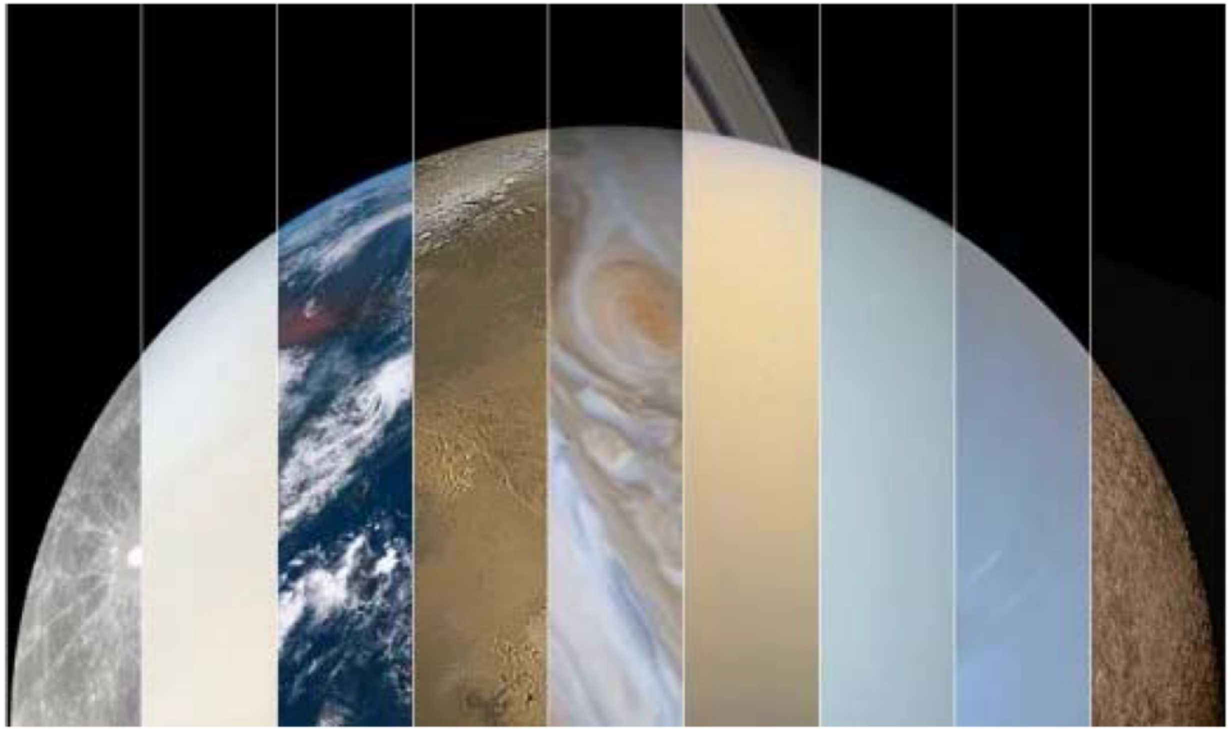

True-Color solar system collage: Mercury, Venus, Earth, Mars, Jupiter, Saturn, Uranus, Neptune, Pluto. (Wish I could add Ceres and Eris, but we don't yet have hi-res color photos of them.) | Source

Mercury

Right: Mercury MESSENGER spacecraft captures color in visible and near-infrared wavelengths. Left: NASA scientists adjust the original false-color inage to show colors to approximate what the human eye would see.

Surface conditions

Earth-Lighting vs. True-Color Martian Landscape

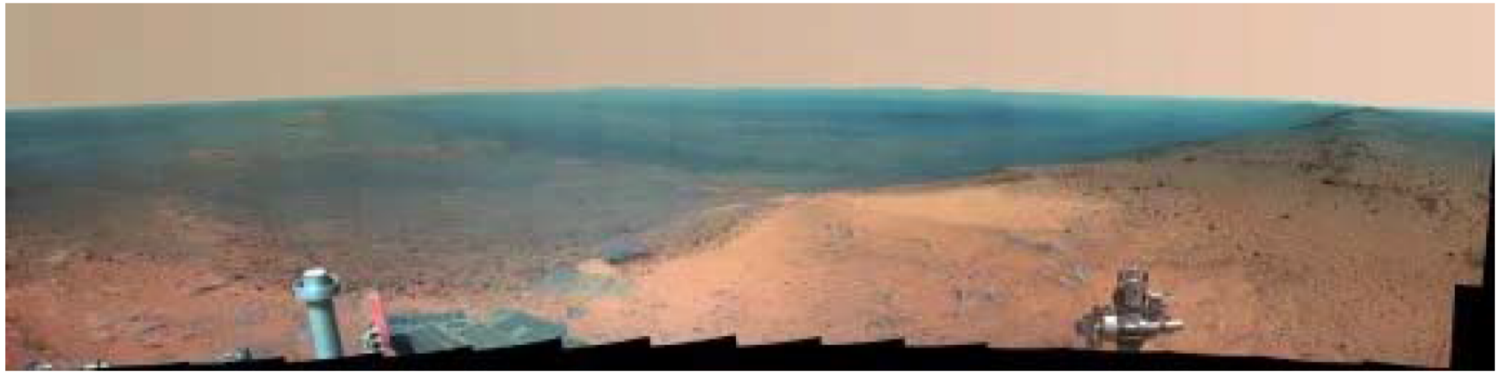

Mars Opportunity Rover panorama, January 2015. This is appoximately what this spot would look like under Earth lighting conditions. [NASA/JPL-Caltech/Cornell Univ./Arizona State Univ.] | Source

Mars Opportunity Rover panorama, January 2015. This is what it would look like if you were actually standing there. [NASA/JPL-Caltech/Cornell Univ./Arizona State Univ.] | Source

Martian sunsets

On May 19th, 2005, NASA's Mars Exploration Rover Spirit captured this stunning view as the Sun sank below the rim of Gusev crater on Mars.

Part 2. Polarization

Electromagnetic wave property

- e.m. waves are not scalar waves !

⇒Full radiative transfer equations should take into account the electric field vectorial nature

$\Rightarrow \vec{E} = E_l \vec{l} + E_r \vec{r}$

2. Polarization

Definition of the Stokes parameters

I, Q, U, V = full characterization of the most general polarization state of light

$I = E_l E_l^* + E_r E_r^*$

$Q = E_l E_l^* - E_r E_r^*$ Linear polarization U=V=0

$U = E_l E_r^* + E_r E_l^*$ Circular polarization V =Q =0

$V = i\,(E_l E_r^* - E_r E_l^*)$

For a coherent solution of Maxwell equation : $I^2 = Q^2+U^2+V^2$ (fully polarized) – partially polarized light : $I^2 > Q^2+U^2+V^2$

Basic applications

Single scattering calculations : some examples

- Atmosphere : Rayleigh scattering
- Clouds : Mie scattering
- Surface : radiative transfer on complex surfaces

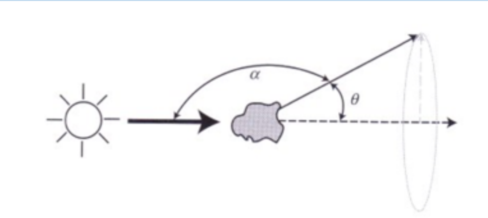

Radiative transfer with polarization – doubling adding methods

Rayleigh scattering

- Formulae

Polarizability : $\vec{p} = \alpha \, \vec{E}_0$

Scattering matrix [S] = $\begin{bmatrix} \cos\theta & 0 \\ 0 & 1 \end{bmatrix}$

Properties :

- $E = k^2 \, p \sin\gamma \, e^{ikr}/r$
- $C_{sca} = 8\pi/3 \quad k^4 \, |\alpha|^2$
- Scattered intensity : $I = \dfrac{(1 + \cos^2\theta) \, k^4 |\alpha|^2 \, I_0}{2 \, r^2}$

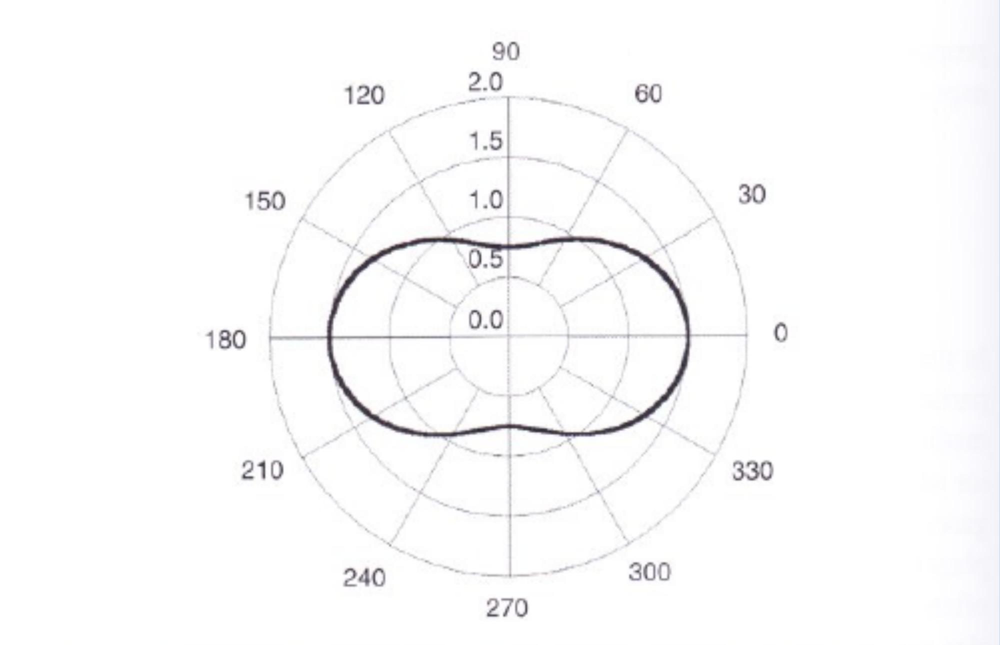

Mars

Coulson KL Appl Opt. 1969 Jul 1;8(7):1287-94. doi: 10.1364/AO.8.001287.**Polarimetry of Mars.**

Abstract

A summary of results of observations of the polarization of Mars shows that surface pressure determinations from these data have not yielded satisfactory results in spite of the extensive number of observations available. It is suggested that the difficulty lies mainly in the neglect of radiative components resulting from a combination of diffuse transmission and surface reflection, the effects of an unknown and variable aerosol component of the atmosphere, and the concentration of the observations in the longer visible wavelengths corresponding to very small atmospheric optical thicknesses. Computations of atmospheric effects to be expected from various Rayleigh and aerosol models of the atmosphere show that the polarizing effects of realistic aerosol models can vary widely, depending on particle parameters, and that polarization due to Rayleigh scattering by representative models of the Martian atmosphere can only serve to shift the position of the neutral point to smaller phase angles and to shift the polarization curve in the positive direction from its position for only the surface-reflected radiation. …

HST observations of Martian polarization

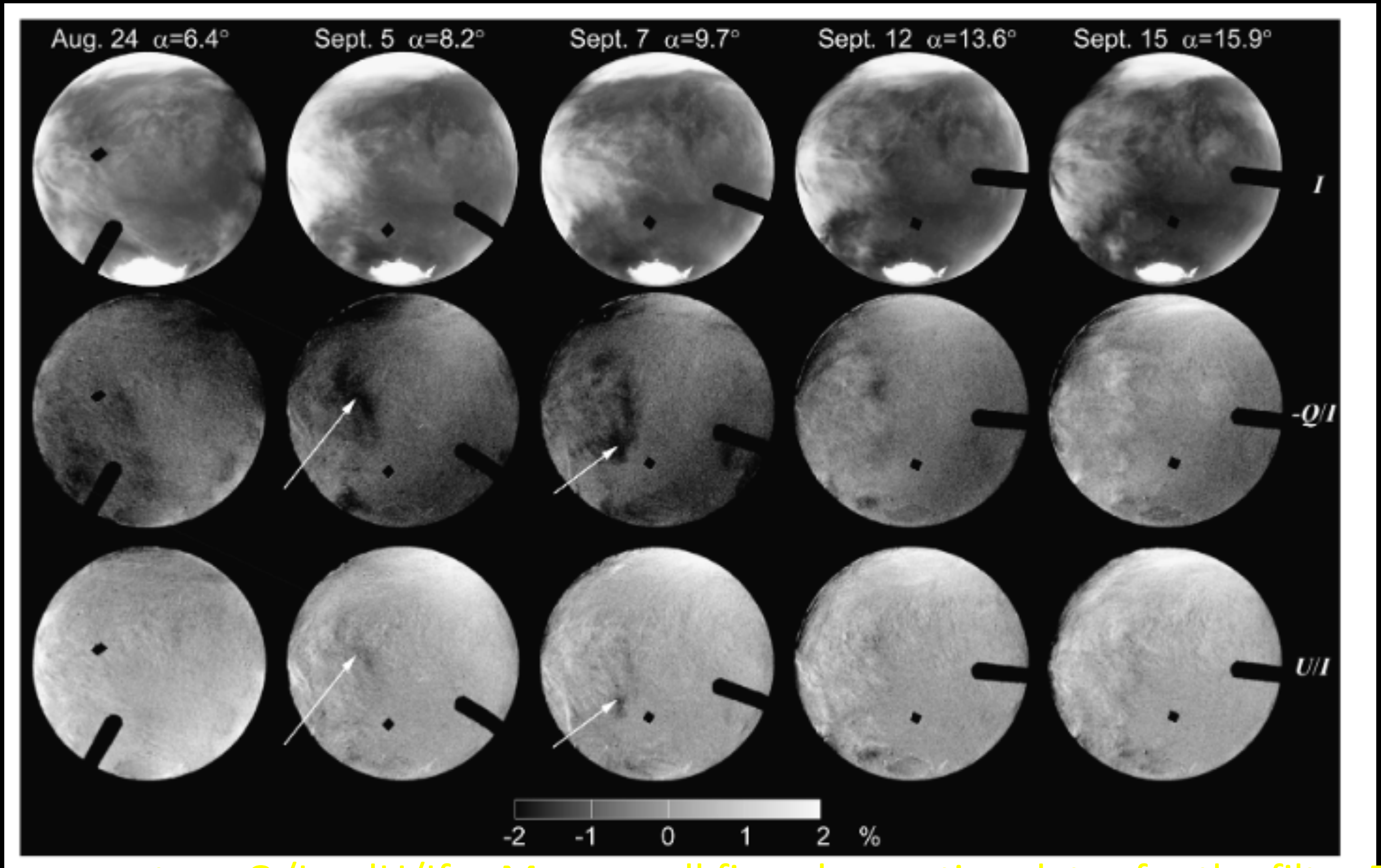

Intensity and normalized Stokes parameters−Q/IandU/Ifor Mars on all five observation dates for the filter F250W. The Stokes parameters aredefined with respect to the photometric-equator-related reference frame. The black coronographic finger and spot are shadowed areas of the detector. Thearrows show the polarimetric transient effect Shkuratov et al, Icarus, 2005

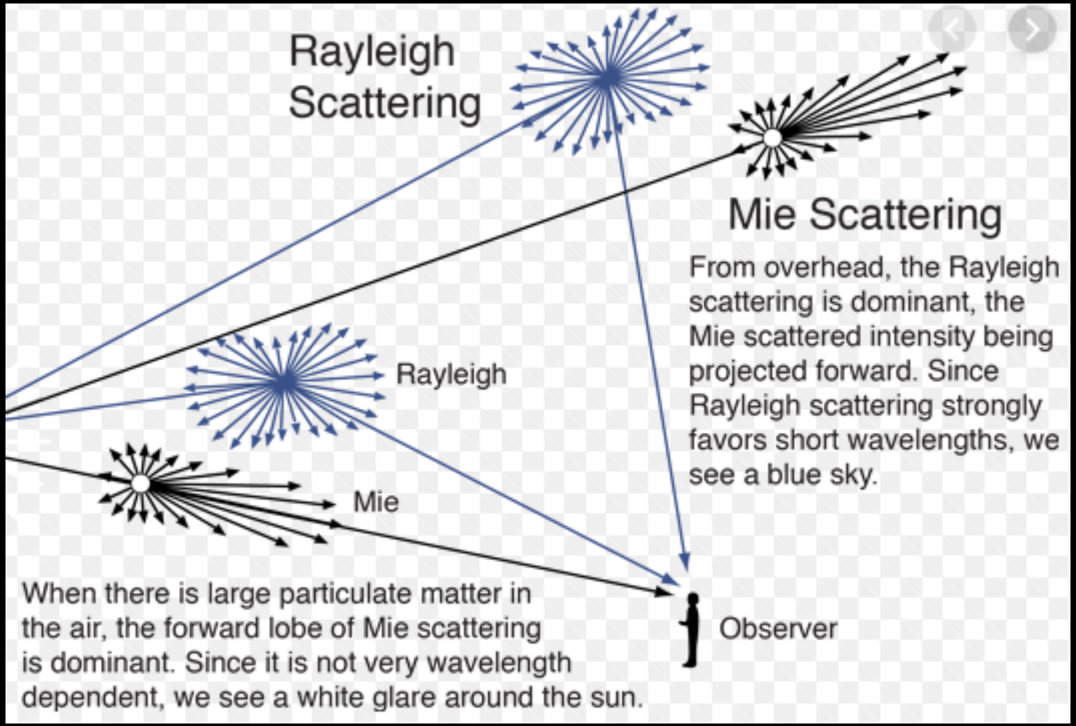
Rayleigh
Scattering
Mie Scattering
From overhead, the Rayleigh scattering is dominant, the Mie scattered intensity being projected forward. Since Rayleigh scattering strongly favors short wavelengths, we see a blue sky.
Rayleigh
Mie
Observer
When there is large particulate matter in the air, the forward lobe of Mie scattering is dominant. Since it is not very wavelength dependent, we see a white glare around the sun.

Scattering by small particles

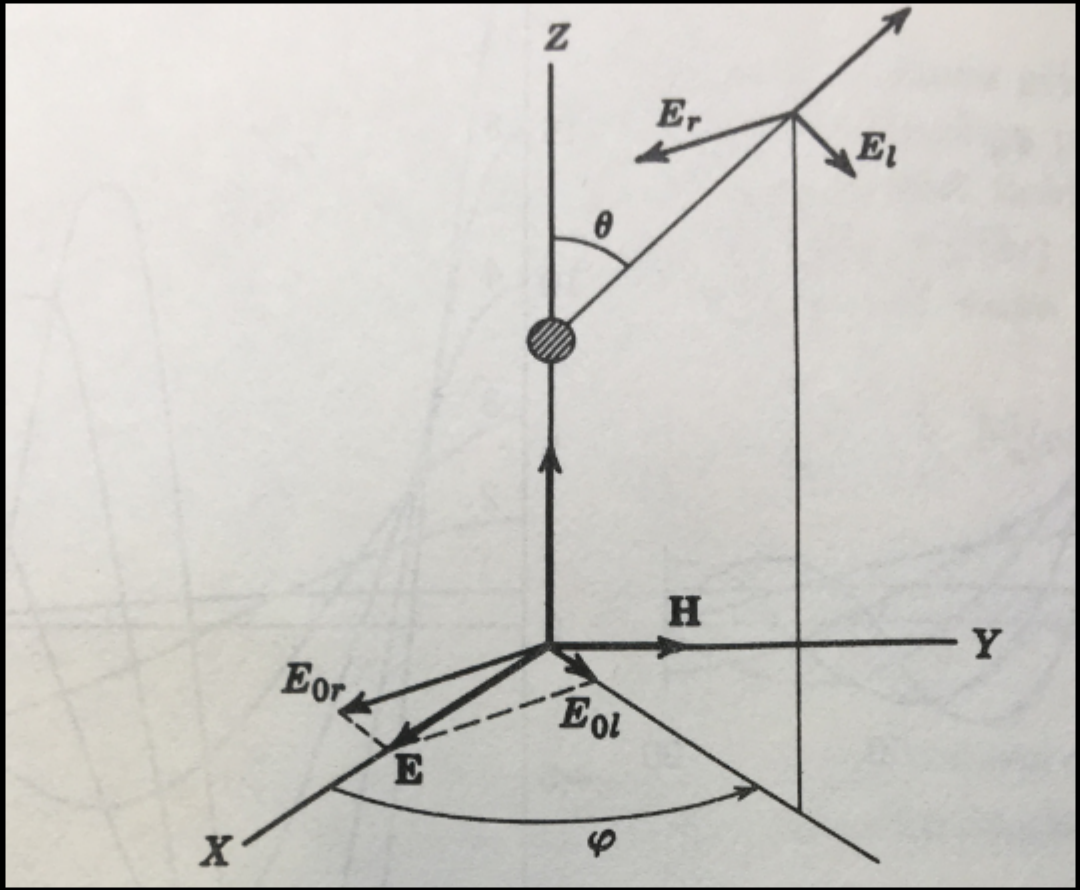

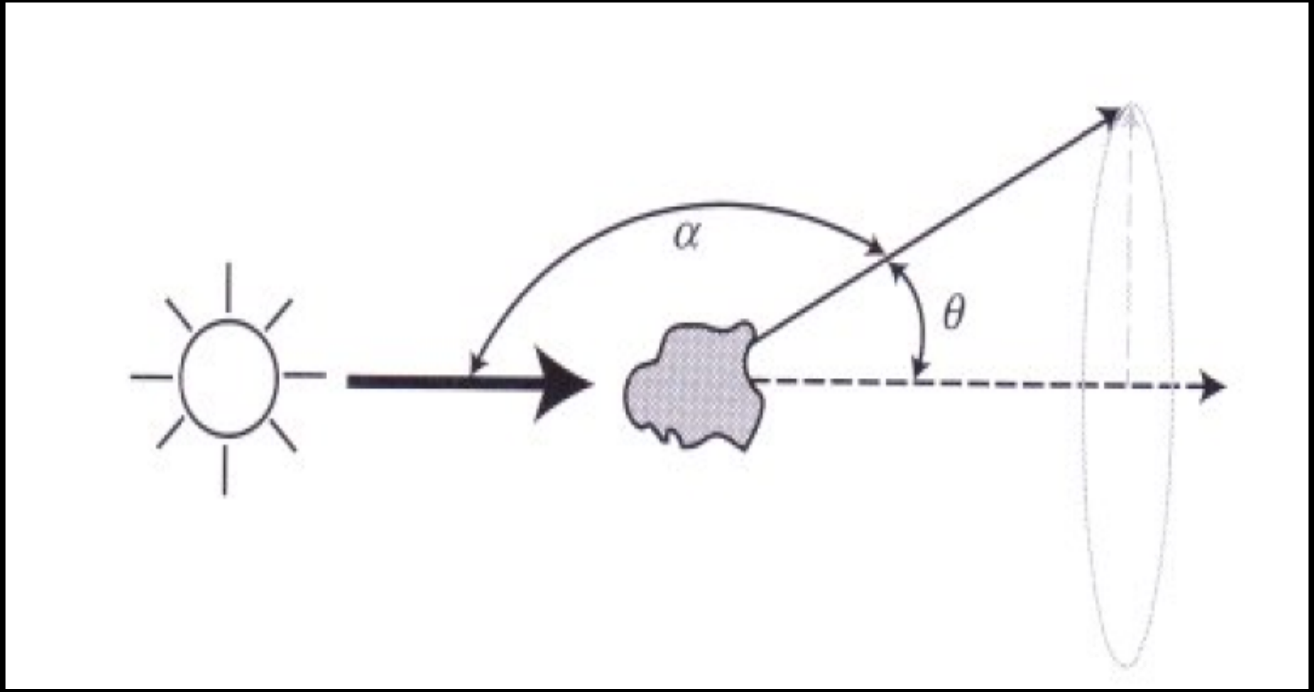

Mie scattering

- Formulae

$$\begin{pmatrix} E_l^s \\ E_r^s \end{pmatrix} = \frac{\exp(-ikr+ikz)}{ikr} \begin{pmatrix} S_2 & S_3 \\ S_4 & S_1 \end{pmatrix} \begin{pmatrix} E_l^i \\ E_r^i \end{pmatrix}$$

$$S_1(\theta) = \sum_{n=1}^{\infty} \frac{2n+1}{n(n+1)} \{a_n \pi_n(\cos\theta) + b_n \pi_n(\cos\theta)\}$$

$$S_2(\theta) = \sum_{n=1}^{\infty} \frac{2n+1}{n(n+1)} \{a_n \tau_n(\cos\theta) + b_n \pi_n(\cos\theta)\}$$

- properties

$$\pi_n(\cos\theta) = \frac{P_n^1(\cos\theta)}{\sin\theta}, \qquad \tau_n(\cos\theta) = \frac{d}{d\theta} P_n^1(\cos\theta),$$

Phases of Venus

Observations of Venus at Pic du Midi

Allows to observe polarization along all phase angles

Image	Index	Date	Time	LCM [°]	λ [°]	Filter	Observatory
	7823	1966-03-10	05:32:00	0.00	195.98	UV	Pic
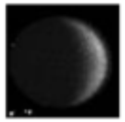	7824	1966-03-11	07:13:00	0.00	197.70	UV	Pic
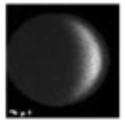	7825	1966-03-12	06:38:00	0.00	199.28	UV	Pic
	7826	1966-03-13	06:06:00	0.00	200.85	UV	Pic
	7827	1966-03-15	06:14:00	0.00	204.08	UV	Pic
	7828	1966-03-16	06:25:00	0.00	205.70	UV	Pic
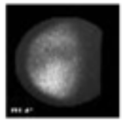	7834	1966-05-28	07:20:00	0.00	321.74	UV	Pic
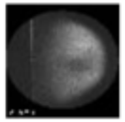	7838	1966-06-02	06:45:00	0.00	329.62	UV	Pic
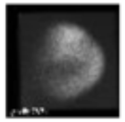	7874	1966-07-09	10:23:00	0.00	28.71	UV	Pic
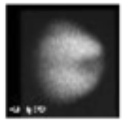	7881	1966-07-12	06:12:00	0.00	33.22	UV	Pic

Article : Hansen & Hovenier Venus, 1974

Interpretation of the Polarization of Venus

JAMES E. HANSEN

Goddard Institute for Space Studies, New York, N. Y. 10025

J. W. HOVENIER

Dept. of Physics and Astronomy, Free University, Amsterdam, Netherlands

(Manuscript received 20 November 1973, in revised form 15 January 1974)

ABSTRACT

The linear polarization of sunlight reflected by Venus is analyzed by comparing observations with extensive multiple scattering computations. The analysis establishes that Venus is veiled by a cloud or haze layer of spherical particles. The refractive index of the particles is 1.44±0.015 at $\lambda=0.55$ µm with a normal dispersion, the refractive index decreasing from 1.46±0.015 at $\lambda=0.365$ µm to 1.43±0.015 at $\lambda=0.99$ µm. The cloud particles have a narrow size distribution with a mean radius of ~1 µm; specifically, the effective radius of the size distribution is 1.05±0.10 µm and the effective variance is 0.07±0.02. The particles exist at a high level in the atmosphere, with the optical thickness unity occurring where the pressure is about 50 mb.

The particle properties deduced from the polarization eliminate all but one of the cloud compositions which have been proposed for Venus. A concentrated solution of sulfuric acid (H_2SO_4-H_2O) provides good agreement with the polarization data.

Retrieval of cloud scattering parameters

Refractive index : m=n-ir

Size distribution with r~1 µm and b=0.045

Atmospheric Rayleigh contribution

Compatible with H_2SO_4 cloud particles

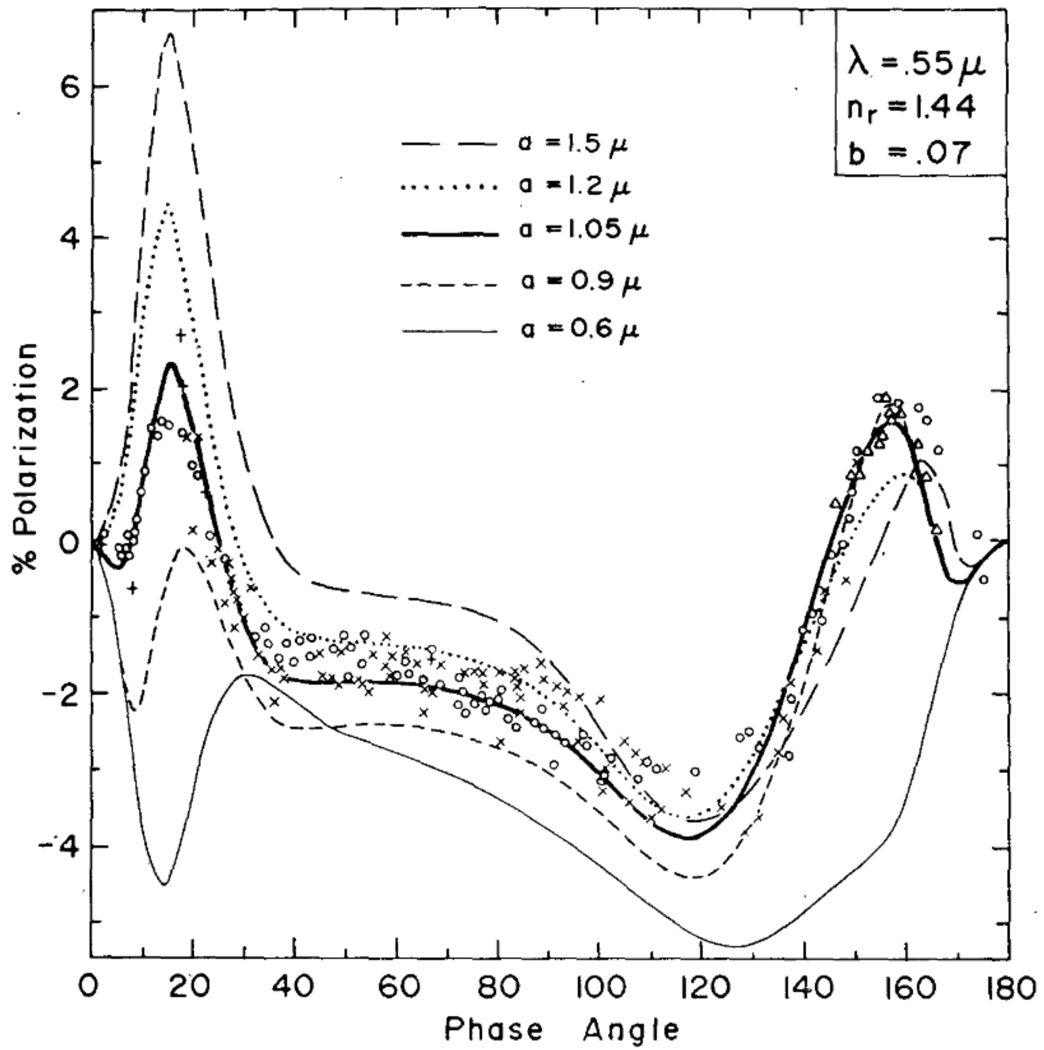

FIG. 4. Observations of the polarization of sunlight reflected by Venus in the visual wavelength region and theoretical computations for $\lambda = 0.55$ μm. The ○'s are wide-band visual observations by Lyot (1929) while the other observations are for an intermediate bandwidth filter centered at $\lambda = 0.55$ μm; the ×'s were obtained by Coffeen and Gehrels (1969), the +'s by Coffeen (cf. Dollfus and Coffeen, 1970), and the Δ's (which refer to the central part of the crescent) by Veverka (1971). The theoretical curves are all for a refractive index 1.44, the size distribution (8) with $b = 0.07$, and a Rayleigh contribution $f_R = 0.045$. The different curves show the influence of the effective radius on the polarization.

Spatial variations – clouds & hazes

Clouds or haze behave differently for polarization

- Multiple scattering tends to lower polarization, due to integration over all directions
- Clouds with large optical depth give low polarization effects
- Hazes optically thin (Mars, Jupiter) on the contrary can exhibit polarization

Jupiter in polarized light

Cassini Huygens,

Wide angle camera with
CH4 filter + polarizer
Closest approach in 2000

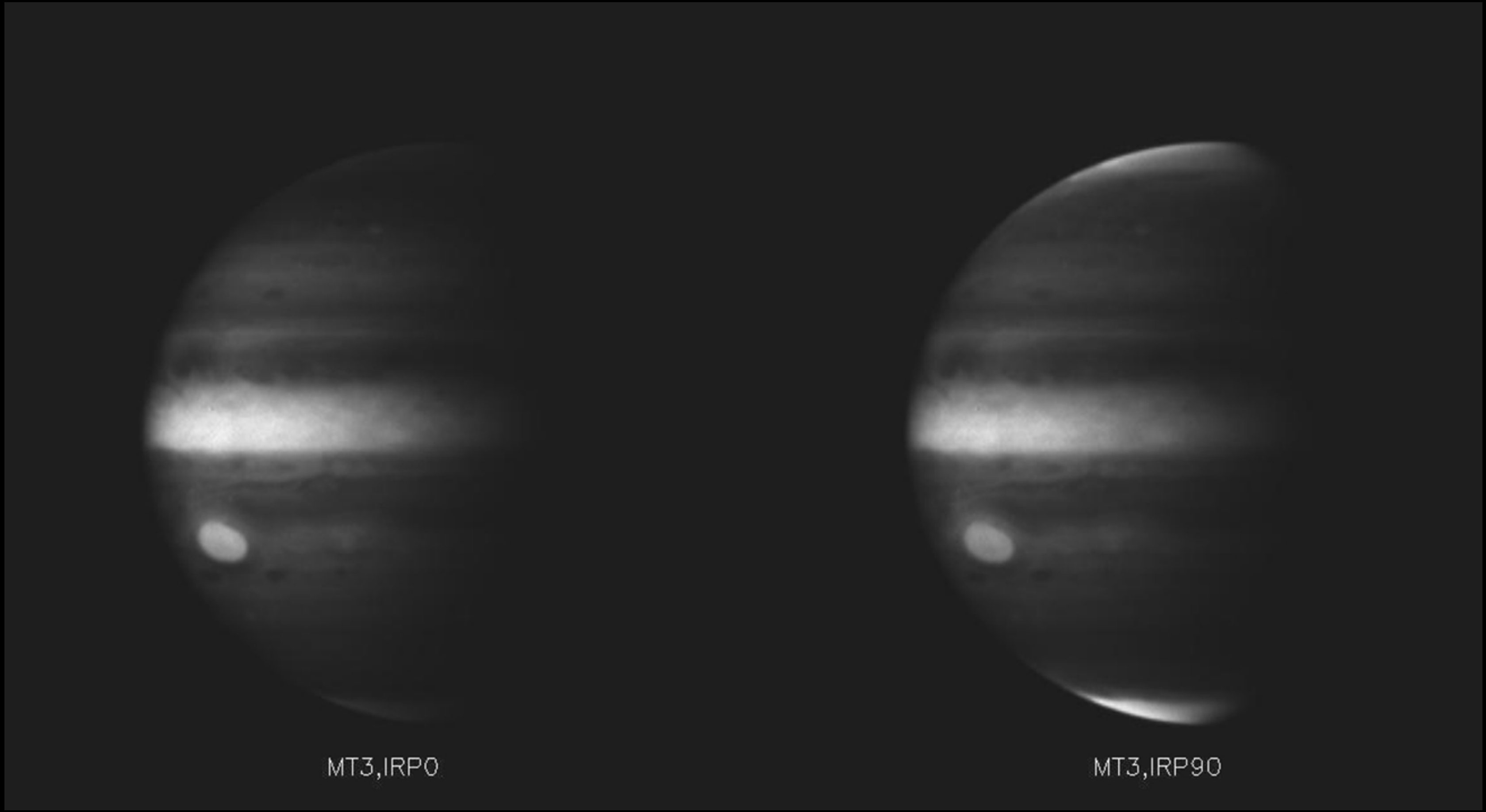

Poles appear bright in one image, and dark in the other. Polarized light is most readily scattered by aerosols. These images indicate that the aerosol particles at Jupiter's poles are small and likely consist of aggregates of even smaller particles, whereas the particles at the equator and covering the Great Red Spot are larger.

Scattering models for non-spherical particles

Difficulties with calculations…

DDA numerical models (Wiscombe and Mugnai, 1988)

Empirical Models : Drossart, 1991

Differences between phase functions of Mie and an irragular model (incoherent Mie scattering)

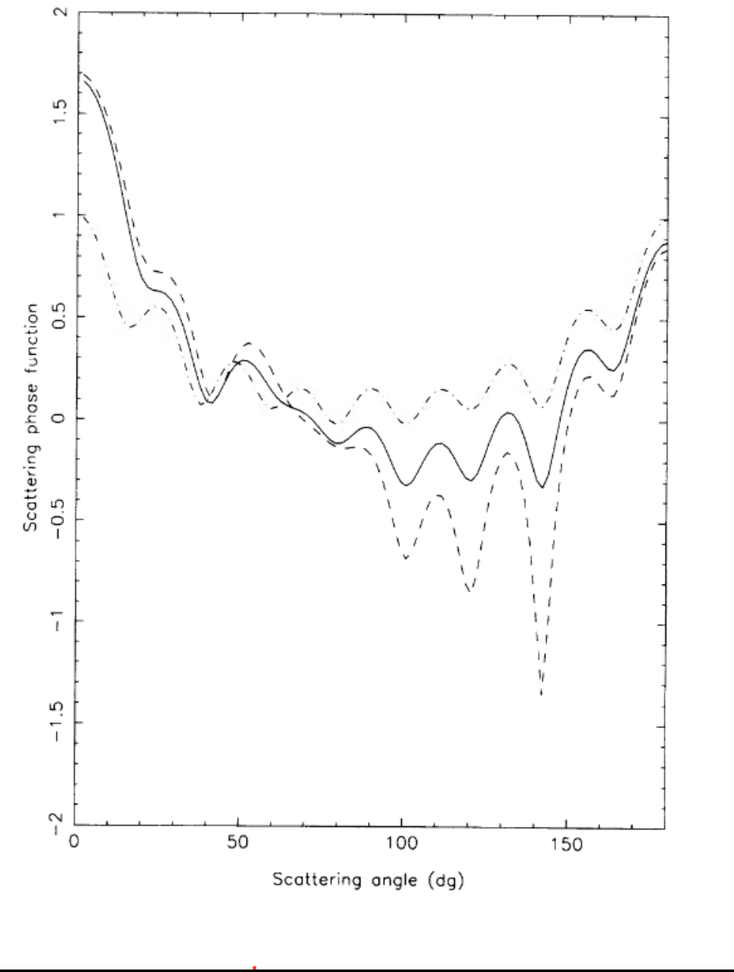

Polarization for atmosphereless bodies

Relation with opposition peak ofo low phase angle variations in albedo

(negative polarization peak)

Abundant littérature on the subject !

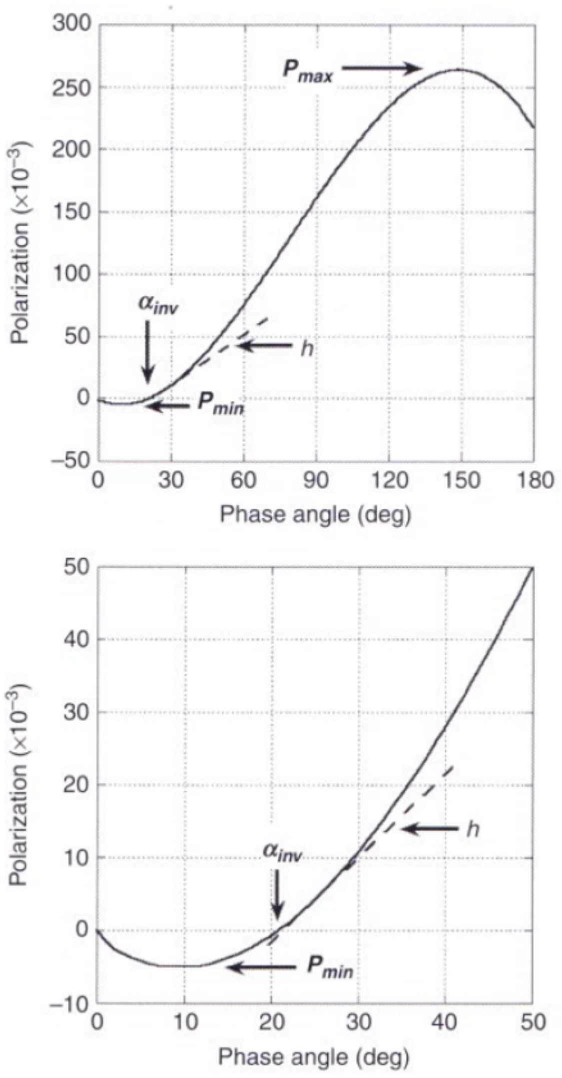

Figure 6.8. A representative polarization phase curve with the major parameters of interest noted. The top figure shows the entire curve, the bottom figure is an enlargement and covers the range of phase angles available for most solar system objects.

Credit: Michael K. Shepard.

2d Intermezzo : rayleigh scattering and color

single scattering function => blue sky

λ^{-4} dependence of scattering in the Rayleigh cross section.

Polarization of the sky follows the Rayleigh scattering law – still present through cloud coverage

Semi-infinite atmosphere with pure Rayleigh scattering (assuming no absorption) : white!

Part 3. Atmospheric escape

Problematics :

Model of atmospheric escape, time constants, physical models

Historical perspective:

Chamberlain, 1960 ; Parker 1963

Objects : planets, Titan, Pluto - comets

Prerequisite

- Hydrostatic atmosphere : atmospheric scale height
- Homopause : eddy / molecular diffusion competition
- Exobase : mean free path vs atmospheric scale height

Hydrostatic atmosphere

- Equation of hydrostatic equilibrium

=> Scale height H=RT/Mg

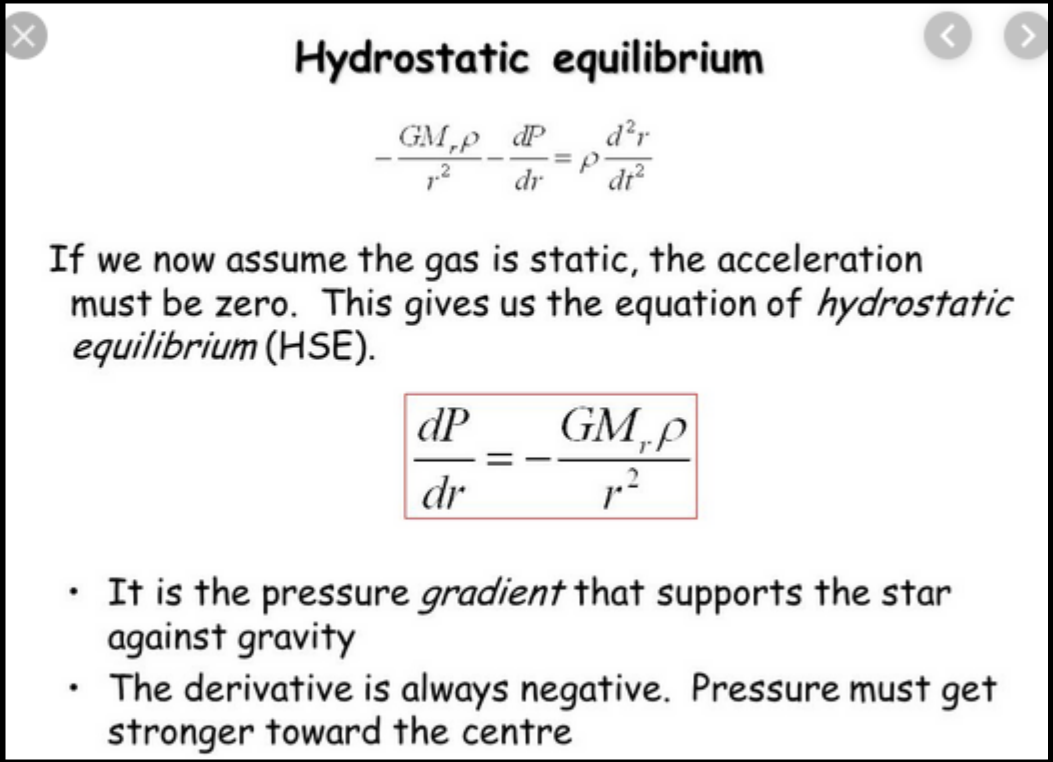

Hydrostatic equilibrium

$$-\frac{GM_r\rho}{r^2}-\frac{dP}{dr}=\rho\frac{d^2r}{dt^2}$$

If we now assume the gas is static, the acceleration must be zero. This gives us the equation of *hydrostatic equilibrium* (HSE).

$$\frac{dP}{dr}=-\frac{GM_r\rho}{r^2}$$

- It is the pressure *gradient* that supports the star against gravity
- The derivative is always negative. Pressure must get stronger toward the centre

Definition of homopause

$$\phi_i = n_i\left[-D_i\left(\frac{1}{n_i}\frac{dn_i}{dz}+\frac{1}{H_i}+\frac{1}{T}\frac{dT}{dz}\right)-K\left(\frac{1}{n_i}\frac{dn_i}{dz}+\frac{1}{H_a}+\frac{1}{T}\frac{dT}{dz}\right)\right]$$

$$n_i(z) = n_i(z_0)(T_0/T)\exp\left(-\int_{z_0}^{z} dz/H_i\right)$$

With $H = RT/MG$ M_i = constituent i
M_a = mean molecular mass
K eddy diffusion coefficient
D_i kinetic diffusion coefficient for i
T temperature

Homopause K ~D
Below : K dominent – above D dominent

Atreya, Atmospheres and Ionospheres of planets and their satellites, Springer, 1986

Jupiter CH_4 measurement

Contrary to Saturn, on Jupiter, the eddy diffusion coefficient is low enough to put the homopause of CH_4 below the main photodissociation level

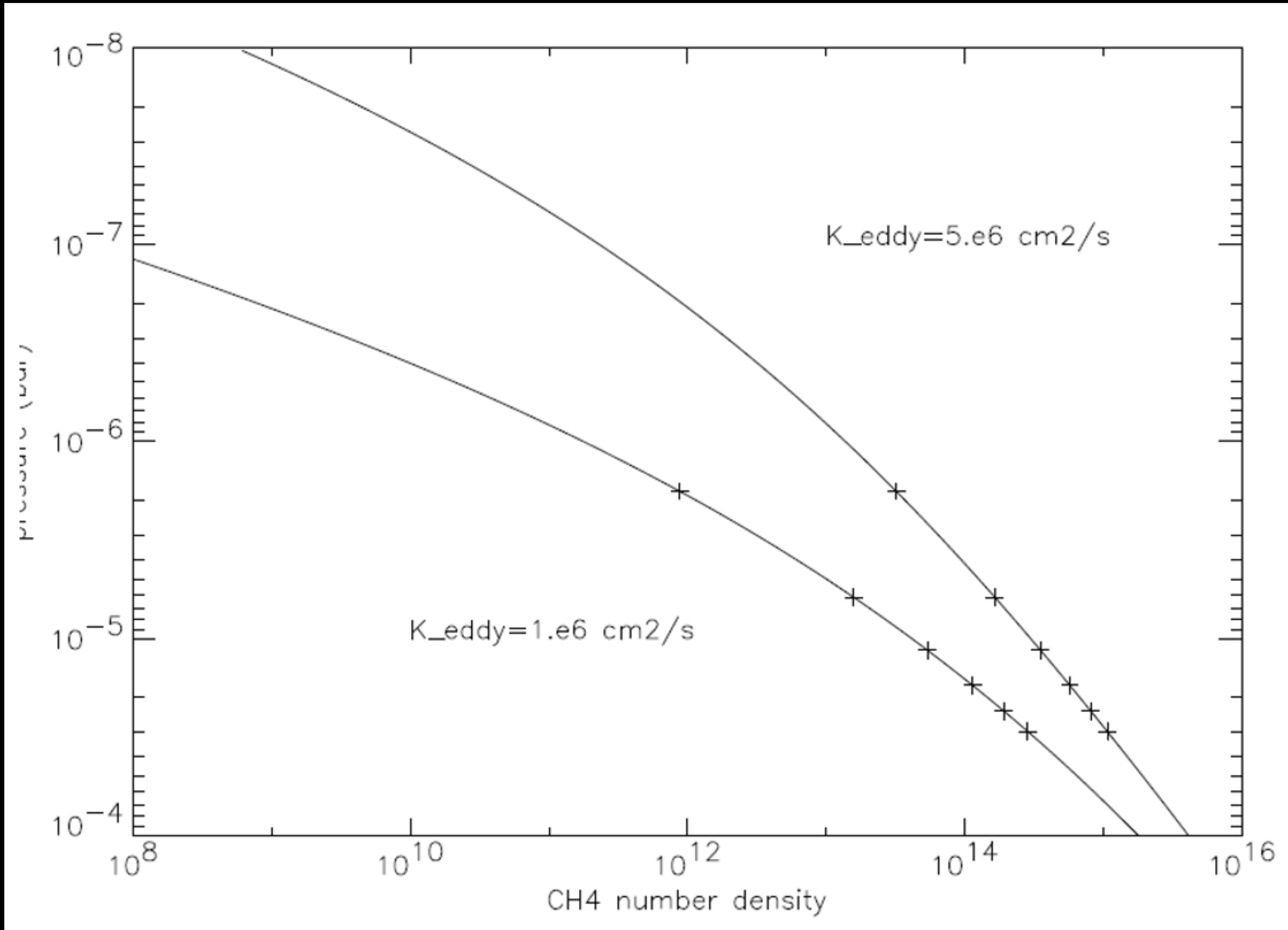

Exobase and escape

Fundamental parameters : Kn and J

- Knudsen parameter : l / H

l = mean free path / H = atmospheric scale height

- Jeans parameter : gravitational energy/thermal energy = r/H = v_{esc}/u(r)

Where u(r)=sqrt(2kT/m) and v_{esc} = sqrt(2 G M/r)

Different regimes K <<1 => hydrodynamic escape

K >~1 : Jeans escape (or molecule by molecule escape)

Exobase : l~H or Kn ~ 1

Kinetic theory of gases

Boltzmann equation

$$\frac{\partial f_s}{\partial t} + \bar{v}_s \cdot \nabla f_s + \ddot{g} \cdot \nabla_{v_s} f = \left(\frac{\delta f_s}{\delta t} \right)$$

The only rigorous approach when hydrodynamical equations fail (Kn > 0.2) !

Jeans escape : kinetic escape

Analytical calculation of the distribution function possible, with some assumptions:

- No collision above exosphere
- Distribution function = truncated maxwellian
- Consequence : column density above the exobase ~ n0 x H
- Escape flux calculation :

Hydrodynamical escape

Thermal heating equation

Reduced to a Bernoulli

Equation

$$\frac{1}{2}v^2 + c_p T + \Phi_g \approx c_p T_0 + \Phi_{g0}$$

Validity in hydrodynamical regime (Kn << 1 ; l < 1)

Transition between Hydrodynamical/Jeans regimes

Monte-Carlo models

Cf : Volkov seminal papers

Phys. Fluids, 2011

ApJ Lett. 2011

THERMALLY DRIVEN ATMOSPHERIC ESCAPE: TRANSITION FROM HYDRODYNAMIC TO JEANS E

ALEXEY N. VOLKOV[1], ROBERT E. JOHNSON[1,2], ORENTHAL J. TUCKER[1], AND JUSTIN T. ERWIN[1]
[1] Materials Science and Engineering Department, University of Virginia, Charlottesville, VA 22904-4745, USA
[2] Physics Department, New York University, NY 10003-6621, USA
Received 2010 October 1; accepted 2011 January 25; published 2011 February 16

ABSTRACT

Thermally driven escape from planetary atmospheres changes in nature from an organized outflow (hydrodynamic escape) to escape on a molecule-by-molecule basis (Jeans escape) with increasing Jeans parameter, λ, the ratio of the gravitational to thermal energy of the atmospheric molecules. This change is described here for the first time using the direct simulation Monte Carlo method. When heating is predominantly below the lower boundary of the simulation region, R_0, and well below the exobase of a single-component atmosphere, the nature of the escape process changes over a surprisingly narrow range of Jeans parameters, λ_0, evaluated at R_0. For an atomic gas, the transition occurs over $\lambda_0 \sim 2$–3, where the lower bound, $\lambda_0 \sim 2.1$, corresponds to the upper limit for isentropic, supersonic outflow. For $\lambda_0 > 3$ escape occurs on a molecule-by-molecule basis and we show that, contrary to earlier suggestions, for $\lambda_0 > \sim 6$ the escape rate does not deviate significantly from the familiar Jeans rate. In a gas composed of diatomic molecules, the transition shifts to $\lambda_0 \sim 2.4$–3.6 and at $\lambda_0 > \sim 4$ the escape rate increases a few tens of percent over that for the monatomic gas. Scaling by the Jeans parameter and the Knudsen number, these results can be applied to thermally induced escape of the major species from solar and extrasolar planets.

Titan & Pluto case : 30 years of atmospheric studies

Atmospheric Escape

Darrell F. Strobel

Johns Hopkins University

Submission version July 19, 2019

Of the historic solar system planets with surface pressures exceeding 1 μbar, Pluto's atmosphere was the least gravitationally bound, and originally thought to be escaping hydrodynamically or even unstable against blowoff. But when constrained by available solar power, estimated escape rates were in the range of (1-10) × 10^{27} molecules s^{-1}. Our actual knowledge of escape rates is limited to the period of the New Horizons (NH) flyby in July 2015, when Pluto was post-perihelion at ~ 32.9 AU from the Sun. The NH data yielded a cold, compact upper atmosphere with escape rates of N_2 = (3-8) × 10^{22} s^{-1} and CH_4 = (4-8) × 10^{25} s^{-1}, for a total of ~ 10^{27} amu s^{-1}, at very subsonic velocities rendering the atmosphere essentially hydrostatic. For Charon the NH upper limits on probable N_2 and CH_4 atmospheres yield solar power limited escape rates of ~ 1 × 10^{25} molecule s^{-1}.

Extensions

- Multicomponent atmospheres
- Non thermal escape mechanisms

Charge exchange

Meteoritic erosion

Mars escape

Maven mission

- Hydrogen in Mars' upper atmosphere comes from water vapor in the lower atmosphere. An atmospheric water molecule can be broken apart by sunlight, releasing the two hydrogen atoms from the oxygen atom that they had been bound to. Several processes at work in Mars' upper atmosphere may then act on the hydrogen, leading to its escape.
- This image shows atomic hydrogen scattering sunlight in the upper atmosphere of Mars, as seen by the Imaging Ultraviolet Spectrograph on NASA's Mars Atmosphere and Volatile Evolution mission. About 400,000 observations, taken over the course of four days shortly after the spacecraft entered orbit around Mars, were used to create the image. Hydrogen is produced by the breakdown of water, which was once abundant on Mars' surface. Because hydrogen has low atomic mass and is weakly bound by gravity, it extends far from the planet (the darkened circle) and can readily escape.
- Credits: NASA/Goddard/University of Colorado

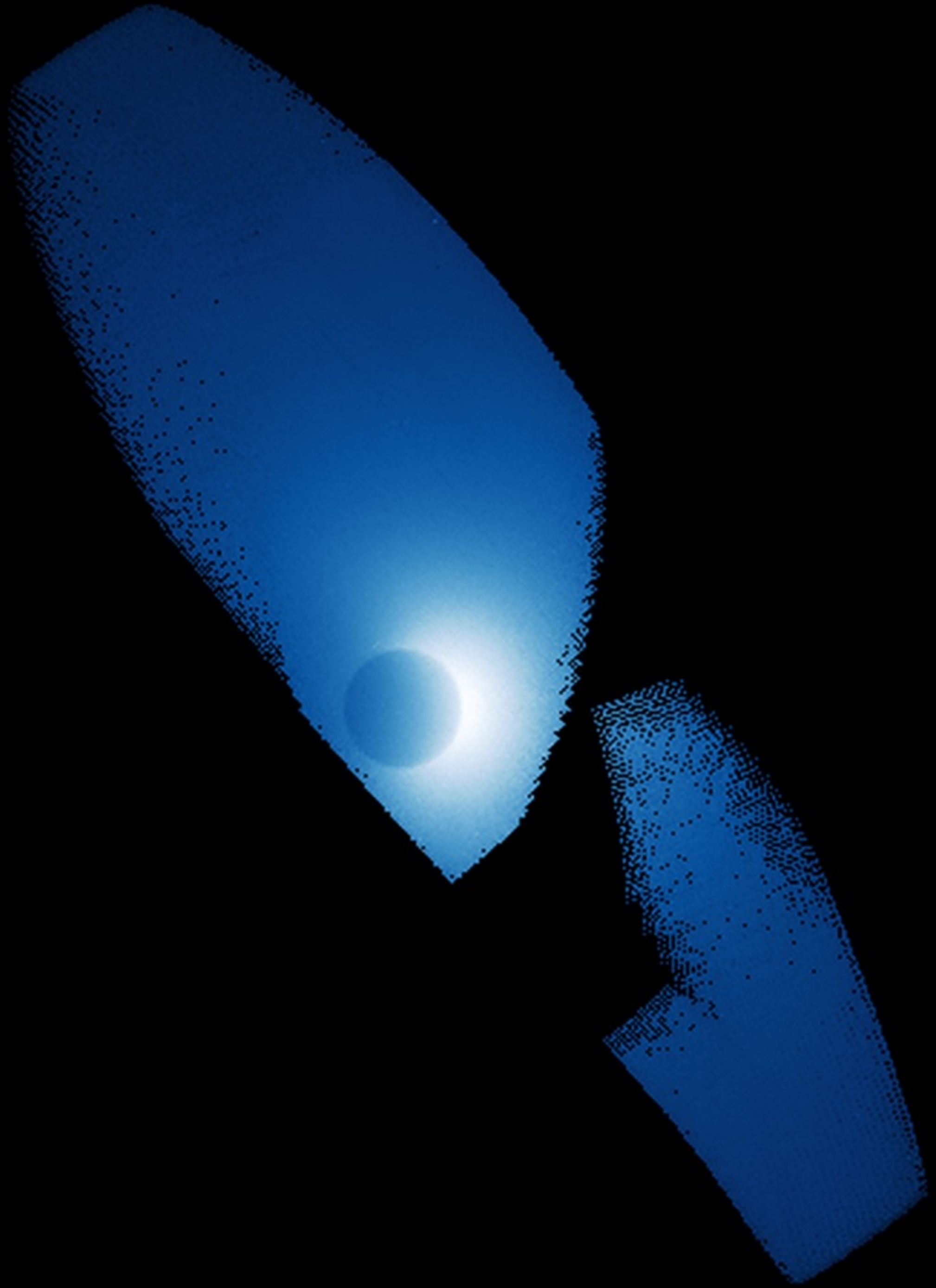

Venus escape

Hydrogen escape

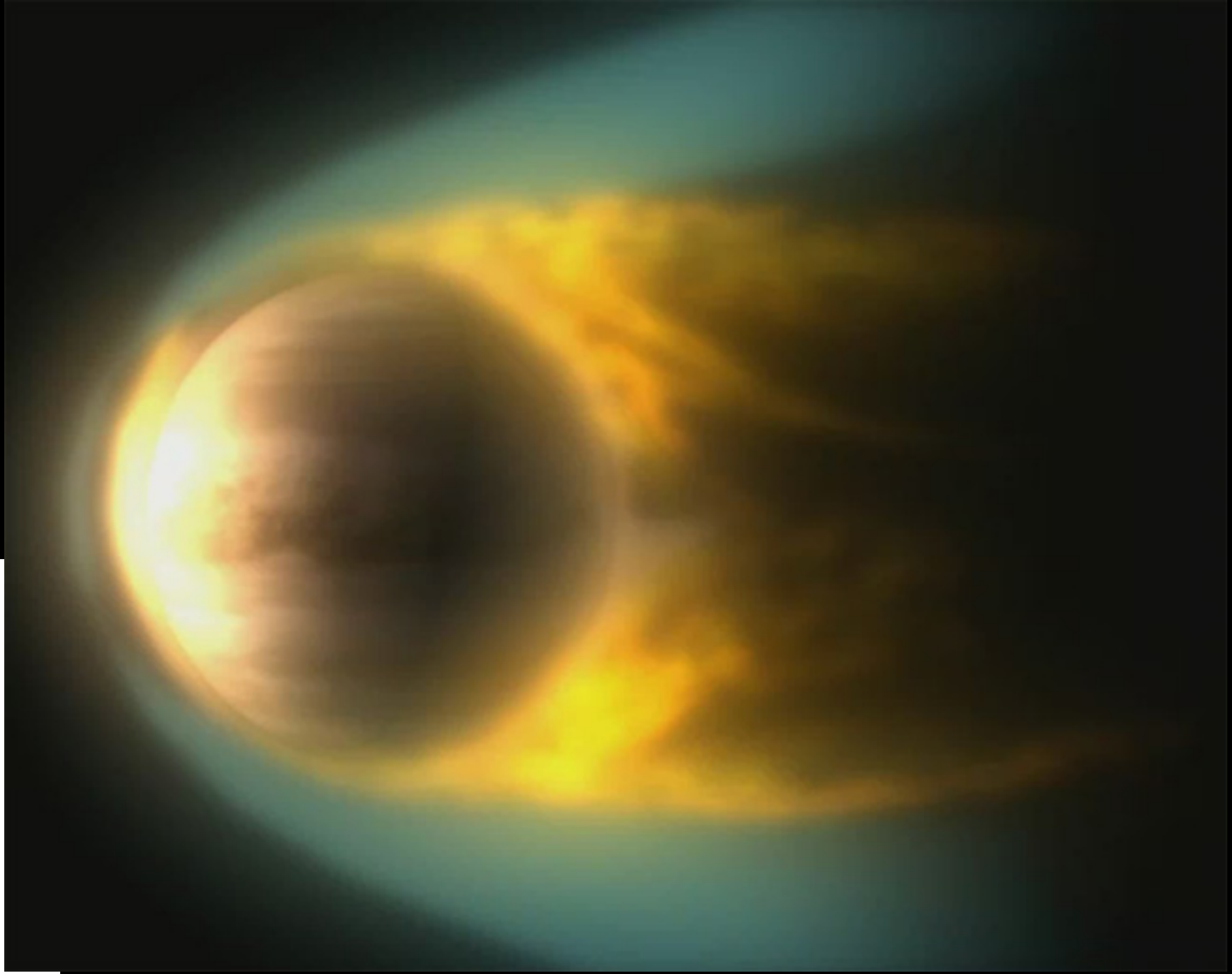

H^+/O^+ Escape Rate Ratio in the Venus Magnetotail and its Dependence on the Solar Cycle

M. Persson[1,2], Y. Futaana[1], A. Fedorov[3], H. Nilsson[1], M. Hamrin[2], and S. Barabash[1]

[1]Swedish Institute for Space Physics, Kiruna, Sweden, [2]Department of Physics, Umeå University, Umeå, Sweden, [3]IRAP, CNRS, Toulouse, France

Abstract A fundamental question for the atmospheric evolution of Venus is *how much water-related material escapes from Venus to space*. In this study, we calculate the nonthermal escape of H^+ and O^+ ions through the Venusian magnetotail and its dependence on the solar cycle. We separate 8 years of data obtained from the ion mass analyzer on Venus Express into solar minimum and maximum. The average escape of H^+ decreased from $7.6 \cdot 10^{24}$ (solar minimum) to $2.1 \cdot 10^{24}\ s^{-1}$ (solar maximum), while a smaller decrease was found for O^+: $2.9 \cdot 10^{24}$ to $2.0 \cdot 10^{24}\ s^{-1}$. As a result, the H^+/O^+ flux ratio decreases from 2.6 to 1.1. This implies that the escape of hydrogen and oxygen could have been below the stoichiometric ratio of water for Venus in its early history under the more active Sun.

3d Intermezzo : on the influence of escape on habitability

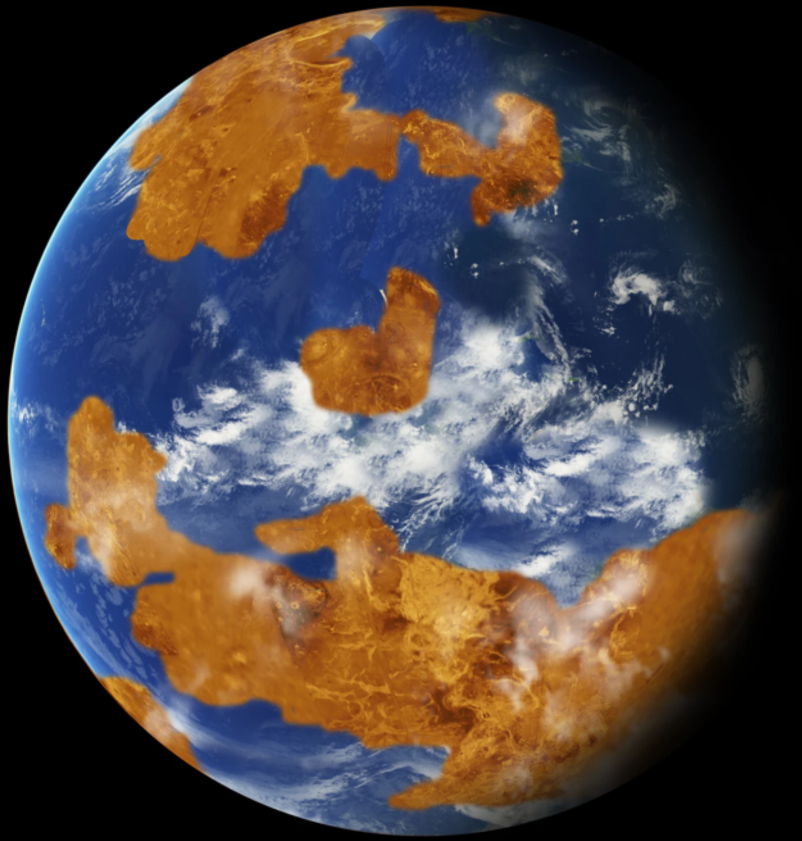

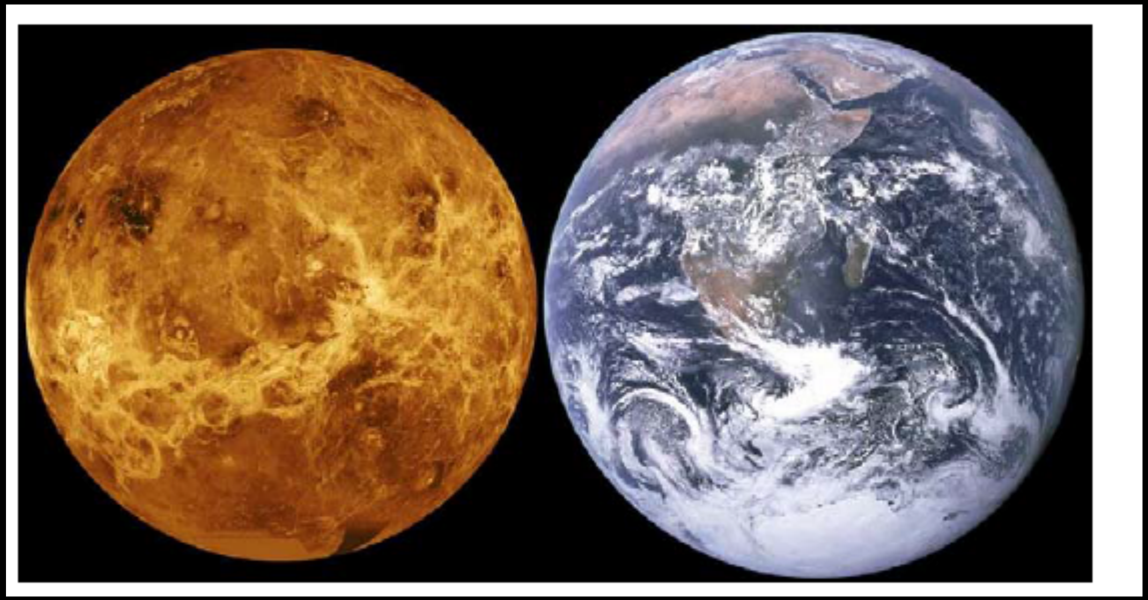

Part 4. Non-LTE mechanisms in planetary atmospheres

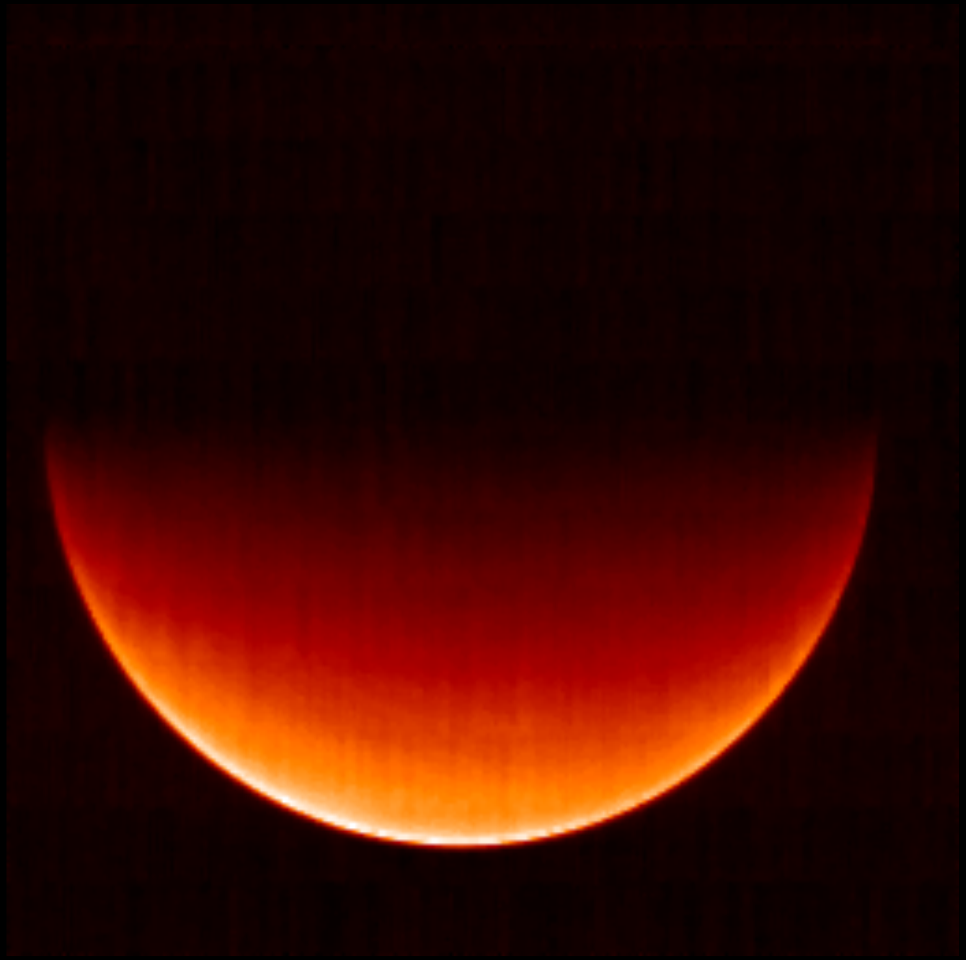

Venus, VIRTIS/Venus Express, 2006
Observation of CO_2 fluorescence at 4.3 µm

- Moreels et al, Experimental Astronomy, 2008

Observations from Observatoire de Haute Provence (1998)

Context of comparative aeronomy of planets

Mesosphere = between stratosphere and thermosphere

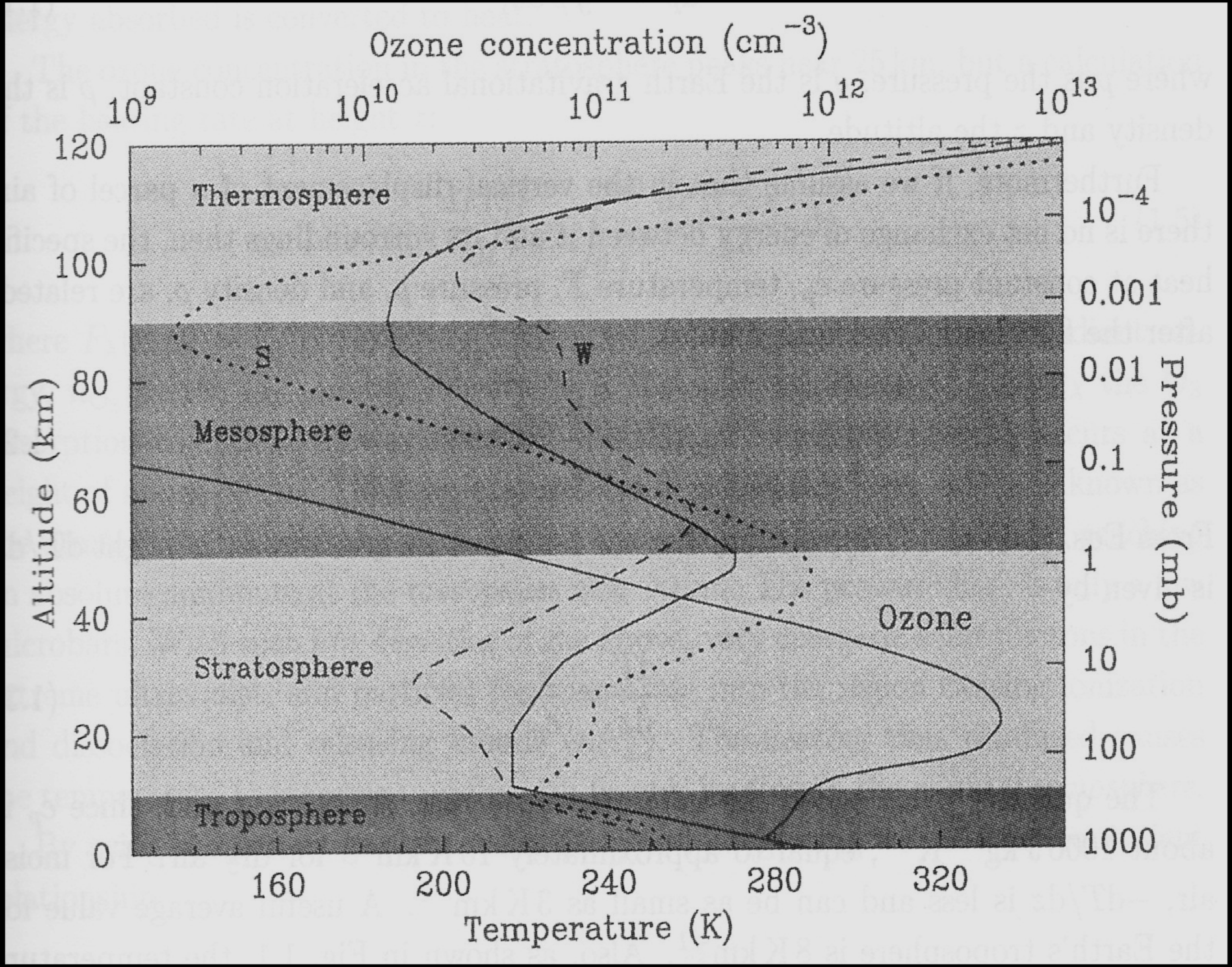

Radiative transfer equation in LTE conditions

Formal radiative transfer equation $dL_\nu(P,s) = - e_\nu n_a [L\nu(P,s) - J\nu(P,s] ds$

L = radiance ; e : extinction coeff. ; n : density of absorber ; J = source term

The complexity is hidden in the source term…

True thermal equilibrium :

$J_\nu = B_\nu$ and $L_\nu = B_\nu$: blackbody condition => 1 temperature T

Local Thermal Equilibrium => $J_\nu = B_\nu$ but $L\nu \neq B\nu$

Observed when thermal collision ensures that all form of energy equilibrate the temperatures (vibrational, rotational, kinetic). Partial LTE possible (rotational vs vibrational, etc.)

Limitations of LTE sounding in infrared emission for dynamical purposes:

- **dependence in limited number of atmospheric parameter (temperature profile T(z))**
- **vertical resolution = weighting function in the RT equation**
- **optical depth τ ~ 1 sounding => limitation to stratospheric levels**

=> Limited dynamical examples : QBO on Earth, QQO on Jupiter/Saturn, expansion of the thermal wave in the SL9 collision with Jupiter

Radiative transfer non-LTE scheme

Non-LTE regime:

$J\nu \neq B\nu$

Thermal collision time > radiative time

Collisional, chemical processes to be taken into account to calculate the source function

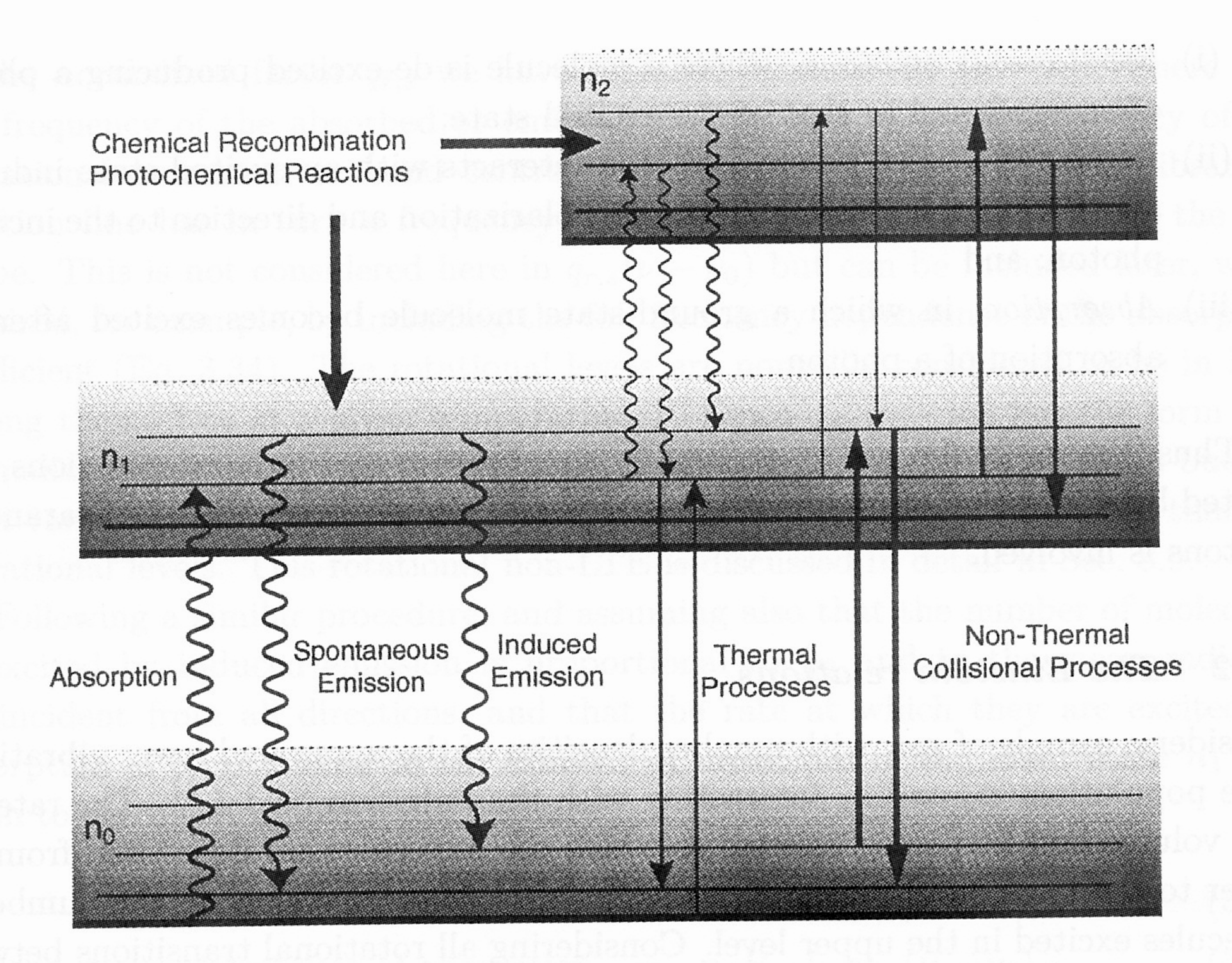

Fig. 3.3 Processes affecting the populations of vibrational levels.

Some non-thermal processes

1. **Vibrational-vibrational energy transfer.**

   Example : CO_2 molecule ; exchange with N_2
2. **Electronic to vibrational energy transfer.**

   Example: $O(^1D)$ state excitating the N_2 vibrational modes
3. **Chemical recombination or chemiluminescence Example: ozone bands at 10 μm**
4. **Photochemical reactions**

   Example : O_2 emissions at 1.27 μm
5. **Dissociative recombination ($O_2^+ + e^- \rightarrow O^* + O$)**
6. **Collisions with charged particles (auroral processes)**

Example : OH emission on Earth

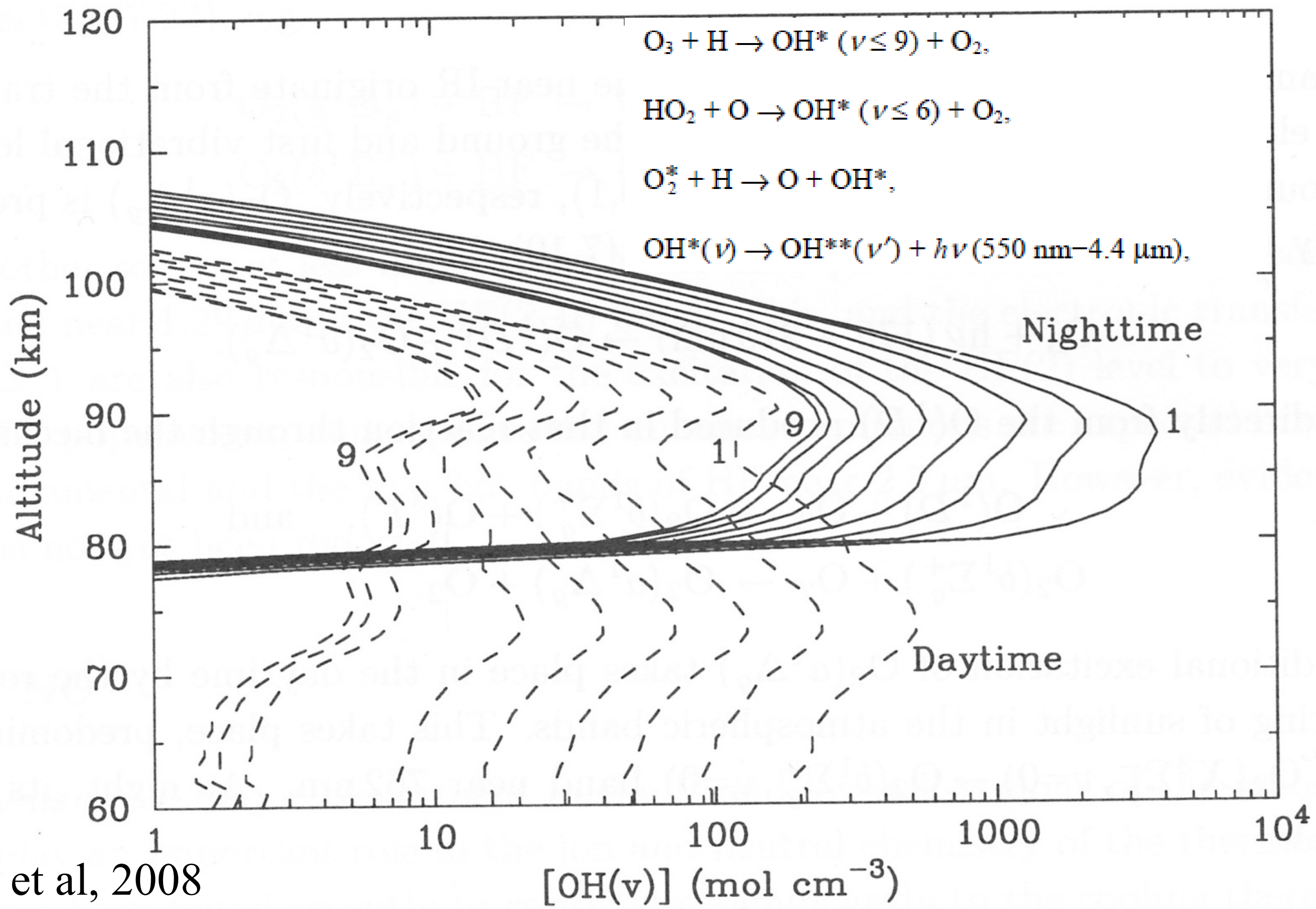

Moreels et al, 2008

Fig. 7.29 Number densities of the vibrationally excited $v = 1$–9 (right to left) hydroxyl radical for night-time (solid) and daytime (dash) conditions. After López-Moreno *et al.* (1987).

OH emission from the ground

- Moreels et al, Experimental Astronomy, 2008

Observations from Observatoire de Haute Provence (1998)

OH emissions are modulated by dynamical processes through density / temperature variations, in particular Gravity waves

Earth O(1D) emission (630 nm) modulated with GW

$O(^1D)$ emission

$O_2 + O^+ \rightarrow O_2^+ + O$

$O_2^+ + e^- \rightarrow O_2 + O(^1D, \ldots)$

$O(^1D) \rightarrow O(^3S) + h\nu$

Emission around 630 nm is modulated by dynamical processes (density / temperature variations)

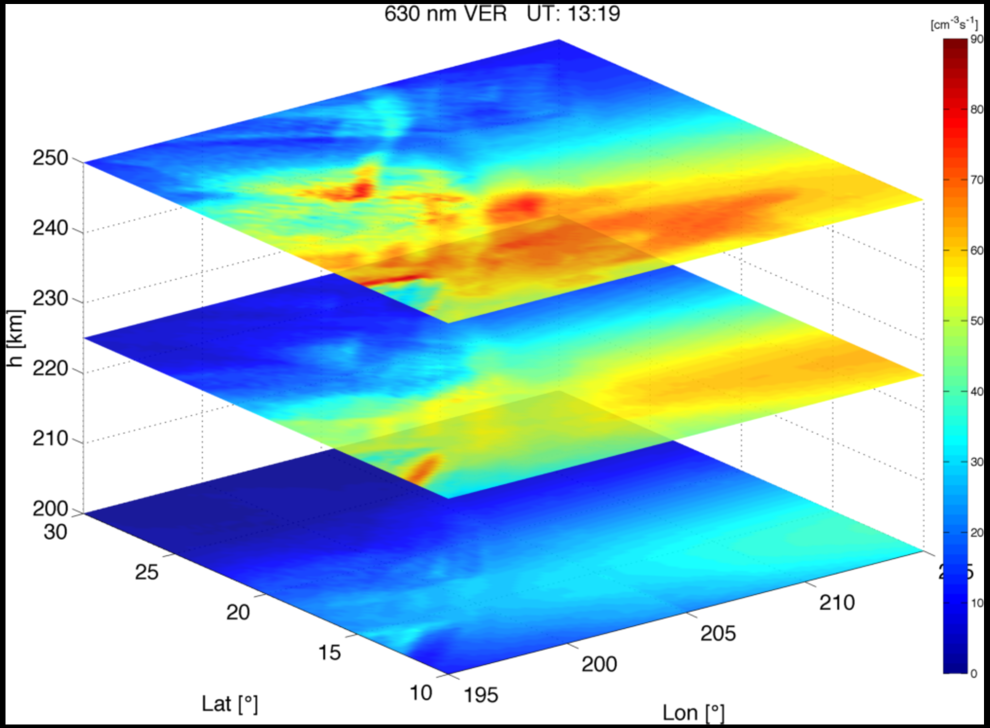

Model by P. Coisson (PhD Thesis, 2012

Tohoku tsunami observation of forced GW travelling above Hawaii

Total vertical Luminescence
verticale totale between 1 et 1.7
mHz : evidence of gravity waves
forced by the tsunami (blue line).
Occhipinti et al, 2012.

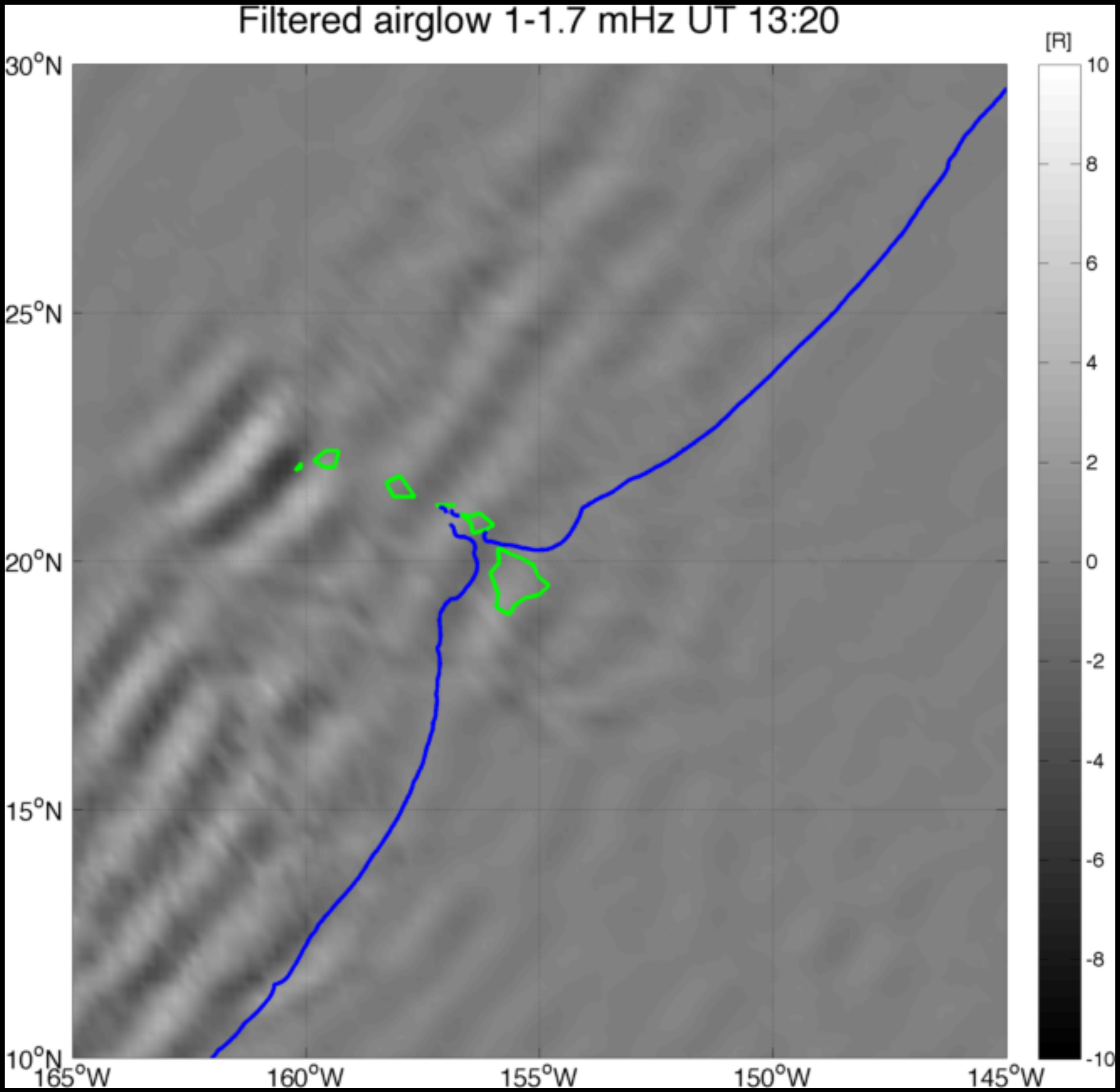

OH and O_2 emission on Venus

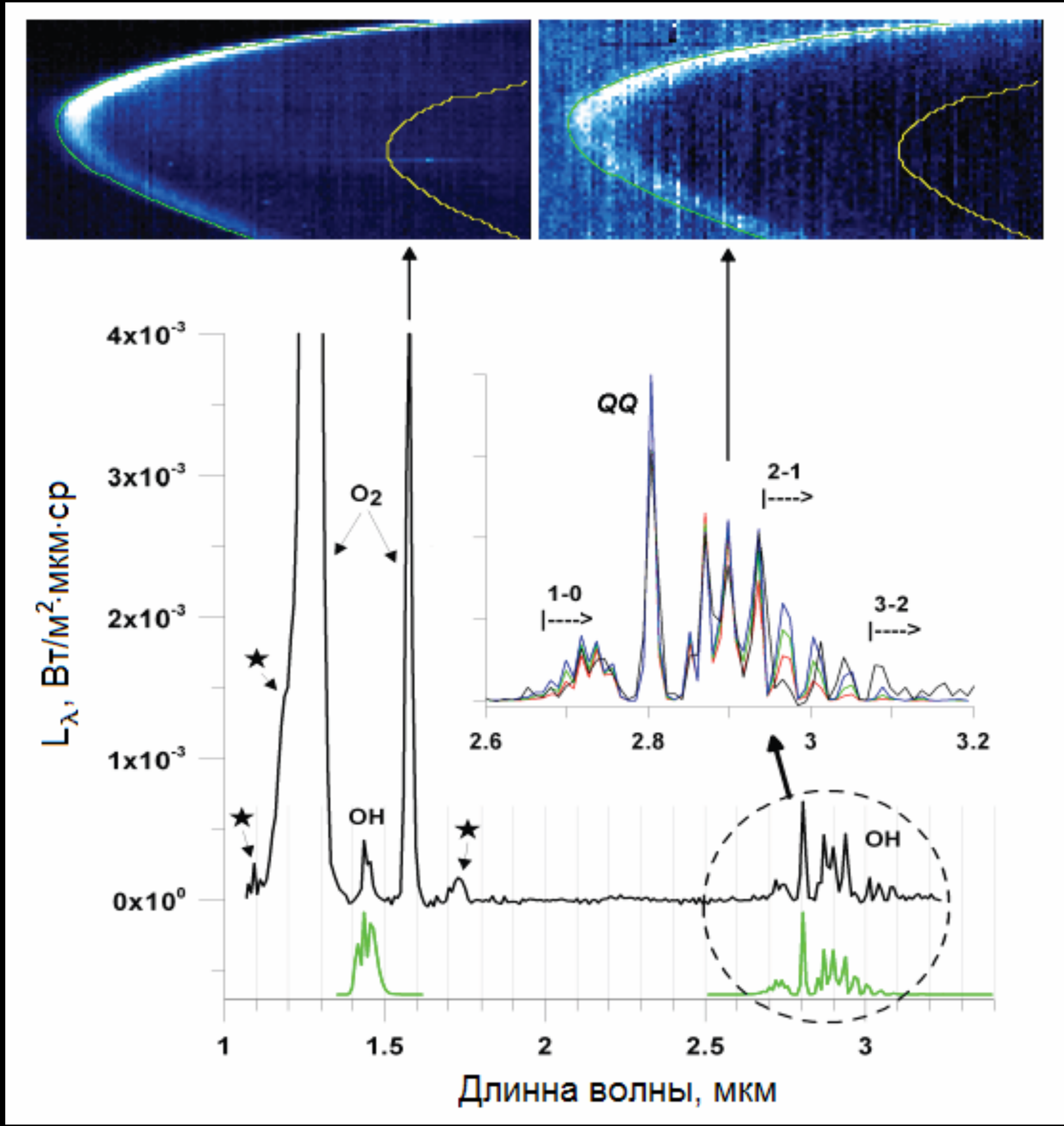

OH altitude emission
~ 95 km as O_2
cf Piccioni et al 2009

A.V. Shakun, PhD Thesis 2012

A conceptual picture of O_2 (Δ) production and airglow on Venus

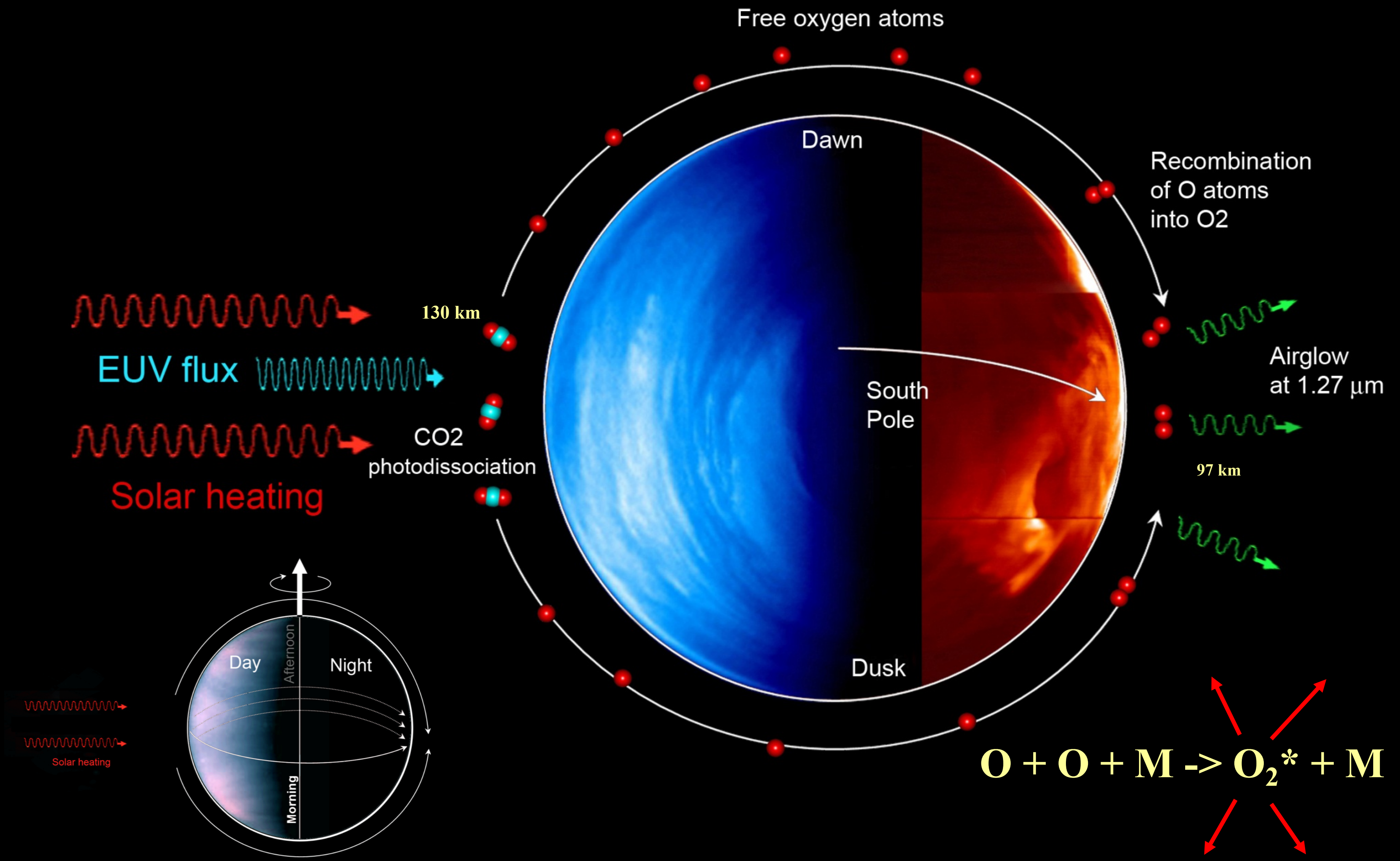

$$O + O + M \rightarrow O_2^* + M$$

O_2 average emission (L. Soret and JC. Gérard, Liège)

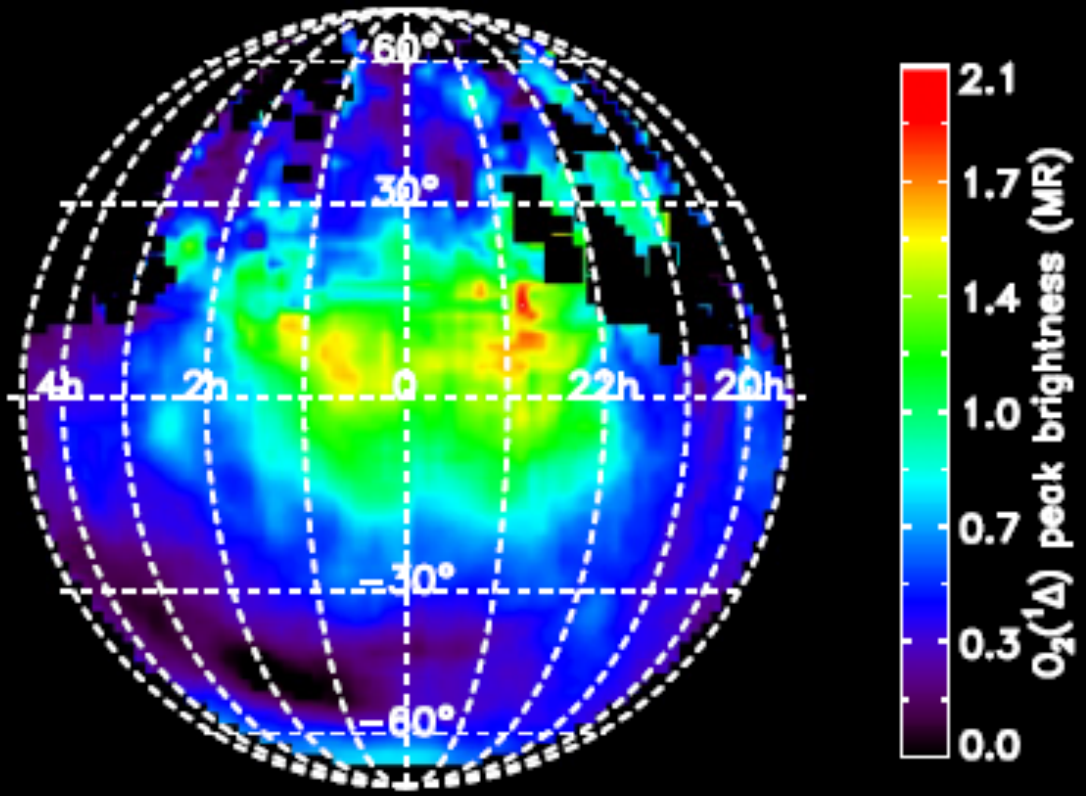

O_2 emission altitude : ~95 km

Mean nadir intensity = 0.50 MR

Latitudinal – local time distribution of the O_2 infrared atmospheric band in the Venus lower thermosphere - Soret et al. (2012)

Comparative planetology: atmosphere of the terrestrial planets

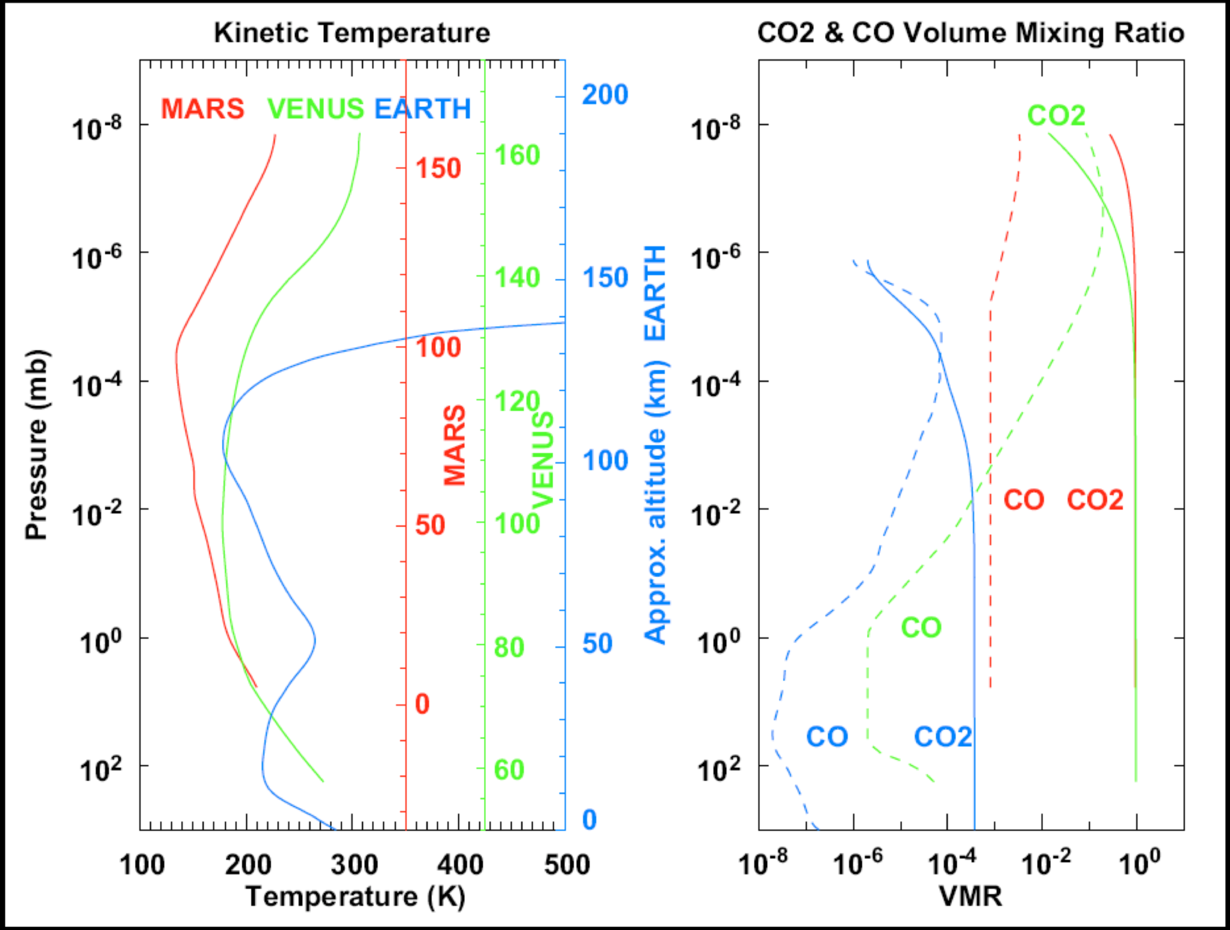

SIMILARITIES

- UV, soft X-rays absorption in the Thermosphere
- IR absorption in the mesosphere

DIFFERENCES

- Venus and Mars thermosphere colder than on the Earth
- O, CO about 10 times more abundant on Venus and Mars
- Stronger cooling in the upper regions of Mars and Venus by the CO_2 15-µm vibrational excited levels
- CO_2 vmr on the Earth is 1000 time smaller

Vibration-rotation spectrum of CO_2

Vibration rotation bands

of CO_2 in the infrared

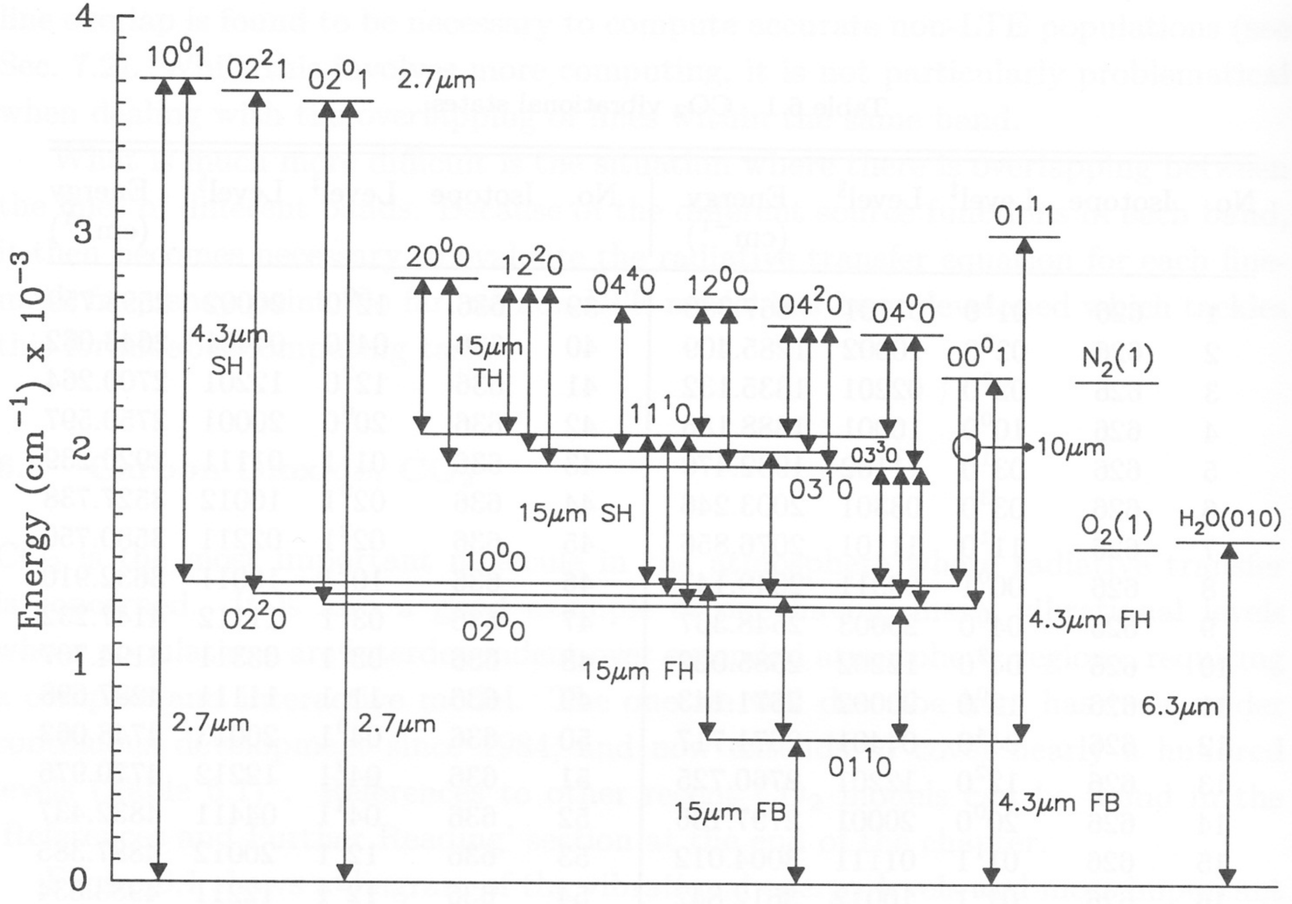

Fig. 6.1 Vibrational levels (with energy lower than 2.7 µm) and transitions for the CO_2 major isotope, and for the first vibrational levels of N_2, O_2, and H_2O.

Basics on non-LTE models for Venus, Mars and the Earth : CO_2

CO_2 4.3 μm levels scheme

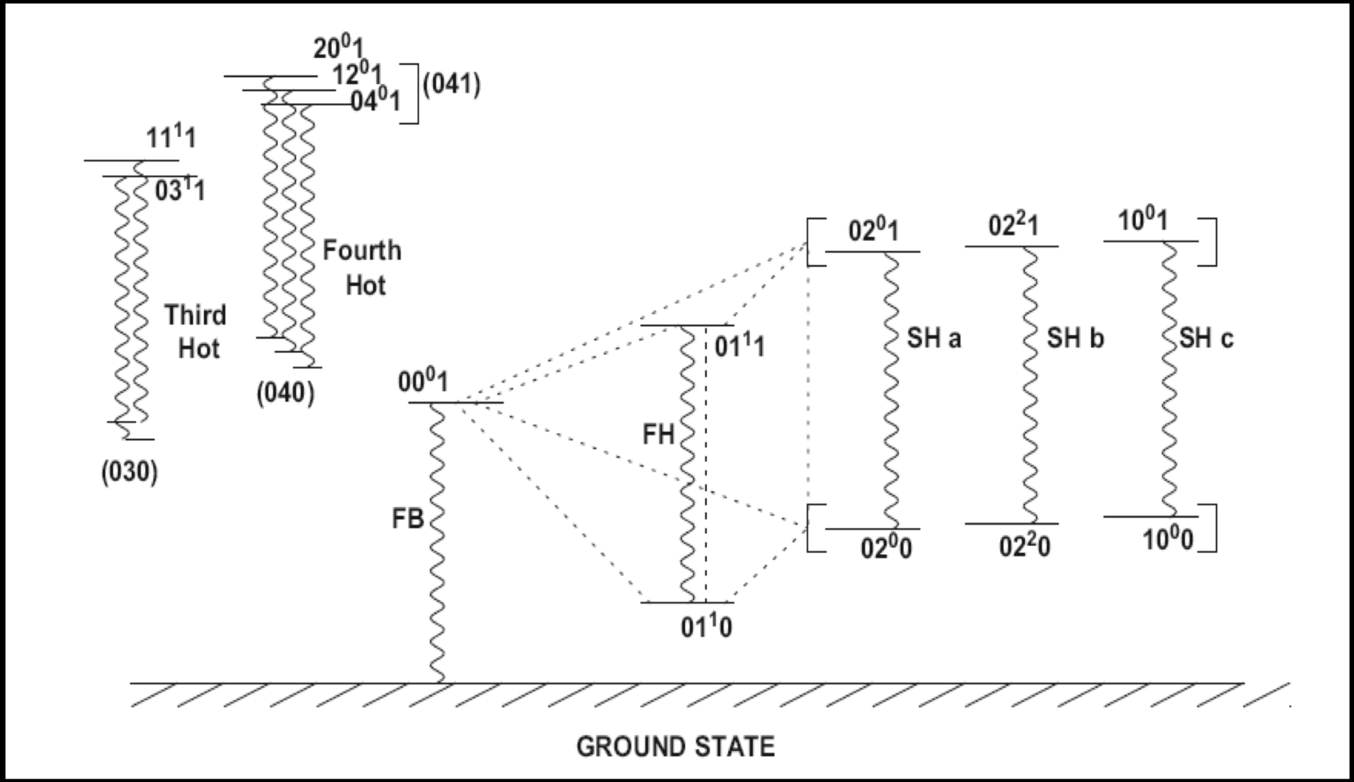

CO_2 high energy states directly excited during daytime by solar absorption.

- FB band: Transition from 001 level to the ground
- FH, SH bands: arises from higher energy states

Venus non LTE Emissions of CO_2 at 4.3 mm

Altitude of emission : 60-150 km

Limb brightnening due to CO_2 fluorescence

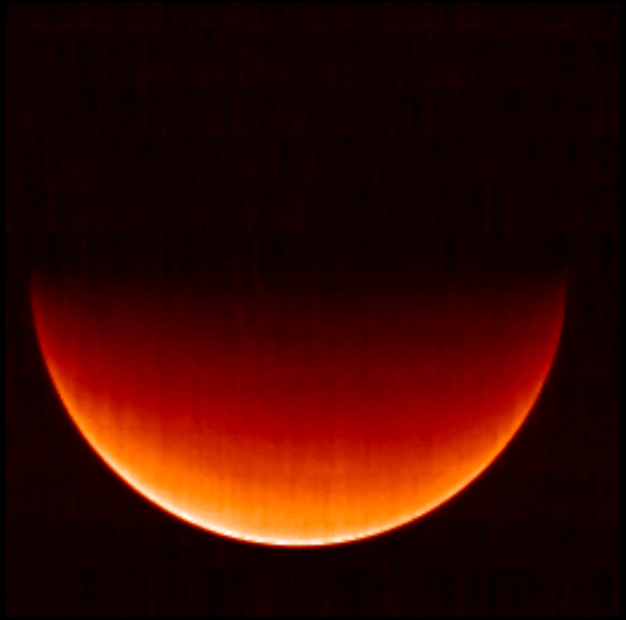

Venus Express/VIRTIS
Observations 2006

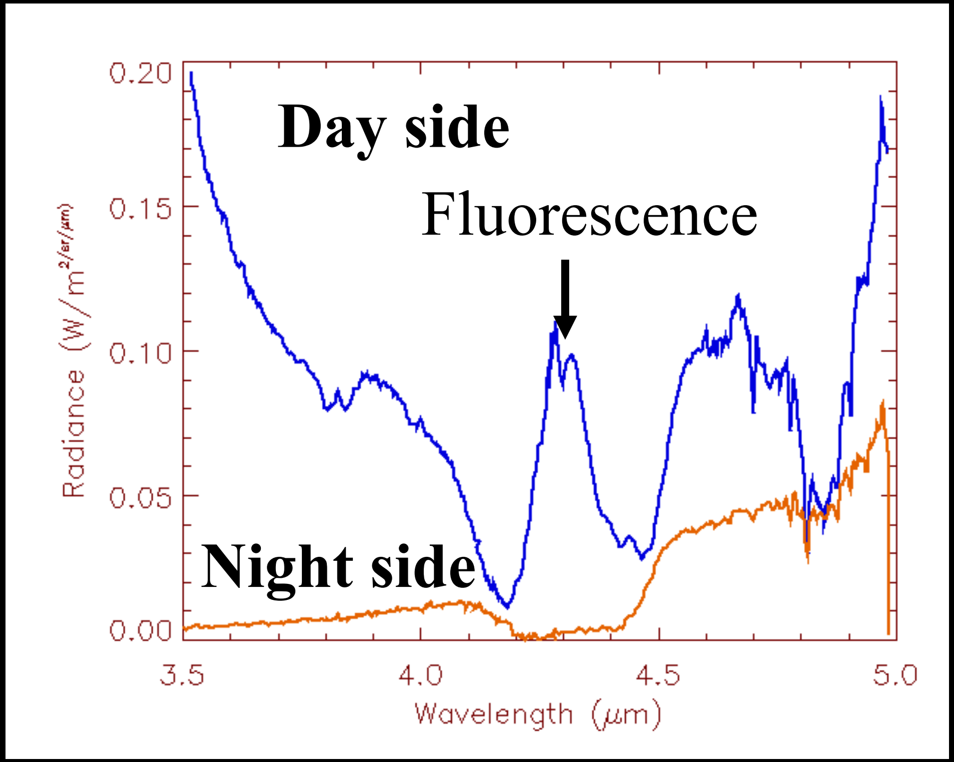

Basics on non-LTE models for Venus, Mars and the Earth

CO_2 4.3 μm Vibrational temperatures

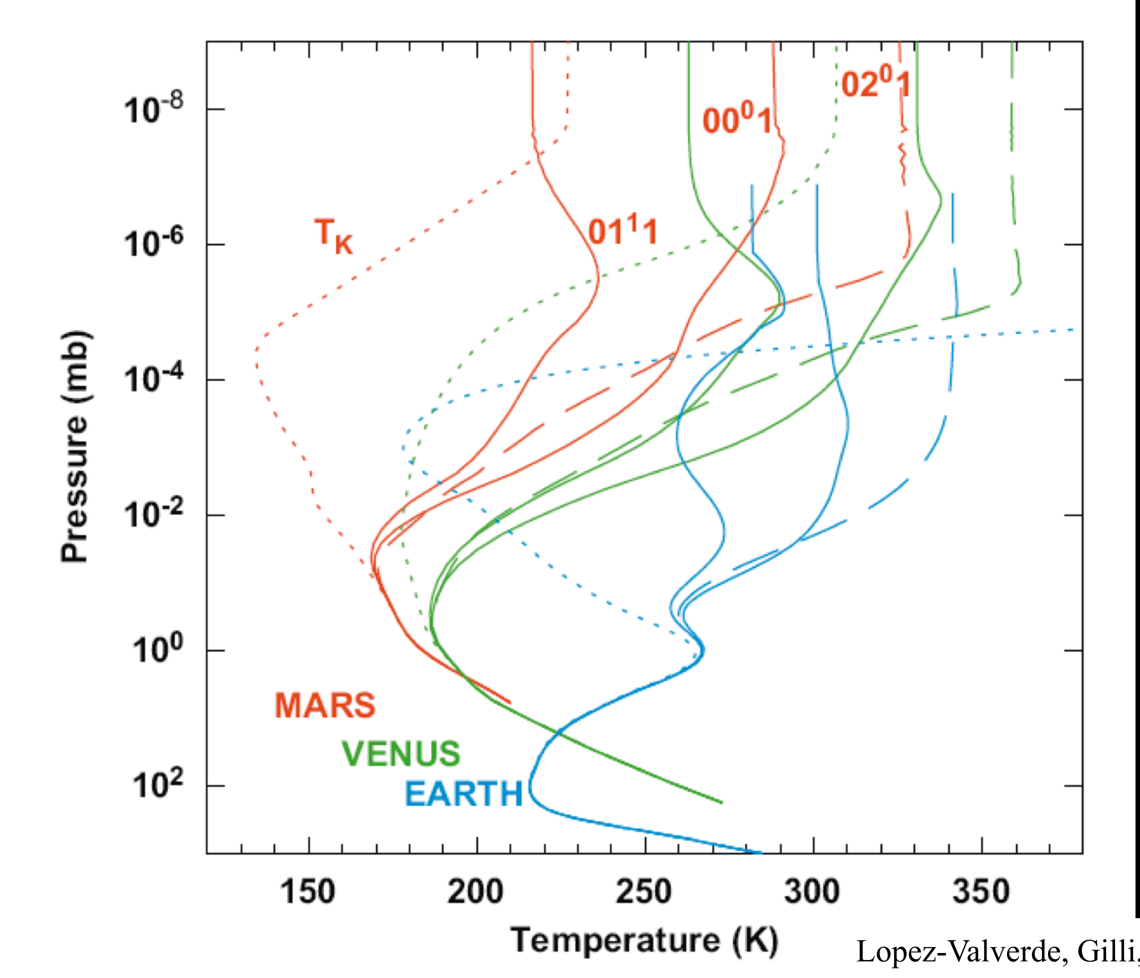

Lopez-Valverde, Gilli,… PSS, 2011

- LTE departure at similar pressure levels for Mars and Venus, lower pressure on Earth
- Vibrational temperatures constant at the top of the atmosphere

CO_2 non-LTE limb observations for Earth, Mars and Venus with VIRTIS

Earth : 66/76/90/100 km
Mars : 73/110/149/188 km
Venus : 98/107/116/126 km
Pressure levels of CO_2 : 10^{-3} to 10^{-9} mbar

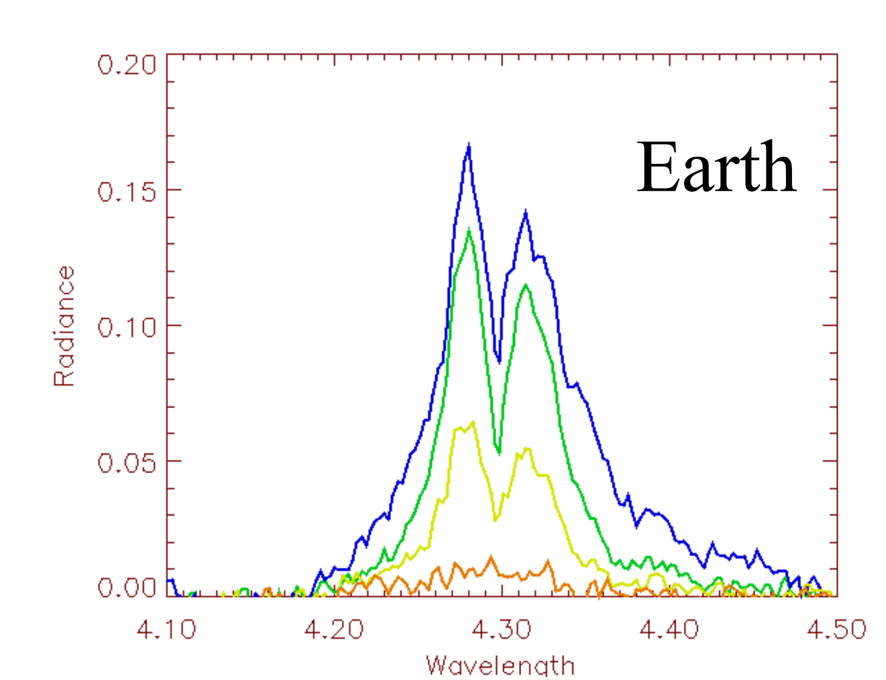

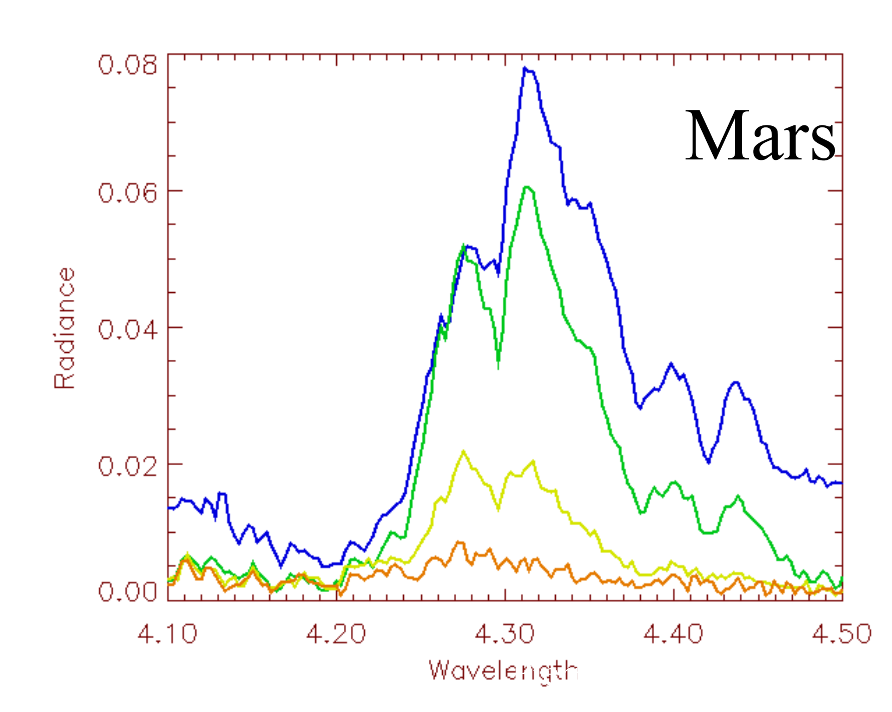

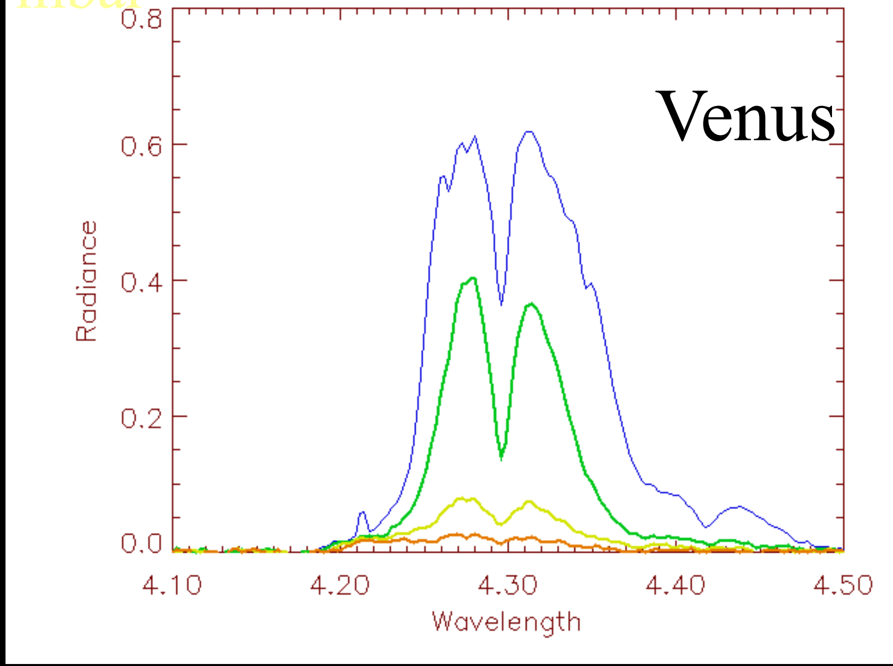

VENUS VIRTIS observations for CO_2 non-LTE

Gilli et al, JGR 2009

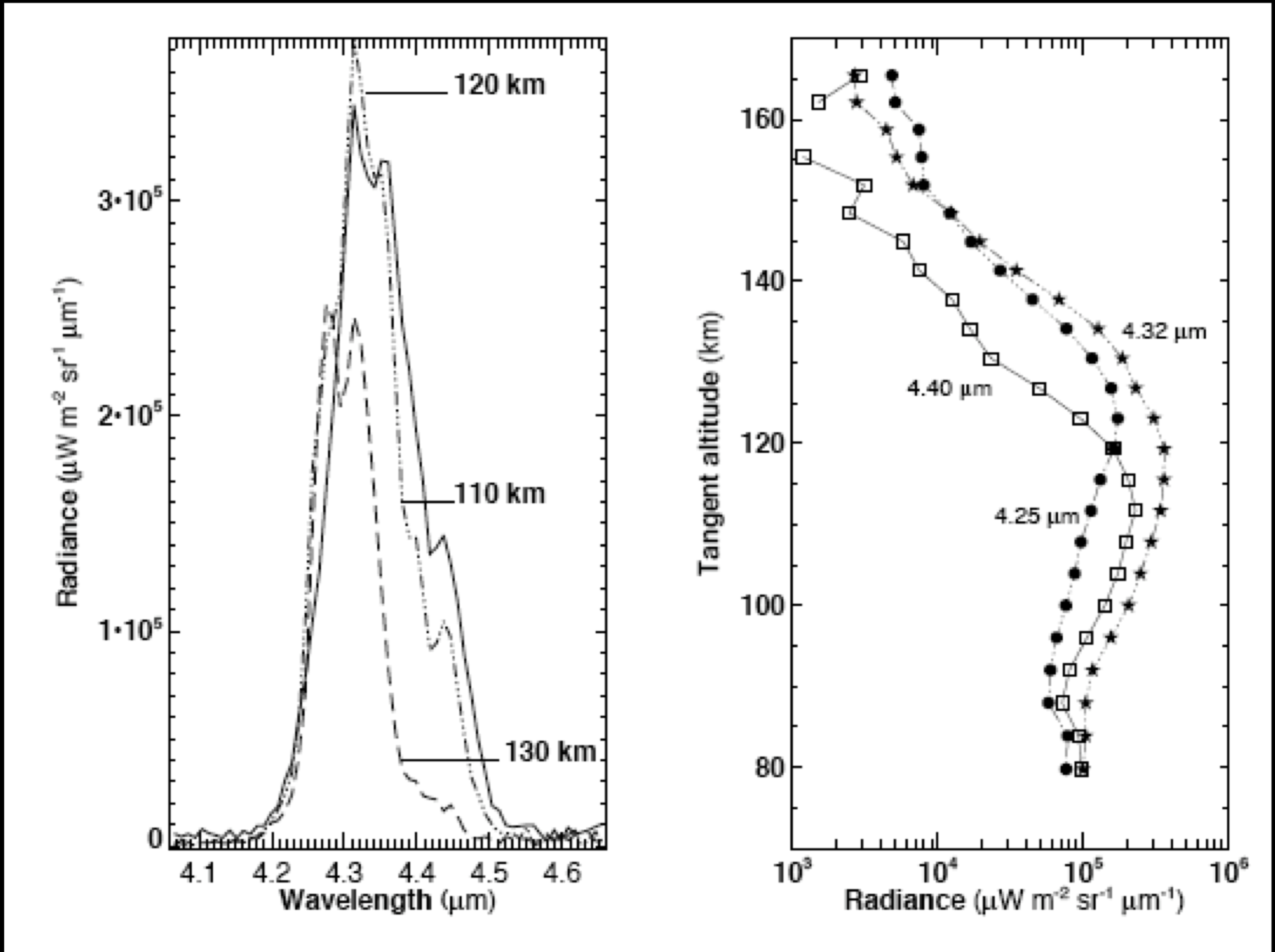

Giant Planets :

Cassini/VIMS CH_4 emissions at 3.3 μm

Jupiter (2000)

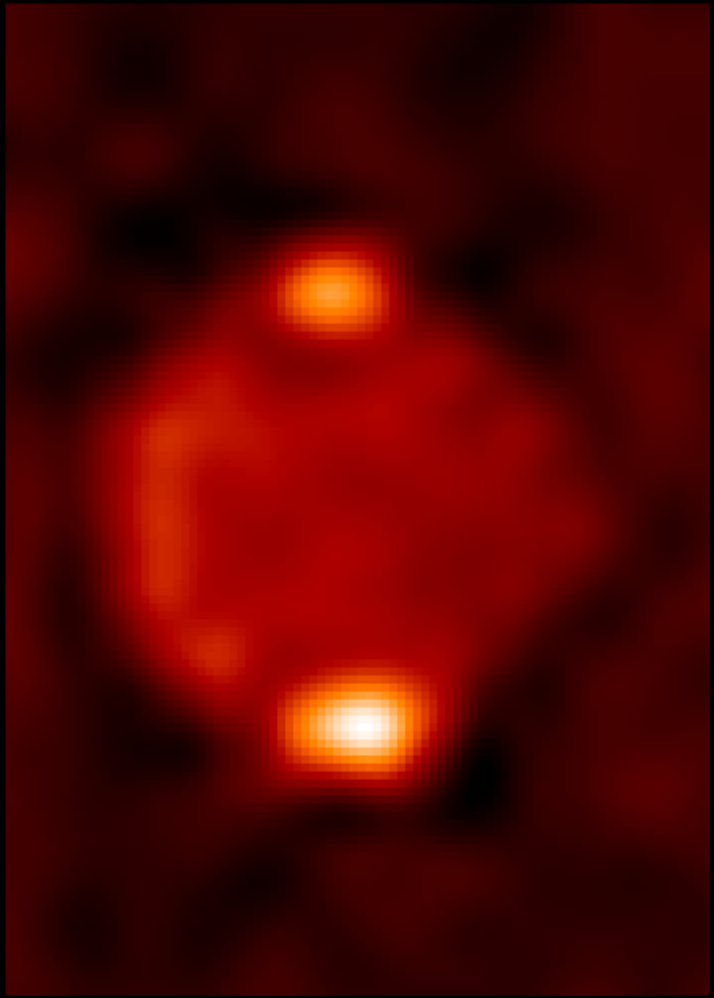

Saturn (2005)

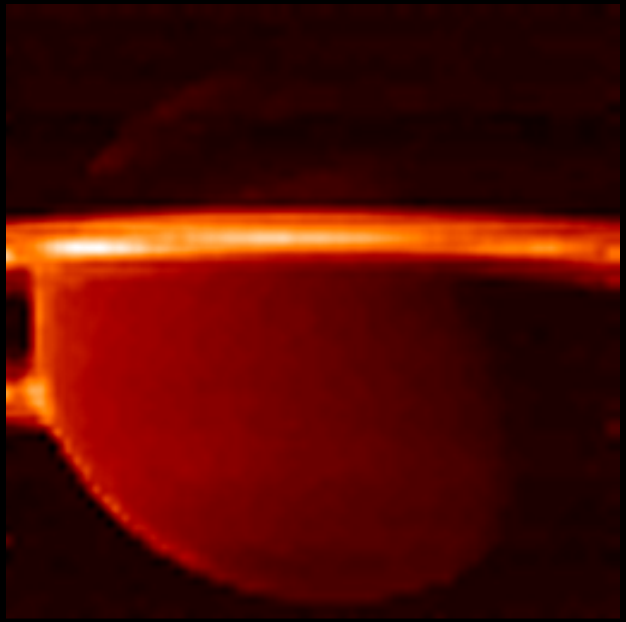

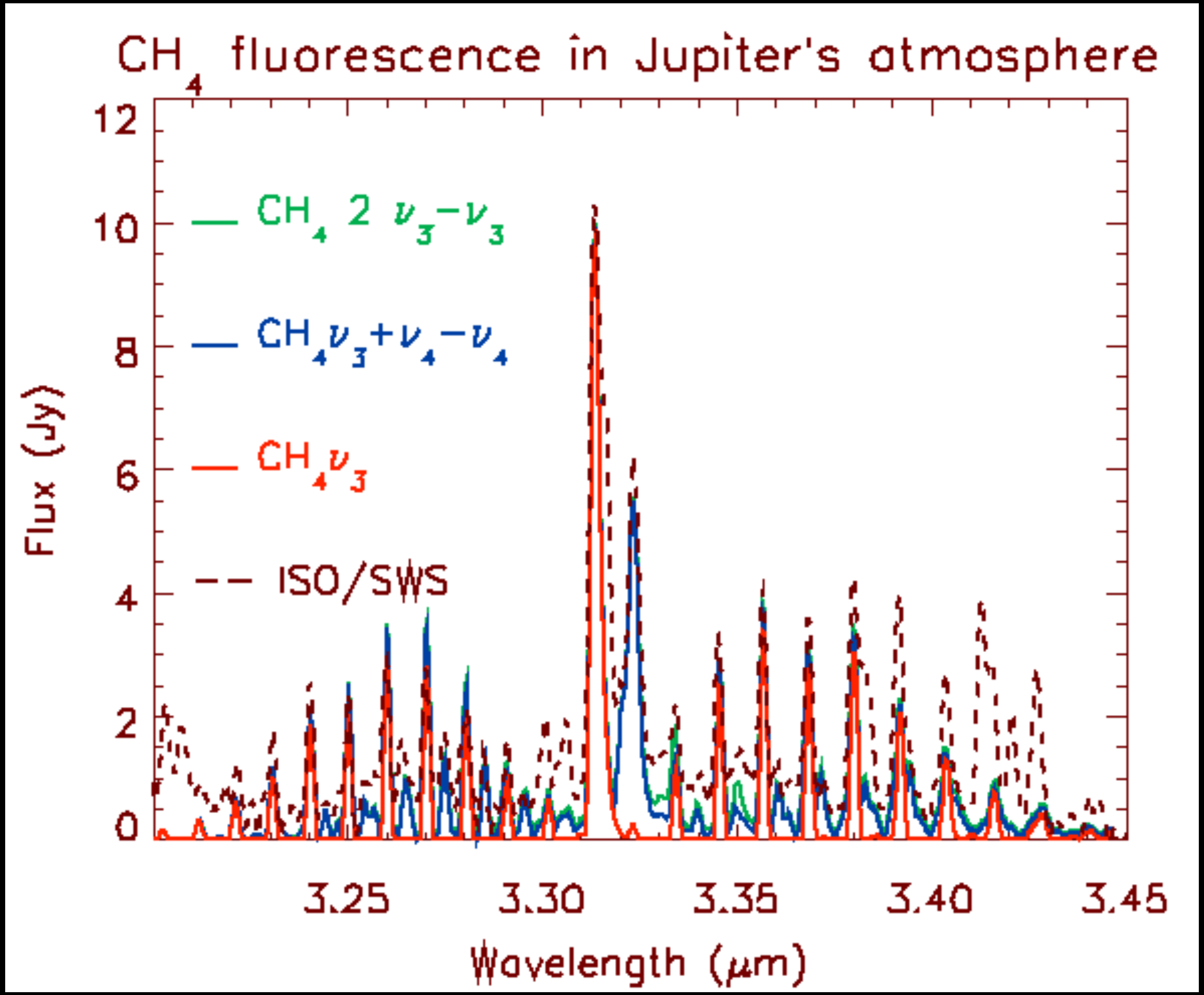

Drossart et al, ESA-SP 427, 1999

Comparison of synthetic spectra with ISO/SWS observations

vibration/rotation bands: CH_4

7.8 µm 3.3 µm 2.3 µm 1.8 µm

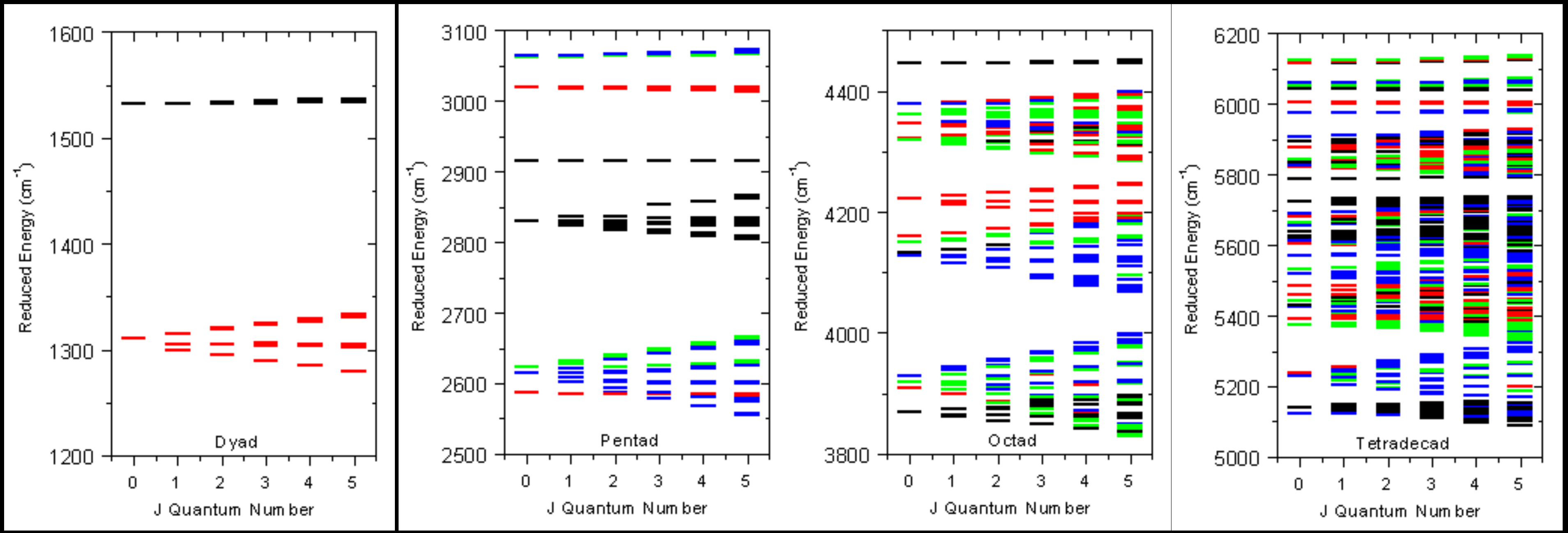

Dyad	Pentad	Octad	Tetradecad
2 vibrational states	5 vibrational states	8 vibrational states	14 vibrational states
2 sublevels	9 sublevels	20 sublevels	60 sublevels

Wenger and Champion, JQSRT, 1998

Simplified scheme of fluorescence in CH_4 in planetary atmospheres

- grouping stretching/ bending levels of CH_4
- CH_4 radiative transitions:
- ν_4 (7.8µm) ν_3 (3.3µm)

$\nu_3 + \nu_4$ (2.3µm) $\nu_3 + 2\nu_4$ (1.7µm)

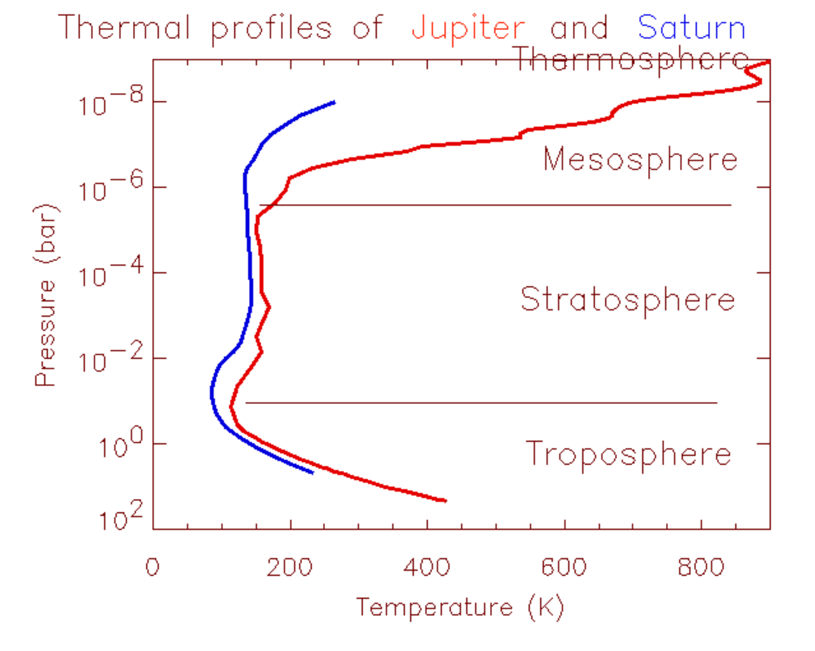

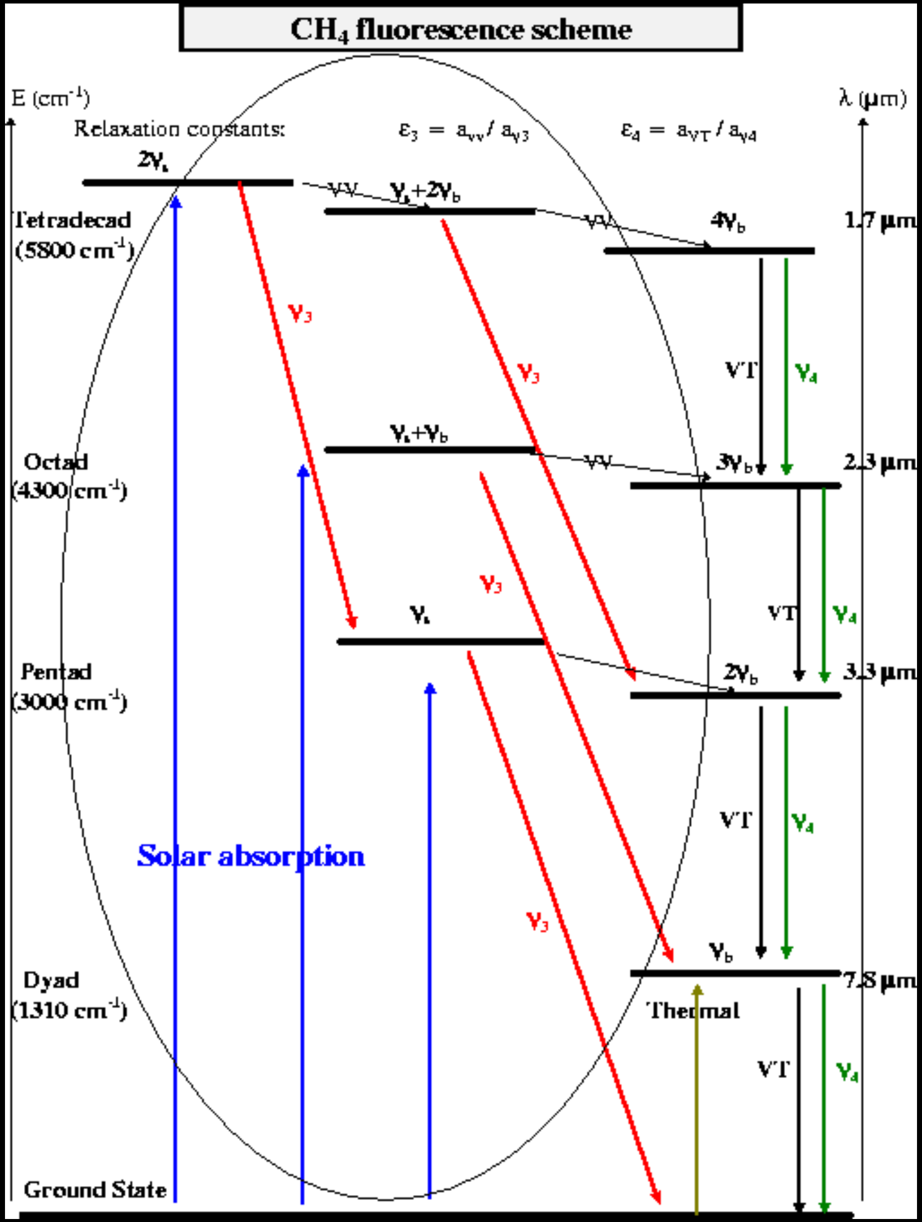

Jupiter infrared observations (VLT/ISAAC)

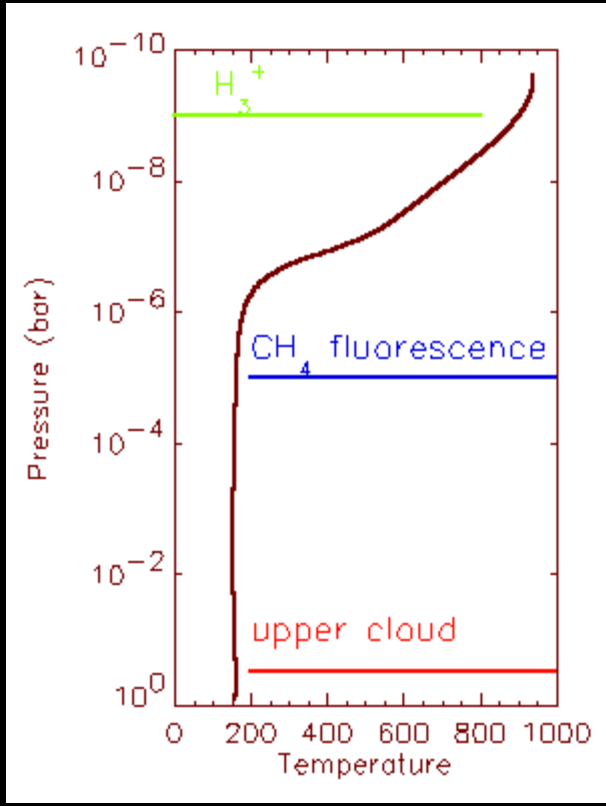

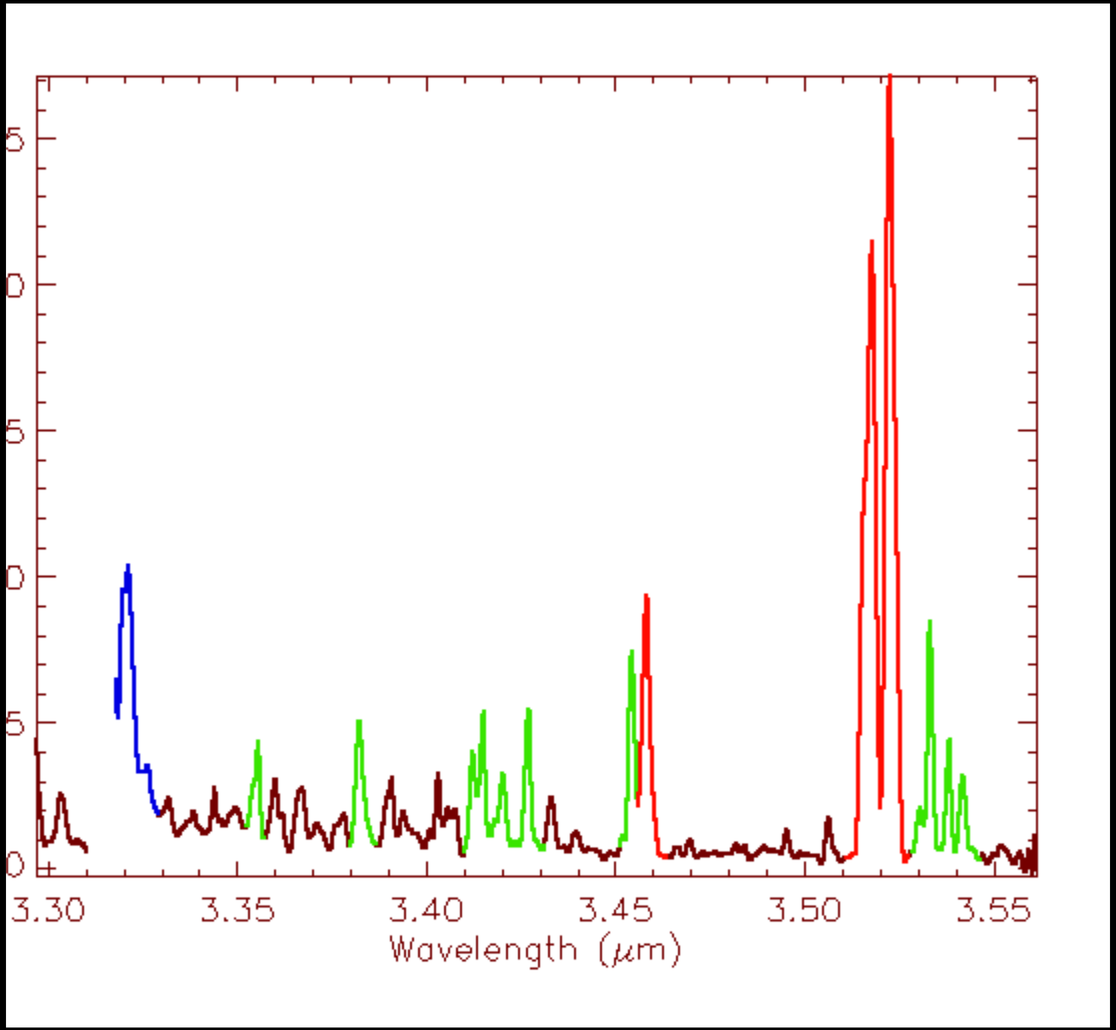

Jupiter : CH_4 fluorescence map

H_3^+ contamination in the auroral zone => measurements limited to l< 60°

CH_4 flux variation: variation ≈ noise $\Delta CH_4 < 20\%$

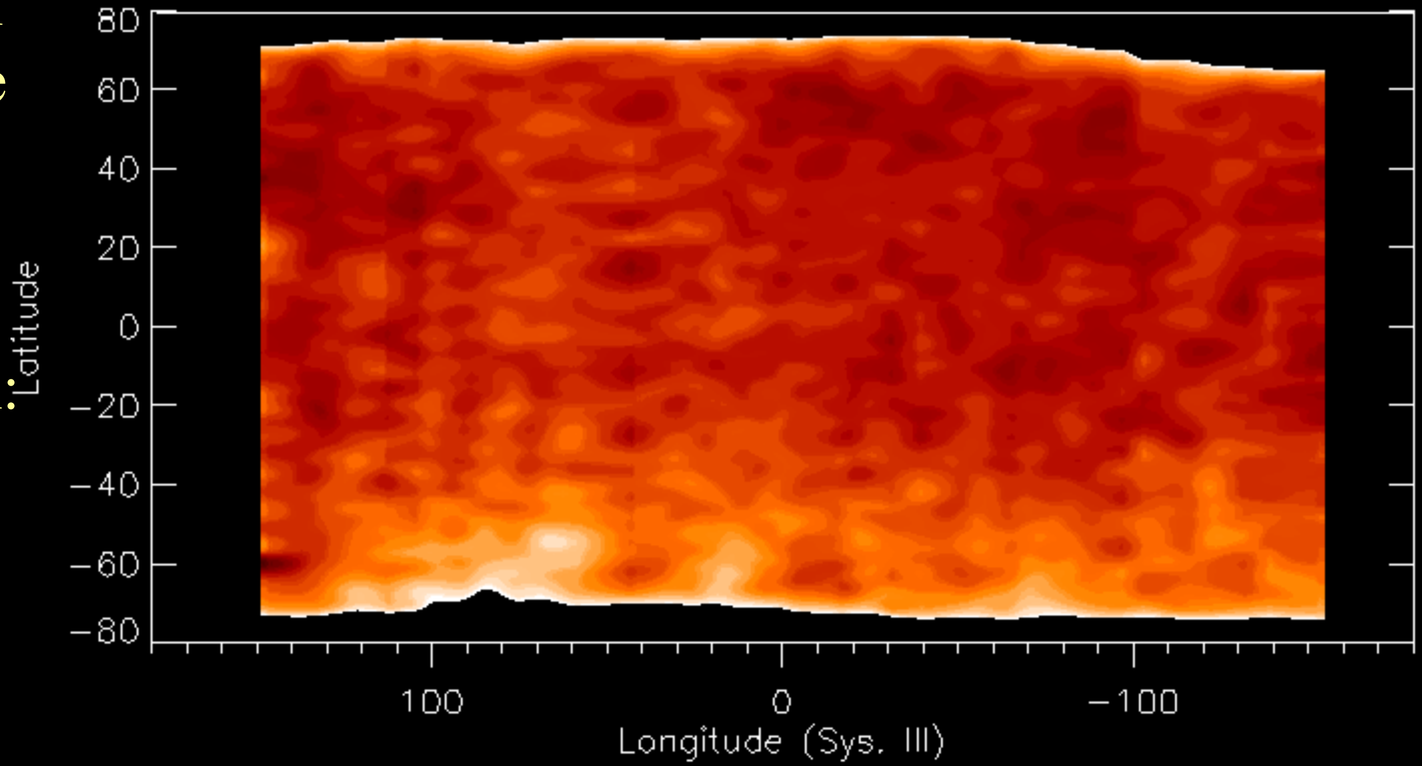

Jupiter : H_3^+ map at mid latitudes

H_3^+ variations detected at ±10% level <=> $\Delta T = \pm 30K$

•large scale: hemispheric asymmetry

•small scale: Wave activity?

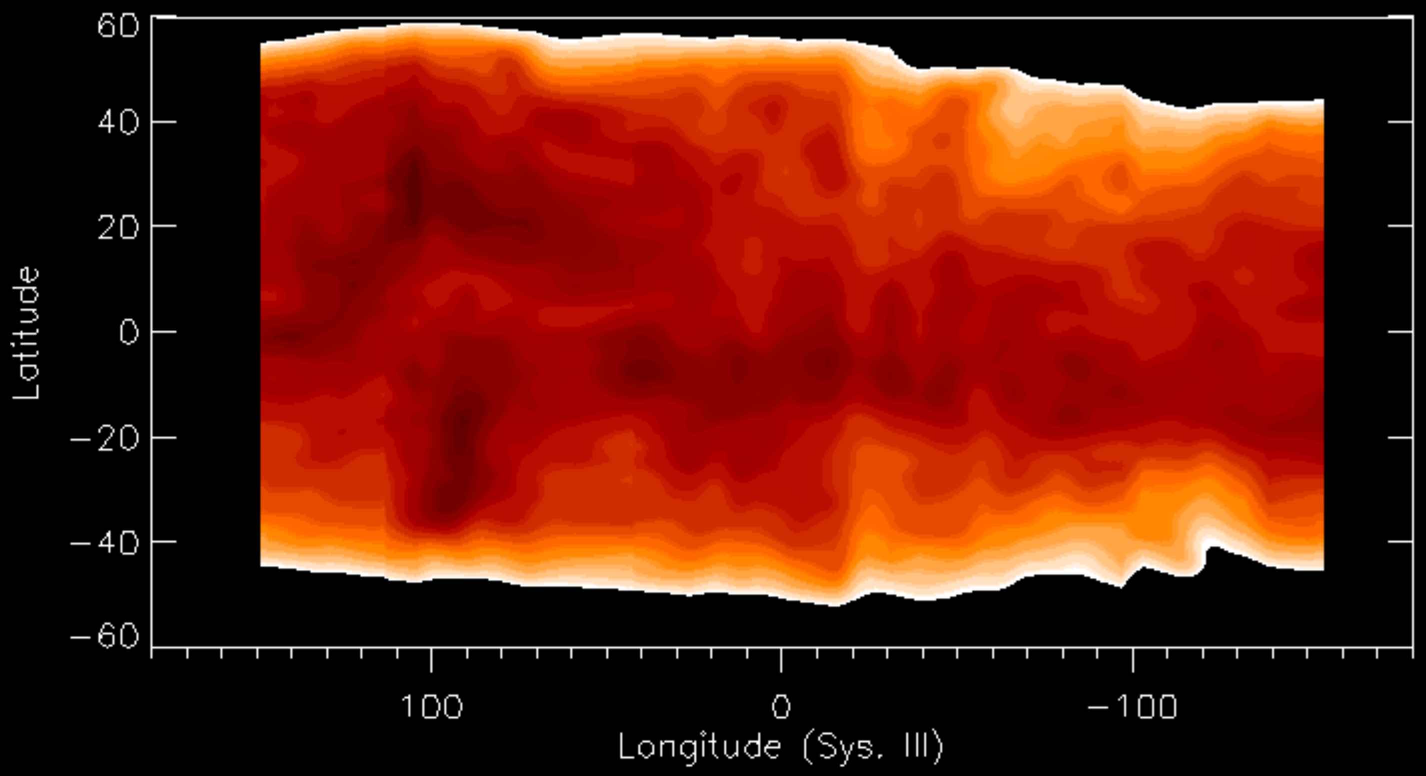

Model for Atmospheric Gravity Waves Signatures in Jupiter's H_3^+(Barstow, Matcheva, Drossart, 2012)

AGW

Neutral Atmosphere

$$T', \rho', p', \vec{U}'_n$$

Ion Dynamics

$$\vec{U}'_i = \left(\vec{U}'_n \cdot \hat{\imath}_B\right)\hat{\imath}_B$$

Ion Chemistry

$$H_2^+ + H_2 \rightarrow H_3^+ + H$$

$$H_3^+ + e^- \rightarrow \begin{cases} H_2 + H \\ 3H \end{cases}$$

$$H_3^+ + CH_4 \rightarrow CH_5^+ + H_2$$

H_3^+ temperature

H_3^+ density

H_3^+ emission

$$\frac{\partial N'_i}{\partial t} + \nabla \cdot \left(N'_i \vec{U}_{i0} + N_{i0}\vec{U}'_i\right) = P' - \left(L'_1 + L'_2\right)$$

Gravity wave on Jupiter : Theoretical Results

Model = Galileo Wave 2:

l_z=147 km l_h=710 km

DT_{max}=41 K Z_{max}=710 km

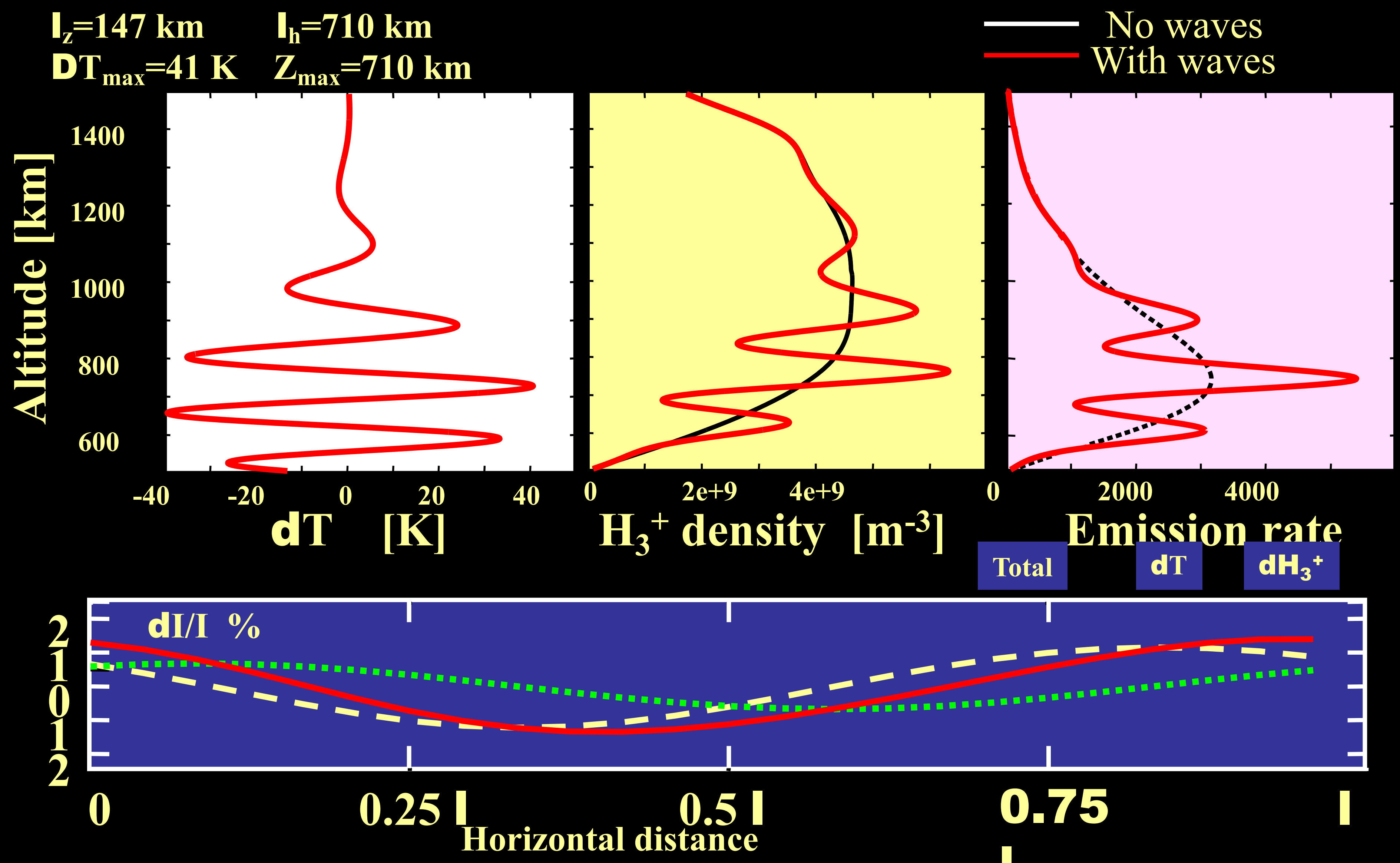

Wave induced variation of the intensity, I, of the H_3^+ emission

Fluorescence scheme

CH_4 vibrational modes : stretching (ν_1 , ν_3) / **bending** (ν_2 , ν_4) **modes with $s \sim 2\,b$**

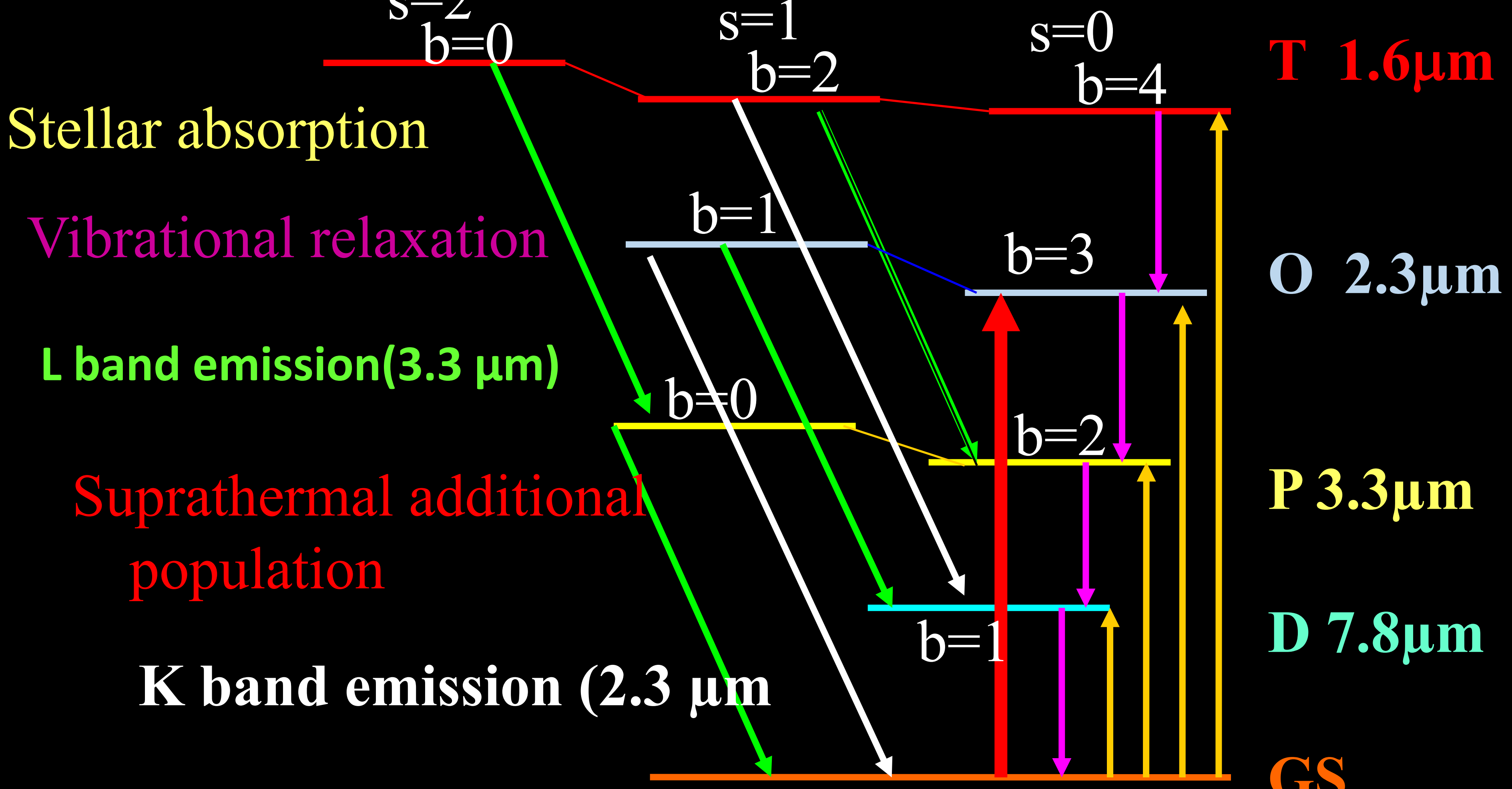

Fit of HD 189733b in L band

Waldmann et al., ApJ, 2012

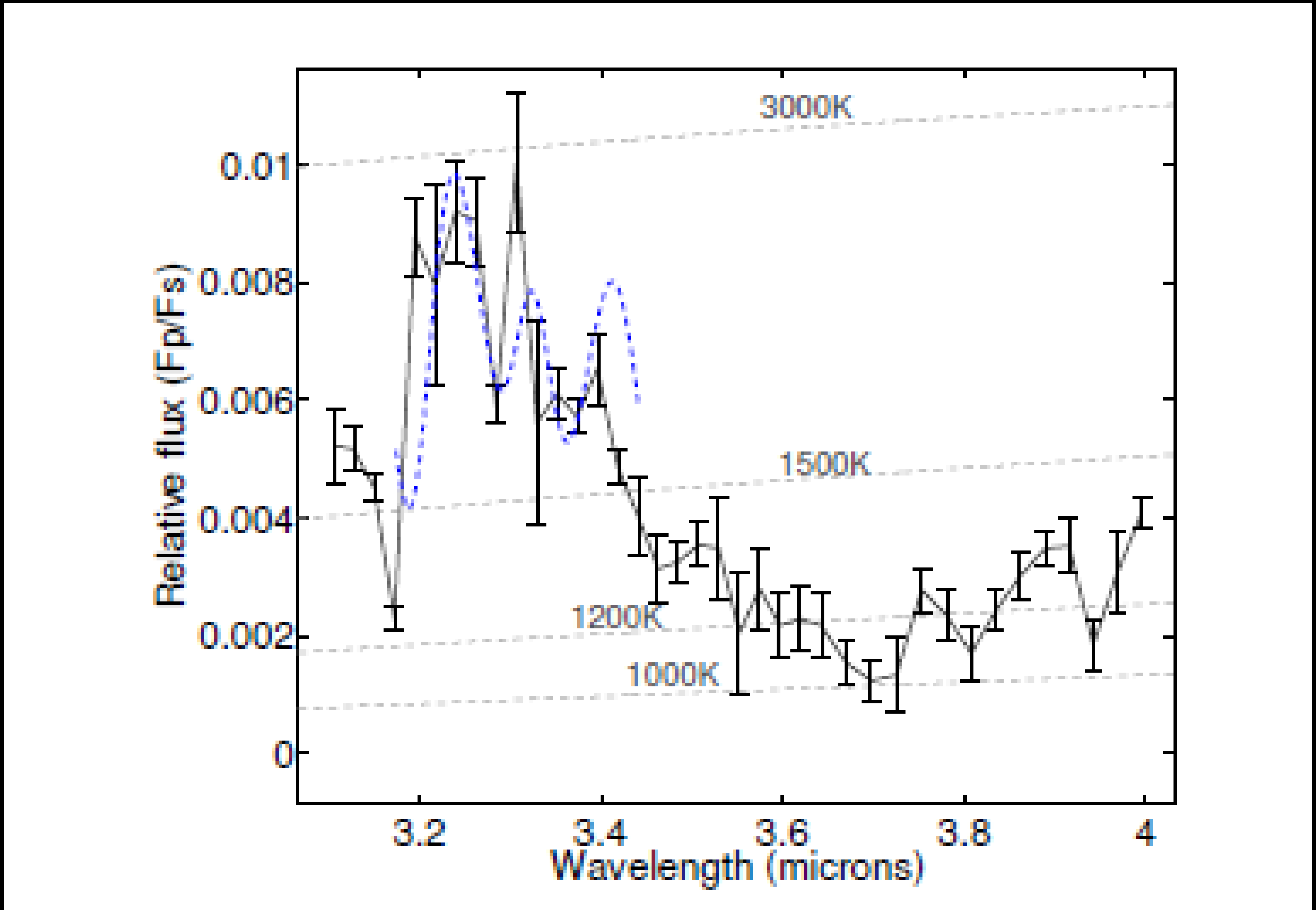

HD 189733b K+L bands

- Observations

(Waldmann et al, ApJ 2012)

- Non-LTE model joint K+L band

- Thermal emission only